

# **Testing the Attitude Determination and Control of a CubeSat with Hardware-in-the-Loop**

**Meghan Kathleen Quadrino, Prof David Miller and Prof Kerri Cahoy**

June 2014

SSL #06-14



# **Testing the Attitude Determination and Control of a CubeSat with Hardware-in-the-Loop**

**Meghan Kathleen Quadrino, Prof David Miller and Prof Kerri Cahoy**

June 2014

SSL #06-14

This work is based on the unaltered text of the thesis by Meghan Quadrino submitted to the Department of Aeronautics and Astronautics in partial fulfillment of the requirements for the degree of Master of Science at the Massachusetts Institute of Technology.



# Abstract

This thesis presents a methodology for testing the attitude determination and control of a CubeSat within a constrained environment. This approach first evaluates the concept of operations of the satellite mission, then takes into account the limitations of the test environment, formulates test plans that can validate algorithms with hardware-in-the-loop, and presents a model by which these tests can be evaluated. The Microsized Microwave Atmospheric Satellite (MicroMAS), a dual-spinner 3U CubeSat, is used as a case study to demonstrate both the overall methodology and the validation model. Laboratory experiments were performed with a one-degree-of-freedom rotation test set-up inside of a Helmholtz Cage magnetic field simulator. The theoretical development of the control algorithms and design choices are discussed. A software model of the controller, hardware, and test environment was used to evaluate the results from these experimental tests. The results showed that, using the designed control system, the satellite model is able to successfully detumble itself, achieve a desired angular rotation, and compensate for the momentum introduced by a rotating payload. The test data are analyzed and show that the control system is able to meet the mission pointing requirements of maintaining within 1 degree ( $3\sigma$ ) deviation from the nominal LVLH attitude after its slew maneuver, before payload spin-up. During its science operation mode, the tests showed a pointing deviation from nominal attitude of about 2.2 degrees ( $3\sigma$ ). The details of the constraints and limitations of the test environment and their impacts are discussed.



Disclaimer: The views expressed in this thesis are those of the author and do not reflect the official policy or position of the United States Air Force, the United States Department of Defense, or the United States Government.



# Acknowledgments

This work was performed primarily from funding from the MicroMAS CubeSat program, sponsored by MIT Lincoln Laboratory (account 6925546, PO 7000180248), and partially by the NASA Jet Propulsion Laboratory, Strategic University Partnership (2746259, RSA NO. 1492489). The author gratefully thanks the sponsors for their generous support that enabled this research. The author also thanks the entire MicroMAS team for their contributions to this work.

#everythingisawesome

#becausePayload



# List of Abbreviations

ADCS	Attitude Determination and Control Subsystem
ADACS	Attitude Determination And Control System
CAD	Computer-Aided Design
CMG	Control Moment Gyroscope
COTS	Commerical off-the-shelf
CPU	Central Processing Unit
EKF	Extended Kalman Filter
EM	Engineering Model
IGRF	International Geomagnetic Reference Model
IMU	Inertial Measurement Unit
LEO	Low-Earth Orbit
LVLH	Local Vertical Local Horizontal
MAI	Maryland Aerospace Incorporated
MIT	Massachusetts Institute of Technology
MicroMAS	Microsized Microwave Atmospheric Satellite
PIC	Peripheral Interface Controller
RPM	Revolutions per Minute
SEU	Single Event Upset
SSL	Space Systems Laboratory
TID	Total Ionizing Dose



# List of Variables

$\mathbf{A}(t)$	Continuous-time state transition matrix
$\mathbf{A}_d$	Discrete-time state transition matrix
$\mathbf{B}$	Magnetic field vector
$\dot{\mathbf{B}}$	First time derivative of magnetic field vector
$\mathbf{B}(t)$	Continuous-time input matrix
$\mathbf{C}(t)$	Continuous-time output matrix
$\mathbf{C}_d$	Discrete-time output matrix
$\mathbf{D}(t)$	Continuous-time feedthrough matrix
$G$	Gravitational constant
$I$	Electrical current
$\mathbf{I}$	Identity matrix
$J$	Scalar mass moment of inertia about one particular axis
$\mathbf{J}$	Mass moment of inertia matrix
$\mathbf{K}_d$	Derivative gain matrix
$\mathbf{K}_i$	Integral gain matrix
$\mathbf{K}_p$	Proportional gain matrix
$\mathbf{L}$	Angular momentum vector
$\mathbf{L}_k$	Kalman gain matrix
$\mathbf{P}_k$	Covariance matrix of state estimate
$\mathbf{P}_{k+1}$	Covariance matrix of state estimate at next time
$\mathbf{Q}_k$	Discrete process noise matrix
$\mathbf{R}(\theta)$	Rotation matrix
$\mathbf{R}_k$	Sensor covariance matrix
$a$	Coefficient of first-order exponential function
$b$	Exponent term in first-order exponential function
$c_d$	Scalar derivative gain term that describes the restoring torque of a string

$d$	Scalar gain term that describes the controller's derivative response
$\ell$	Scalar length
$k$	Scalar gain term, used in a variety of equations
$k_d$	Scalar proportional gain term that describes the restoring torque of a string
$m$	Mass of some object
$\mathbf{m}$	Magnetic dipole vector
$n$	Number of coil windings
$\hat{\mathbf{n}}$	Unit vector representing payload axis of rotation wrt the body frame of the satellite
$q_i$	Element of a quaternion
$\mathbf{q}$	Vector components of a quaternion
$\delta\mathbf{q}$	Quaternion innovation, containing only the vector components
$\bar{\mathbf{q}}$	4-Element quaternion, with scalar first and vector components following
$r$	Scalar distance from one object to another
$\mathbf{r}$	Three-dimensional position vector
$\Delta t$	Non-zero discrete amount of time
$\mathbf{u}$	Control torque vector
$\mathbf{u}(t)$	Continuous-time input matrix
$\mathbf{v}$	Some three-dimensional vector
$\mathbf{v}(t)$	Continuous-time sensor noise matrix
$\mathbf{v}_k$	Discrete-time sensor noise matrix
$\mathbf{w}(t)$	Continuous-time process noise matrix
$\mathbf{w}_k$	Discrete-time process noise matrix
$\mathbf{x}(t)$	Continuous-time state vector
$\dot{\mathbf{x}}(t)$	Continuous-time derivative of state vector
$\mathbf{x}_k$	Discrete-time state vector
$\hat{\mathbf{x}}_k$	Estimate of state vector
$\mathbf{x}_{k+1}$	Discrete-time state vector at next time
$\hat{\mathbf{x}}_{k+1}$	Estimate of state vector at next time
$\mathbf{y}(t)$	Continuous-time output matrix
$\mathbf{y}_k$	Discrete-time output matrix
$\Omega$	Skew-symmetric matrix of angular rate
$\alpha$	Angular acceleration vector
$\beta_i$	Component of the bias of the rate gyroscope
$\beta$	Vector containing the biases of the rate gyroscope
$\boldsymbol{\eta}_u$	Vector describing zero-mean Gaussian white noise process

$\eta_v$	Vector containing noise on gyro measurement
$\lambda$	Unit vector along eigenaxis
$\mu_0$	Scalar constant describing the permeability of free space
$\omega_d$	Damped frequency of oscillation of a second-order under-damped system
$\omega_n$	Natural frequency of a second-order under-damped system
$\omega_{x,y,z}$	Component of angular rate, corresponding to an axis
$\omega$	Angular rate vector
$\dot{\omega}$	Vector containing first time derivative of angular rate
$\bar{\omega}$	Measured vector of angular rate from rate gyroscope
$\phi$	Angle or angular displacement
$\dot{\phi}$	First time derivative of angular displacement
$\ddot{\phi}$	Second time derivative of angular displacement
$\sigma_i$	Scalar standard deviation of a particular measurement element
$\tau$	Torque vector
$\theta$	Angle from one vector to another
$\theta_d$	Angular displacement from a neutral, non-rotated position
$\dot{\theta}_d$	Rate of oscillation of damped harmonic oscillator
$\zeta$	Damping coefficient of a second-order under-damped system



# Contents

<b>1</b>	<b>Introduction to Attitude Determination and Control Subsystem (ADCS) for Small Satellites and Review of Literature</b>	<b>29</b>
1.1	Introduction to ADCS on Small Satellites . . . . .	29
1.1.1	Purpose of Attitude Determination and Control . . . . .	30
1.1.2	Measuring Attitude . . . . .	30
1.1.3	Controlling Attitude . . . . .	32
1.2	Previous CubeSat Missions with Attitude Control . . . . .	33
1.3	Ground-Based Testing and Validation of ADCS . . . . .	35
1.4	Introduction to MicroMAS . . . . .	38
<b>2</b>	<b>Control Algorithms &amp; Extended Kalman Filter</b>	<b>41</b>
2.1	Overview of MicroMAS's Attitude Determination and Control . . . . .	41
2.1.1	Sensors . . . . .	43
2.1.2	TRIAD Algorithm . . . . .	49
2.2	Extended Kalman Filter (EKF) Application to Attitude Estimation for Satellites	51
2.2.1	General State Space Representation . . . . .	52
2.2.2	Definition of State Vector . . . . .	54
2.2.3	Propagating the State . . . . .	55
2.2.4	Updating the State with the Innovation . . . . .	60

2.2.5	Summary of EKF Process . . . . .	62
2.3	Control Law Theory . . . . .	62
2.3.1	Actuators . . . . .	62
2.3.2	B-Dot Algorithm . . . . .	64
2.3.3	Linear Quaternion Feedback Estimator . . . . .	65
2.4	Control Law Implementation for a Dual-Spinner CubeSat . . . . .	71
2.4.1	Introducing New Terms to the Control Vector . . . . .	73
<b>3</b>	<b>Constraints and Facilities for ADCS Tests</b>	<b>77</b>
3.1	Space Environment . . . . .	77
3.1.1	Microgravity . . . . .	78
3.1.2	Earth's Magnetic Field . . . . .	79
3.1.3	Radiation . . . . .	80
3.1.4	Cold Space and Vacuum . . . . .	81
3.2	Simulating Microgravity . . . . .	82
3.2.1	Challenges and Constraints . . . . .	82
3.2.2	Spherical Air Bearing . . . . .	82
3.2.3	Limitations of Air Bearing Tests . . . . .	84
3.2.4	Uniaxial Attitude Control Tests: "Piñata" Rig . . . . .	87
3.2.5	Zero-G Tests . . . . .	90
3.3	Earth's Magnetic Field . . . . .	91
3.3.1	Helmholtz Cage . . . . .	91
3.3.2	Merritt 4-Coil Helmholtz Cage . . . . .	92
<b>4</b>	<b>Mission Concept of Operations: Requirements and Test Descriptions</b>	<b>101</b>
4.1	Goals and Requirements of Small Satellite ADCS Testing . . . . .	101
4.2	ADCS Modes . . . . .	102

4.3	Detumble Mode . . . . .	103
4.3.1	Explanation of Detumble Mode . . . . .	103
4.3.2	Testing B-dot Control using the Helmholtz Cage . . . . .	105
4.3.3	Evaluating Performance of the B-dot Control . . . . .	107
4.4	Slew Mode . . . . .	111
4.4.1	Explanation of Slew Mode . . . . .	111
4.4.2	Testing Slew Mode using the Piñata Rig and the Helmholtz Cage . .	115
4.4.3	Evaluation of Slew Mode . . . . .	119
4.5	Spin-up Mode . . . . .	120
4.5.1	Explanation of Spin-up Mode . . . . .	120
4.5.2	Testing Spin-up Mode using the Piñata Rig and the Helmholtz Cage	122
4.5.3	Evaluating the Spin-up . . . . .	122
4.6	Stabilization (Science) Mode . . . . .	123
4.6.1	Explanation of Stabilization Mode . . . . .	123
4.6.2	Testing of Stabilization Mode . . . . .	124
4.6.3	Evaluating Stabilization . . . . .	124
<b>5</b>	<b>Test Results</b>	<b>125</b>
5.1	Overview . . . . .	125
5.2	Verification of Actuator Performance . . . . .	126
5.2.1	Magnetorquers . . . . .	126
5.2.2	Reaction Wheels . . . . .	128
5.3	Estimator Results . . . . .	130
5.3.1	Illustration of EKF Performance . . . . .	130
5.3.2	Making the Filter Robust to Changes in Sensor Inputs . . . . .	131
5.4	Detumble Mode . . . . .	134

5.4.1	Piñata Tests about the X-Axis . . . . .	134
5.4.2	Piñata Tests about the Y-Axis . . . . .	137
5.4.3	Reading the Signs . . . . .	139
5.5	Slew Mode . . . . .	141
5.5.1	Setting up the Test . . . . .	142
5.5.2	Modeling the Test Environment . . . . .	143
5.5.3	Slewing about the X-Axis . . . . .	145
5.5.4	Slewing about the Y-Axis . . . . .	148
5.5.5	Slewing about the Z-Axis . . . . .	151
5.6	Spin-up & Stabilization Modes . . . . .	154
5.6.1	Spinning up the Payload . . . . .	154
5.6.2	Stabilizing after Payload Spin-up . . . . .	156
5.6.3	Zero G Flight Results . . . . .	159
<b>6</b>	<b>Discussion of Test Results and Model</b>	<b>161</b>
6.1	Discussion of Test Results . . . . .	161
6.1.1	Estimator . . . . .	161
6.1.2	Detumble Mode . . . . .	162
6.1.3	Slew Mode . . . . .	165
6.1.4	Spin-up Mode . . . . .	166
6.1.5	Stabilization Mode . . . . .	167
6.2	Robustness of Model . . . . .	167
6.2.1	Exploring Uncertainties . . . . .	168
6.2.2	Inertia of the Satellite . . . . .	168
6.2.3	Proportional and Derivative Gains of the String . . . . .	170
6.2.4	Damping Coefficient that Models Response of String . . . . .	170

6.2.5	Natural Frequency that Models Response of String . . . . .	172
6.3	Concluding Thoughts . . . . .	173
<b>7</b>	<b>Conclusion and Future Work</b>	<b>175</b>



# List of Figures

1-1	Quantifying Angular Rotation from Two Vectors . . . . .	31
1-2	CanX2 . . . . .	33
1-3	QbX-1 and QbX-2 . . . . .	34
1-5	ADCS Ground Test Capabilities at the Space Dynamics Laboratory at Utah State University . . . . .	36
1-6	Attitude Control System High Detail Simulator (ACS- HDS) at the University of Alcala, Madrid . . . . .	37
1-7	Photograph of the ExoPlanetSat Air Bearing TestBed . . . . .	38
1-8	CAD Model of MicroMAS . . . . .	39
1-9	CAD Model of MicroMAS with Components Highlighted . . . . .	40
2-1	MicroMAS ADCS Block Diagram . . . . .	42
2-2	MicroMAS Sensors & Reference Frames . . . . .	43
2-3	Analog Devices 16334 Inertial Measurement Unit . . . . .	44
2-4	PNI MicroMag-3 . . . . .	45
2-5	Silonex SLSD-717N7 Solderable Planar Photodiode . . . . .	45
2-6	Excelitas Technologies' TPD Thermopile . . . . .	48
2-7	Discrete Kalman Filter Recursive Loop . . . . .	56
2-8	Maryland Aerospace Incorporated 400 Mini ADACS Unit . . . . .	63

3-1	Earth's Magnetic field and magnetosphere . . . . .	79
3-2	Spherical Air Bearing . . . . .	83
3-3	MicroMAS "Flat-Sat" for Air Bearing Testing . . . . .	85
3-4	CAD Model of Engineering Unit MicroMAS Satellite . . . . .	88
3-5	Comparison of EM and Flight Satellites with Transparent Chassis . . . . .	89
3-6	Properties of Merritt 4-Coil Design . . . . .	94
3-7	Implementation of 4-Coil Design around Spherical Air Bearing . . . . .	96
3-8	MIT Space Systems Laboratory's Helmholtz Cage . . . . .	97
3-9	Block Diagram of Helmholtz Cage Interface . . . . .	98
3-10	Uniformity of Helmholtz Cage Along X-Axis . . . . .	99
3-11	Uniformity of Helmholtz Cage Along Y-Axis . . . . .	100
4-1	MicroMAS ADCS Mode Diagram . . . . .	103
4-2	Drawing of Desired Magnetic Field within 4-coil per axis Helmholtz Cage for Magnetorquer Actuation with EM Satellite Shown Suspended . . . . .	106
4-3	MicroMAS in its nominal LVLH attitude . . . . .	112
5-1	Y-Axis Magnetorquer Duty Cycling . . . . .	127
5-2	Measured Reaction Wheel Torque with a Linear Fit . . . . .	129
5-3	Covariance Matrix with respect to Logarithmic Time Scale . . . . .	131
5-4	Measured vs Filtered Quaternion . . . . .	132
5-5	Instantaneous Change of Sensor Inputs to Attitude Estimate . . . . .	132
5-6	Kalman Filter Reset: Instantaneous Change of Sensor Inputs to Attitude Estimate . . . . .	133
5-7	EM Satellite Hanging in Cage with its Body X-Axis Along Axis of Rotation	135
5-8	Comparison of Detumble Tests along X Axis . . . . .	136
5-9	Simple Model of String as Second-order System . . . . .	136

5-10 Comparison of Detumble Tests along Y-Axis . . . . .	138
5-11 EM Satellite Hanging in Cage with its Body Y-Axis Along Axis of Rotation	139
5-12 Actuating Case with One Sign Error . . . . .	140
5-13 Actuating Case with Both Signs Incorrect . . . . .	141
5-14 Simulink Model of Satellite with Restoring Torque due to String . . . . .	143
5-15 Time Response of a Slew about the X-Axis . . . . .	146
5-16 Zoomed-in Look at Steady State Response of Slew: X-Axis . . . . .	148
5-17 Time Response of a Slew about the Y-Axis . . . . .	149
5-18 Zoomed-in Look at Steady State Response of Slew: Y-Axis . . . . .	150
5-19 Time Response of a Slew about the Z-Axis . . . . .	152
5-20 Zoomed-in Look at Steady State Response of Slew: Z-Axis . . . . .	153
5-21 Payload Spin-up . . . . .	155
5-22 Stabilization During and After Payload Spin-up . . . . .	157
5-23 Torque of X Reaction Wheel During Spin-up and Stabilization . . . . .	159
6-1 Simulation of Hanging Test of Detumble Mode . . . . .	163
6-2 Prediction of Magnetorquer Effect on Damping Compared with Actual Data	164
6-3 Modeling the String Response as a Second Order System . . . . .	165
6-4 Comparison of Data with Models with Varying Inertia Estimates . . . . .	169
6-5 Model Response to Changing the Damping Coefficient of the String . . . . .	171
6-6 Model Response to Changing the Natural Frequency of the String . . . . .	173



# List of Tables

2.1	Sensor Rankings for use in TRIAD Algorithm . . . . .	50
3.1	Merritt 4-Coil Design Parameters . . . . .	94
4.1	Detumble Mode Operations Summary . . . . .	104
4.2	Slew Mode Operations Summary . . . . .	114
4.3	Spin-up Mode Operations Summary . . . . .	121
4.4	Stabilization Mode Operations Summary . . . . .	124
5.1	Parameters of the Time Response: X-Axis . . . . .	137
5.2	Parameters of the Time Response: Y-Axis . . . . .	139
5.3	Parameters of the Slew Maneuver: X-Axis . . . . .	147
5.4	Parameters of the Slew Maneuver: Y-Axis . . . . .	150
5.5	Parameters of the Slew Maneuver: Z-Axis . . . . .	153



# **Chapter 1**

## **Introduction to Attitude Determination and Control Subsystem (ADCS) for Small Satellites and Review of Literature**

### **1.1 Introduction to ADCS on Small Satellites**

Traditionally, communications and surveillance missions use monolithic satellites that are on the order of thousands of kilograms, or around the size of a school bus, and cost billions of dollars. Small satellites are defined as less than 500 kilograms. Within that classification, there are minisatellites (100-500 kg), nanosatellites (1-10 kg), picosatellites (0.1-1 kg), and tiny femtosatellites, (<100 grams)[1]. These small satellites provide an opportunity to prove new technological innovations at a fraction of the cost of traditional large satellite programs. With that trade-off in cost come many challenges in trying to fit components that enable the critical capabilities of large satellites in a size, weight, and power (SWAP) -constrained

environment. CubeSats are nanosatellites with a base unit volume of 10x10x10 centimeters<sup>3</sup>, and mass of less than 1.33 kg per unit (1U). [2]

Among the challenges facing nanosatellites is the determination and control of the pointing of the satellite. For ADCS, a smaller satellite means less volume and mass for sensors and actuators, as well as less processing power for algorithms on a smaller, more limited central processing unit. These challenges have not yet been fully addressed, as small satellites are still a burgeoning enterprise. In this work, we aim to develop a modeling and hardware-in-the-loop approach to validate attitude determination and control for CubeSats.

### **1.1.1 Purpose of Attitude Determination and Control**

Typically, Earth-orbiting satellites are launched for Earth observation or sensing. Once the satellite is in orbit, it is in a microgravity environment, which means that without the application of force, it will be in a free tumble. Objects in low-earth orbit (LEO) also experience disturbances due to aerodynamic drag, J2 effects due to the oblateness of the Earth, and solar radiation pressure, among others. In order for a satellite to be able to accomplish its mission, it must be pointed in the desired direction. Often, requirements for Earth-observation satellites are quite stringent in terms of pointing. The measurement of pointing, or angular rotation, is called a satellite's attitude.

### **1.1.2 Measuring Attitude**

Attitude is simply a measurement of a rotation from some pre-defined non-rotated orientation. It can be measured by using sensors that can give measurements of a known quantity (*e.g.* magnetic field, direction of the sun, direction of a star, etc.) in the form of three-

dimensional vector. An attitude estimate is created by combining information from two sensors, and compare the measured values are with the expected values at the nominal non-rotated position. [3] As the satellite tumbles in space, the measurement deviation from the expected value indicates how far, and about which axis, the satellite has rotated. Figure 1-1 shows two vectors, and how the second can be used to give information about the rotation about the first.

Each of these sensors yield a three dimensional vector estimate of the direction of some

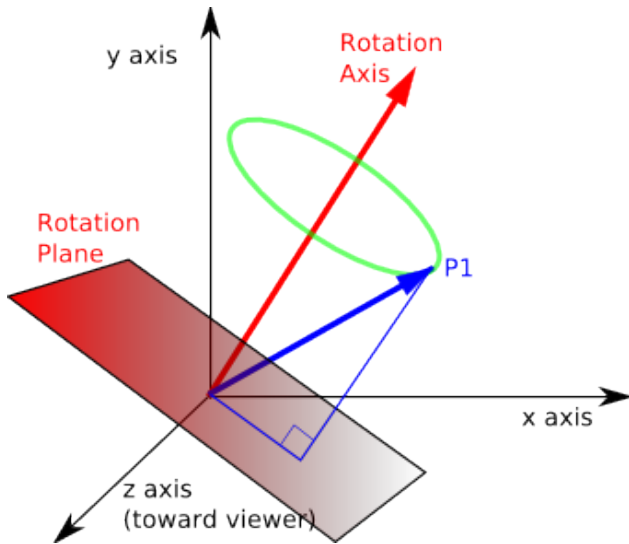


Figure 1-1: Quantifying Angular Rotation from Two Vectors [4]

object (magnetic field vector, the sun, the Earth, a star). These sensor estimates can be compared to the known location of the object in the nominal, non-rotated orientation of the satellite. Examples of sensors used for attitude measurement or determination in small satellites, are inertial measurement units (IMUs), magnetometers, sun sensors, Earth sensors, and star trackers. These sensors are commercially available in form factors small enough for nanosatellites. Sensors will be discussed more in detail in Chapter 2.

### 1.1.3 Controlling Attitude

Control of attitude requires actuators that can impart torque in precise increments about specific axes. In small satellites, this can be especially challenging. Although the inertia of the overall satellite is smaller, and thus requires less torque to achieve the same rotation than for a more massive satellite, high quality, reliable actuators that can both provide the necessary torque and are small enough to fit inside of a nanosatellite are still under development.

Traditionally, attitude control is accomplished with propulsion, control moment gyros (CMGs), and reaction wheel sets. The advantage of propulsion is that it enables both translational and rotational motion, but the disadvantage is that that eventually, thrusters run out of fuel. It is also difficult to find propulsion units that would fit inside a nanosatellite. Control moment gyroscopes impart torque by using a motorized gimbal to tilt the axis of a spinning rotor. However, CMGs are not yet commercially available in the CubeSat form factor.

Reaction wheel sets operate using the principle of conservation of momentum, where they increase or decrease rotation rates to impart torque. Reaction wheels come in a set of at least three – one per axis – where a wheel is spun by a motor, which transfers momentum of the tumbling satellite into the spinning wheel. (A set of four wheels is preferable, for redundancy.) Often, these reaction wheel sets are accompanied by magnetic torque rods, which apply current through a rod or coil. This induces a magnetic flux, which causes a torque. Magnetorquers are most effective in LEO, since that is where the Earth’s magnetic field is strongest. Nanosatellites typically use torque rods, with one or three miniature reaction wheels.

## 1.2 Previous CubeSat Missions with Attitude Control

There have only been a few CubeSat missions so far that use some form of active attitude control. Active attitude control means that a satellite uses some kind of actuator to impart torque to affect its rotation. Passive attitude control takes advantage gravity gradient torques, aerodynamic drag, and other environmental disturbances to point itself in a desired orientation, but does not produce any torque itself.

We will address three here that are relevant to showing the progression of attitude knowledge and control in nanosatellites. Those three are: CanX2 by the University of Toronto, the Qb-X missions of the Naval Research Laboratory in Washington, DC, and PSSCT-2 and AeroCube-4 of the Aerospace Corporation in El Segundo, California.

One of the first satellites that attempted attitude control was CanX2 in 2008, built by the University of Toronto's Institute for Space Studies. It uses a magnetometer and sun sensors for attitude knowledge, and uses magnetorquers, supplemented by one reaction wheel, made by Sinclair, about its long axis. CanX2 has achieved about 1.5 degrees of pointing knowledge in sunlight and about 5 degrees of control during slew (rotation maneuver) with its one wheel [5].

Qb-X1 and Qb-X2 sponsored by the Naval Research Laboratory were another pair of

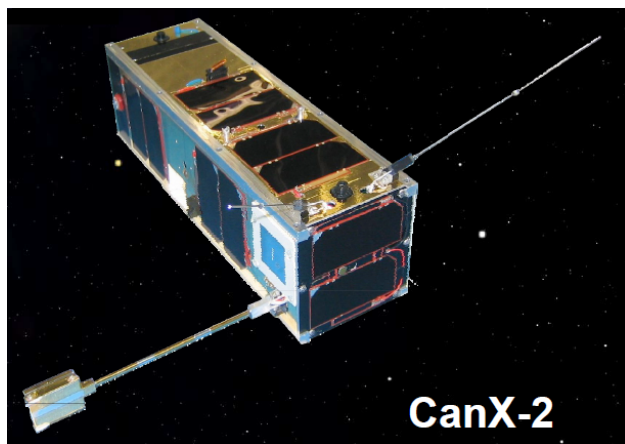


Figure 1-2: CanX2 [5]

CubeSats with active attitude control. These CubeSats, launched in 2010, use an International Geomagnetic Reference Field (IGRF) model for rate-damping using magnetorquers, but lack full attitude determination. They have a three-reaction wheel and magnetorquer IMI-100 ADACS unit made by Maryland Aerospace Incorporated (formerly IntelliTech Inc.) of Crofton, Maryland for attitude control. The “pointing controller consists of a combination of passive attitude stabilization and active rate damping control” using natural gravity gradient torques, aerodynamic drag, and limited use of reaction wheels. [6] Testing was done on these satellites to characterize each satellite’s residual dipole, and simulation analyses were performed for the control law. Their on-orbit data showed attitude knowledge no better than 25 degrees, but report stable attitude control. [7]

The Aerospace Corporation has built and launched many CubeSats over the past decade.

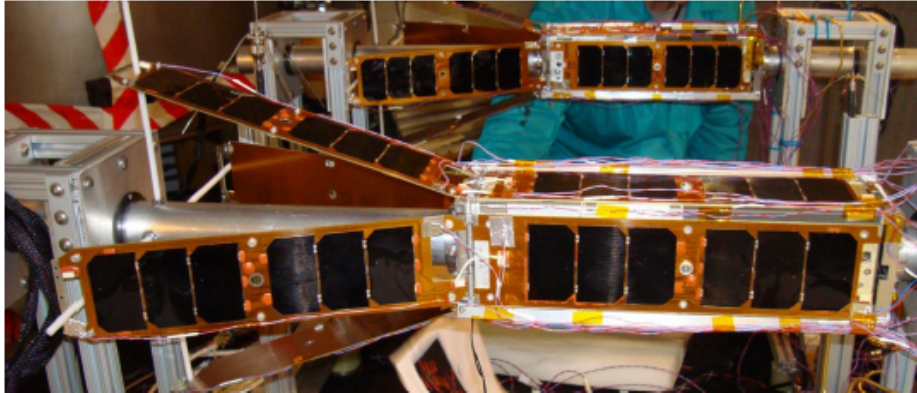


Figure 1-3: QbX-1 and QbX-2 [7]

PSSCT-2, launched in 2011, has Earth horizon sensors, sun sensors, and a magnetometer for attitude determination and three reaction wheels supplemented by three magnetorquers for attitude control. The reaction wheels and torque rods were built by the Aerospace Corporation. They demonstrated closed-loop 3-axis attitude control. [8] They also launched AeroCube-4 in 2012, which had a goal of less than a degree of pointing precision, based on its inertial measurement unit (IMU) measurements of rotation rate. Aerospace has re-

ported that PSSCT-2 achieved 5 degrees of pointing accuracy and AeroCube-4 demonstrated 3 degrees of pointing accuracy. [9] The reduced accuracy in AeroCube-4 was attributed to the loss of an axis of knowledge of the magnetic field and corruption of the microelectrical mechanical IMU by helium absorption.[9] Aerospace has planned missions to demonstrate 1 degree and 0.5 degree pointing accuracy on AeroCube-5 and AeroCube-OCSD respectively. AeroCube-OCSD augment its sensor suite with multiple star trackers with less than  $0.1^\circ$  accuracy to achieve high-precision pointing. [9]



(a) PSSC2 [8]



(b) AeroCube-4 [8]

### 1.3 Ground-Based Testing and Validation of ADCS

Because pointing control is so critical to many CubeSat missions, a rigorous methodology for ground-based test and evaluation is needed. Many universities have developed 3-axis attitude control testbeds for the purpose of validating ADCS systems on real hardware. [10][11][12],[13] These testbeds are typically made up an air bearing or other gimbal platform to enable freedom of rotation about one or multiple axes. Many also have some form of magnetic field emulator.

The Space Dynamics Laboratory (SDL) at Utah State University (USU) has developed

a hardware-in-the-loop testbed for simulating the conditions to stimulate attitude sensors and actuators, and performed testing on the DICE and PEARL satellites. [10] SDL predicts its evaluation of pointing accuracy of its tests to be  $0.19^\circ$ ,  $1\sigma$ . A summary of the extensive capabilities are shown in Figure 1-5.

End-to-end validation of an attitude control system for a INTA-Nanosat-1B was per-

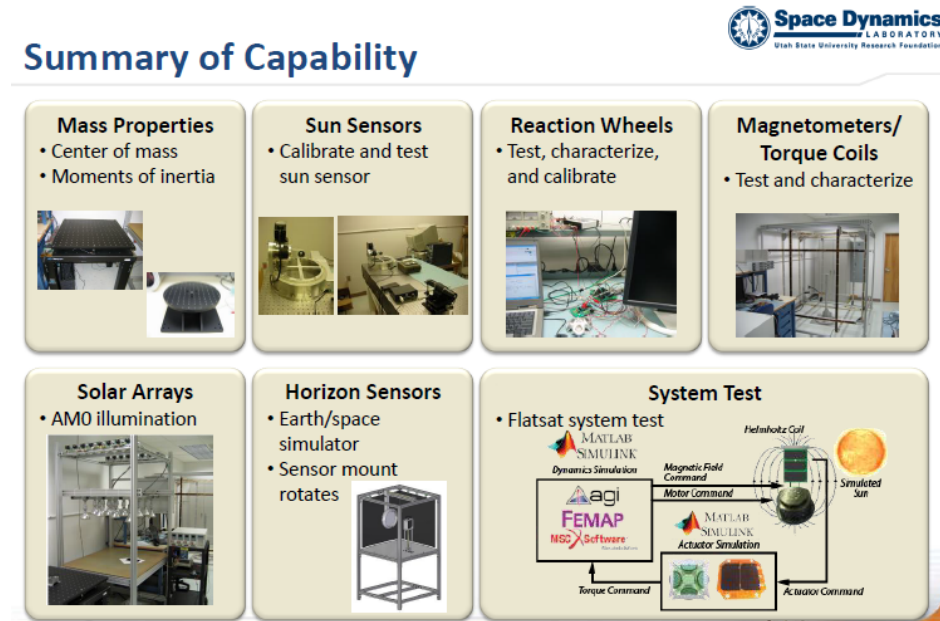


Figure 1-5: ADCS Ground Test Capabilities at the Space Dynamics Laboratory at Utah State University [10]

formed using a combination of hardware with software simulation of sensor inputs at the Space Research Group at the University of Alcala in Madrid. *Polo* and his team created a simulated environment on a PC, which then fed simulated values to the satellites' sensors, which their controller and actuators then responded to. The resultant torque of the actuators was then fed back into the simulation to track the satellite's dynamics. The closed-loop tests were able to help the team to validate each of their control modes, and detect and solve problems that they had been previously unaware of. [14] A diagram of their dynamics environment is shown in Figure 1-6.

Testing of high-precision pointing was performed at MIT's Space Systems Lab for a

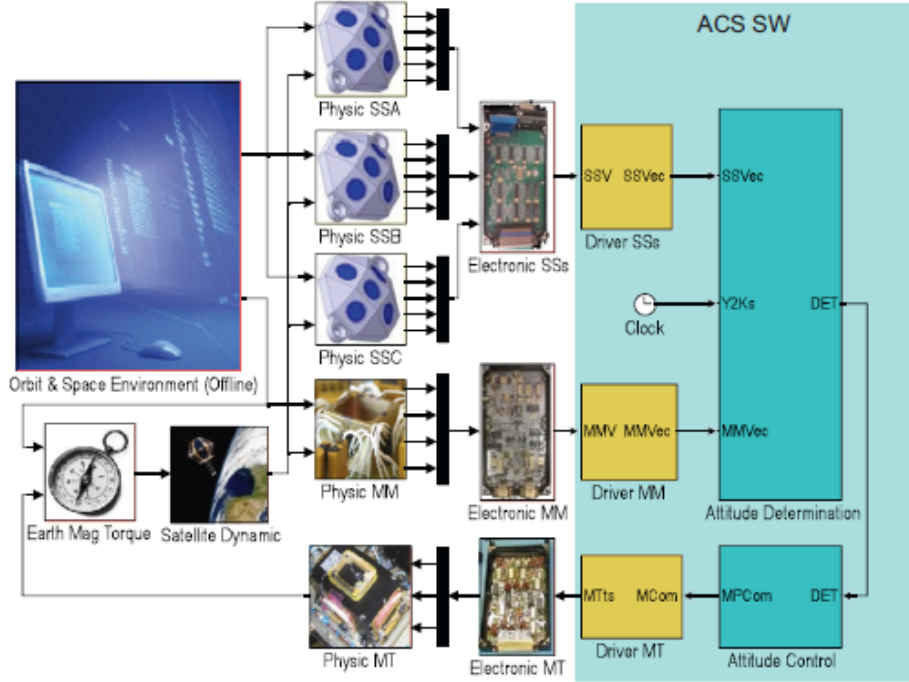


Figure 1-6: Attitude Control System High Detail Simulator (ACS- HDS) at the University of Alcala, Madrid [14]

ExoPlanetSat, a CubeSat mission due to launch in 2016. *Pong* was able to demonstrate precision pointing on his air-bearing testbed with flight-equivalent hardware of 12 arcseconds ( $3\sigma$ ). He used a star tracker and a computer monitor with a map of a star field to achieve high precision attitude knowledge, and developed his own software algorithms to improved pointing control. [15] A photograph of his testbed is shown in Figure 1-7.

This work aims to contribute to the body of knowledge of ground testing of attitude determination and control algorithms on nanosatellites with hardware-in-the-loop. We present a methodology for testing the attitude determination and control for small satellites in a resource-constrained environment.

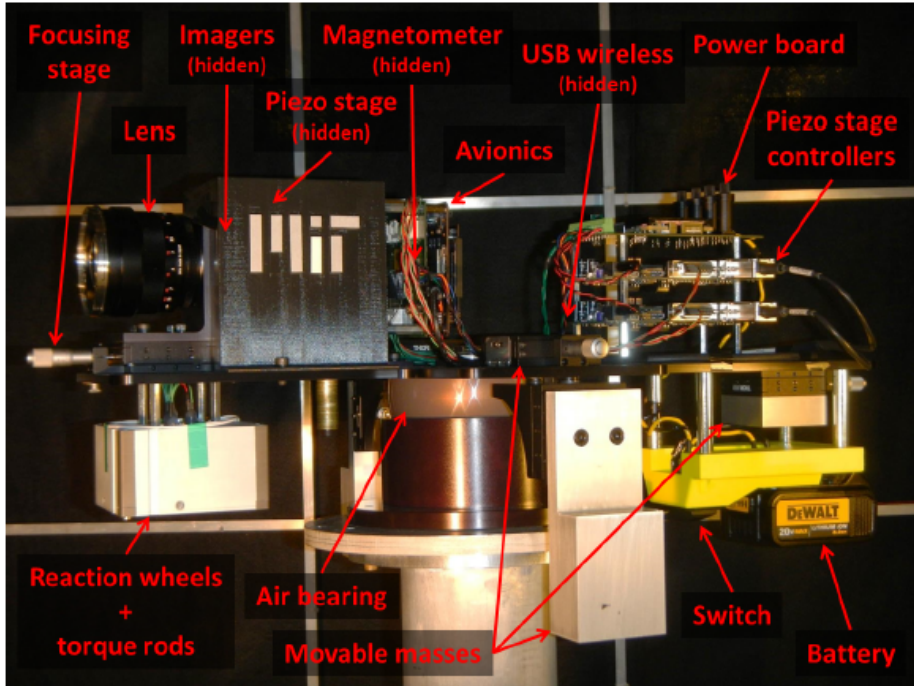


Figure 1-7: Photograph of the ExoPlanetSat Air Bearing TestBed [15]

## 1.4 Introduction to MicroMAS

The case study for this research is MicroMAS, a 3-U CubeSat (10x10x34 cm) built jointly by MIT's Lincoln Laboratory and Space Systems Lab on campus. It is unique in that it is dual-spinner CubeSat. Its payload, a microwave radiometer that takes measurements of oxygen gas absorption in the atmosphere, rotates at a constant rate while the rest of the satellite must remain stabilized over Earth. The rotation allows for the radiometer to calibrate its measurements against cold space. This is a unique challenge for attitude determination and control on a CubeSat, based on limited actuator abilities and little ADCS pointing heritage.

The Microsized Microwave Atmospheric Satellite, or MicroMAS, is a dual-spinner 3-U CubeSat, with a variety of commercial off-the-shelf (COTS) sensors and actuators, including an inertial measurement unit, a magnetometer, sun sensors, infrared Earth horizon sensors, and a miniature reaction wheel set supplemented by torque rods. The bus and scanner

assembly were designed and built by graduate students at MIT, and the payload was designed and built by Lincoln Laboratory and University of Massachusetts, Amherst [16]. A computer-aided design (CAD) structural model of the satellite is shown in Figure 1-8.

The payload rotates about the vertical axis in the picture. It has four deployable

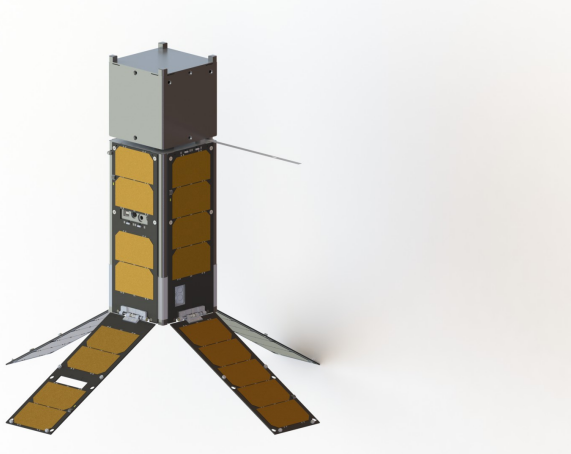


Figure 1-8: CAD Model of MicroMAS [17]

solar panels, and four body-mounted panels. A breakdown of the components are shown in Figure 1-9. [18] The boardstack which contains the avionics and holds some of the sensors was a combination of COTS components by Pumpkin Incorporated and unique design circuit board design. [19] The ADACS (attitude determination and control subsystem) unit is a MAI-400 three-reaction wheel and magnetorquer set by Maryland Aerospace Incorporated. The scanner assembly is made by Aeroflex, the motor controller is made by Elmo, and the encoder is made by Micro-E electronics. The inertial measurement unit is made by Analog Devices. The relevant sensors and actuators will be discussed in more detail in Chapters 2 and 4.

The decision to use a dual-spinner design, rather than rotating the entire satellite, was made because of the limited ability of the reaction wheels and magnetorquers to be able to provide the necessary torque to stabilize an entire spinning satellite. [20] Thus, one of the reaction wheels must match the angular momentum of the rotating payload in order to

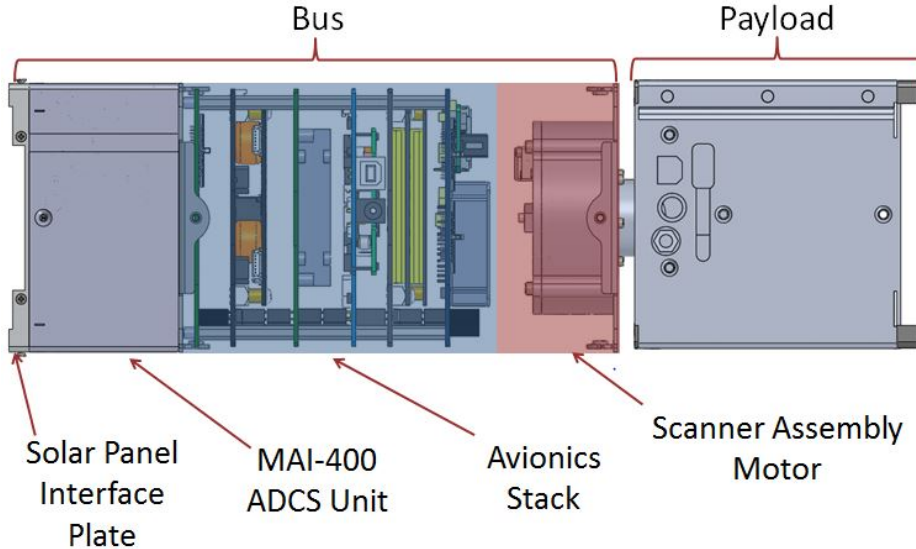


Figure 1-9: CAD Model of MicroMAS with Components Highlighted [18]

stabilize the satellite.

MicroMAS serves a good case study because it requires 1 degree accuracy in pointing to accomplish its mission to take precision measurements of the atmosphere. The satellite must remain stabilized throughout its science data collection. This is an ambitious goal knowing that the rotating payload will provide a constant source of momentum to manage, in addition to any disturbances the satellite may encounter. The rest of this work is dedicated to setting up and explaining how this ambitious goal can be successfully validated with ground tests.

Chapter 2 presents the estimation and control algorithms that are used. Chapter 3 discusses the constraints of hardware testing and what facilities are available. Chapter 4 presents the ADCS modes of MicroMAS, a specific test plan for each mode, and the metrics to evaluate each test. Chapter 5 presents the results of these tests as compared with those metrics. Chapter 6 is a discussion of the results along with an analysis of the model used for comparison. Chapter 7 briefly presents future work in the area of attitude determination and control testing on CubeSats.

# **Chapter 2**

## **Control Algorithms & Extended Kalman Filter**

### **2.1 Overview of MicroMAS's Attitude Determination and Control**

As noted in Chapter 1, the case study for this testing is a nanosatellite called MicroMAS. MicroMAS is a 3U CubeSat sponsored by MIT Lincoln Laboratory in collaboration with MIT's Space Systems Laboratory. It is a proof-of-concept mission for weather tracking with a microwave radiometer in a CubeSat form factor. Because its payload takes passive thermal measurements of the Earth's atmosphere with respect to altitude, knowing and controlling the attitude of the satellite is critical to the mission. To do this, MicroMAS uses a proportional-integral-derivative (PID) control law with reaction wheels as the primary actuator, supplemented by magnetic torque rods that help to dump the excess momentum that disturbance torques introduce. The attitude information is gathered from sensors which give vector information in the body frame of the satellite. These body-frame vectors are then compared to vectors in the inertial frame, computed using an orbit propagator, to generate

an estimate of angular rotation in the form of a quaternion.

An Extended Kalman Filter is then used to filter the attitude estimate, by taking the measured quaternion and the measured angular rate from the inertial measurement unit as inputs. The control law then uses the filtered quaternion and angular rate for its feedback control. The block diagram in Figure 2-1 illustrates the flow from sensors, to software, to actuators, to the environment and non-linear dynamics. In this chapter, the focus is presenting the information contained within the software block which performs the attitude estimation and control.

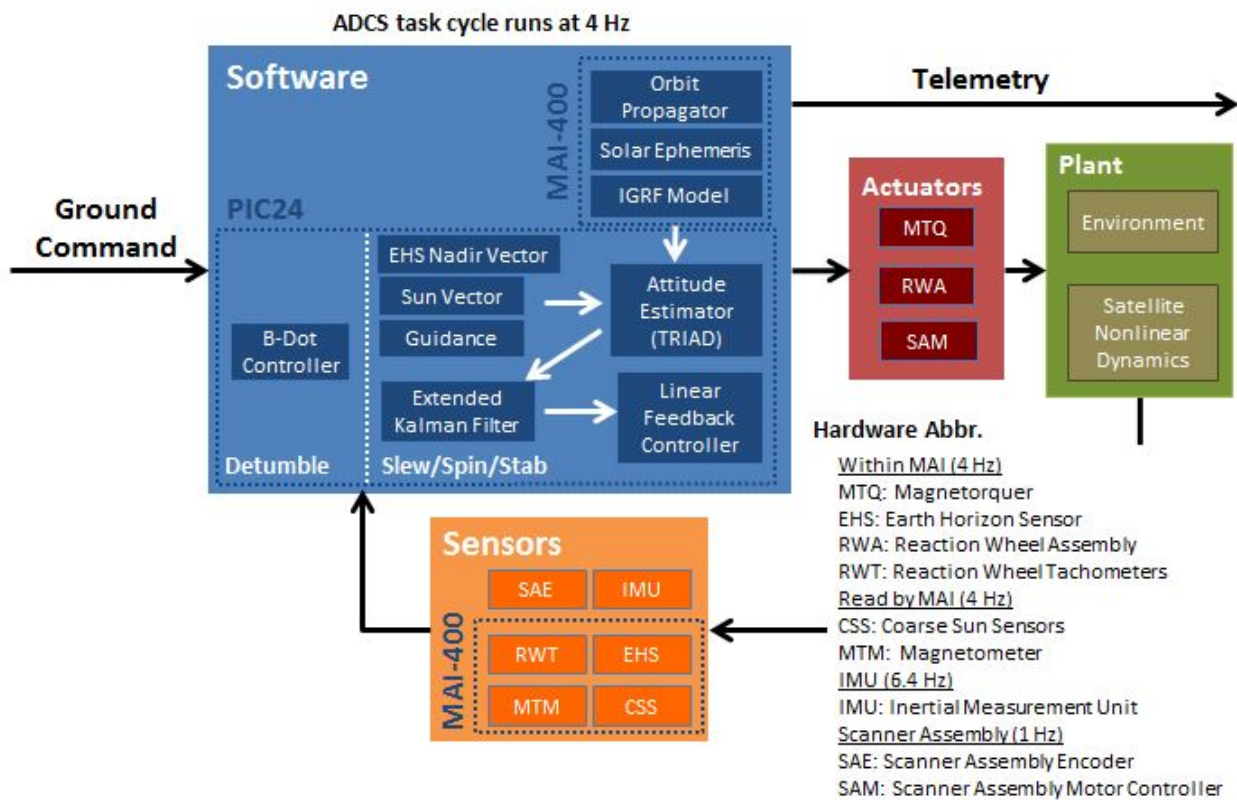


Figure 2-1: MicroMAS ADCS Block Diagram

### 2.1.1 Sensors

To understand how to control the attitude, it is important to understand the process from sensor input, to attitude knowledge formulation, any filtering done on the measurements collected, and then how those measurements are fed into the control law. This process begins with the sensors that the satellite uses to formulate a unit vector, which contains directional information. These vectors can then be combined to yield a quaternion. MicroMAS has sun sensors, Earth horizon sensors, an inertial measurement unit containing both rate gyros and an accelerometer, and a magnetometer. The sensors and their respective reference frames are shown in the Figure 2-2. The acronyms will be explained in the following subsections. All axes will be referred to in the body frame (shown in purple in Figure 2-2), unless otherwise specified.

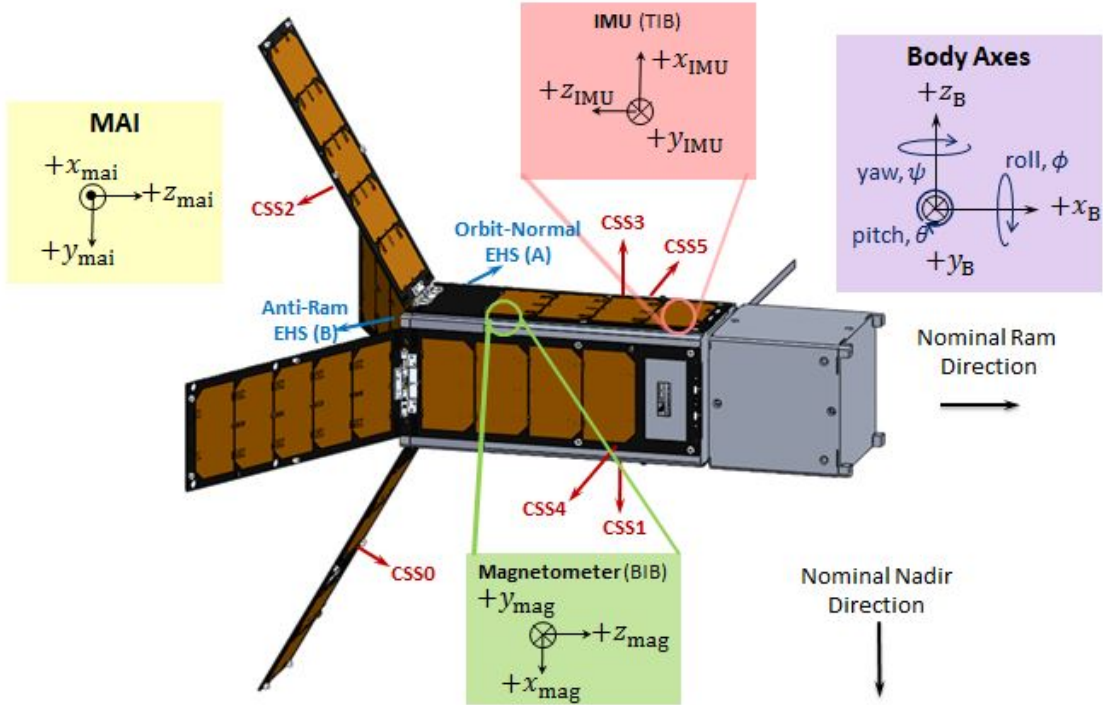


Figure 2-2: MicroMAS Sensors & Reference Frames [21]

### 2.1.1.1 Inertial Measurement Unit

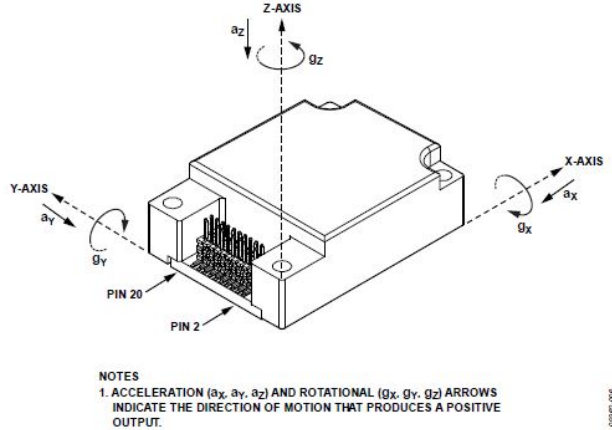


Figure 2-3: Analog Devices 16334 Inertial Measurement Unit [22]

MicroMAS has an ADIS 16334 inertial measurement unit made by Analog Devices. It contains both a micro-electrical-mechanical systems (MEMS) rate gyroscope and a tri-axial linear accelerometer. The range of the gyroscope is adjustable, but the most sensitive setting has a range of  $\pm 75^\circ/\text{s}$  and with a sensitivity of  $\pm 0.0125^\circ/\text{s}$ . It has an internal Bartlett Window FIR filter as well as an averaging filter that can be set depending on the rate at which it will be sampled. The accelerometer has a range of  $\pm 5g$  and a sensitivity of  $\pm 0.001g$ . The IMU takes 819.2 samples per second, but can be read at any power of two lower than that. [22] MicroMAS samples the gyro at 6.4 Hz, which allows it to average its samples at a power of  $2^7$ .

The rate gyro provides information about angular rotation rates about all three axes. These angular rate estimates are treated as first-order derivatives of the quaternion estimate, and are included in the Kalman filtering process for the attitude estimates. The accelerometer estimates are not used in the attitude estimation or control processes, but give information on linear acceleration that the satellite experiences.

### 2.1.1.2 Magnetometer

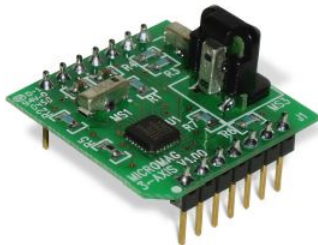


Figure 2-4: PNI MicroMag-3 [23]

MicroMAS has a MicroMag-3 magnetometer, made by the PNI Sensor Corporation. It is a tri-axial magnetometer with a range of  $\pm 1100\mu T$  and a resolution of  $\pm 0.015\mu T$ . [23] The magnetometer is used to take vector measurements of the Earth's magnetic field, and then compare those measurements to an International Geomagnetic Reference Field (IGRF) model. This model is essentially a map around the Earth, which will help the satellite to know which direction it is oriented. The magnetometer is read through the Maryland Aerospace Incorporated (MAI) 400 ADACS unit, but is a separate sensor.

### 2.1.1.3 Sun Sensors



Figure 2-5: Silonex SLSD-717N7 Solderable Planar Photodiode [24]

One of the estimates MicroMAS relies on for coarse attitude estimation is the sun vector. MicroMAS uses Silonex SLSD-717N7 photo diodes sensitive to the visible light spectrum. The

range of detectable wavelengths is 400-1100 nanometers, with a half cone angle of  $60^\circ$ . The photo diodes give a voltage which can then be interpolated to an angle offset, from a chart given in the datasheet. [24] For MicroMAS, the photo diodes are mounted on the satellite's solar panels, four of which are body-mounted and four of which are deployed. In Figure 2-2, the sun sensors are indicated as CSS, which stands for coarse sun sensor, and then numbered from 0 to 5. The sensors are described as coarse because their field of view is 60 degrees, which means that the information they can provide is more uncertain than a sensor with a narrower field of view.

The body-mounted sensors give  $\pm Y$  and  $\pm Z$  knowledge, and the two sensors mounted on deployed panels give constrained  $\pm X$  knowledge. The information in the  $\pm X$  direction is constrained because the solar panels are canted at a 60 degree angle from the centerline of the satellite, and thus do not have their boresight along the x-axis. A more ideal configuration would have photo diodes mounted on each body face of the satellite, so that each boresight looks directly along each body axis. However, this was not possible for MicroMAS, due to the design decision to deploy the panels for better power generation. The specific angle of 60 degrees was chosen to avoid the field of view of the Earth horizon sensors. Despite this constraint, an estimate of the location of the sun can be found by taking the known configuration into account.

Through an algorithm involving the combination of their six voltage measurements, the sun sensors can give a rough direction for the sun when the satellite is not in eclipse. This algorithm takes the raw voltage from each sensor and maps to it the correct body axis. It compares the two voltages from the same axis (the positive and negative) and keeps the larger of the two, as long as the voltage is above the noise floor. The next step is to interpolate that voltage to an angle  $\theta$ , defined as the angle between the sensor boresight and the light source, from a curve given in the photo diode's datasheet based on its responsivity. This

cosine of this angle is then used as the component of the vector.

$$s_{y,z} = \cos(\theta_{y,z}) \quad (2.1)$$

The algorithm then accounts for the limitation in the x-axis by extrapolating the information collected and subtracting the overlapping information from the  $\pm Z$  sensor.

$$s_x = \frac{(\cos(\theta_x) - \sin(\phi)s_z)}{\cos(\phi)} \quad (2.2)$$

The angle  $\phi$  is the angle at which the sun sensors are canted. In the case of MicroMAS, that angle is 60 degrees. These components are then normalized in order to get a unit vector that estimates the direction of the sun in the body frame.

This algorithm was written by the author, with some information from the engineers at Maryland Aerospace Incorporated as to how they computed their own internal sun vector, and supplemented by work from T. Nguyen, a fellow graduate student at MIT. Nguyen contributed the term taking into account the extra knowledge from the overlapping sensor in the  $\pm X$  axis case, which improved the accuracy of the estimate. The estimate was verified using a simulation in the Satellite Tool Kit (STK), which allowed comparison to a solar ephemeris over multiple orbits.

#### 2.1.1.4 Earth Horizon Sensors

MicroMAS is in a low-earth orbit (LEO), and as such spends about one third of its orbit in eclipse, so solely relying on the sun vector is not ideal. The satellite uses thermopiles as Earth horizon sensors (EHS). Thermopiles convert thermal energy into electrical energy, and produce a voltage proportional to a temperature gradient. The TPD 1T 0214 G9 thermopile detector made by Excelitas Technologies senses light in the wavelength between 8 and 14



Figure 2-6: Excelitas Technologies' TPD Thermopile [25]

micrometers, with a sensitivity of  $65\mu V/K$ . Each thermopile has a field of view of 70 degrees. [25]

MicroMAS has two mounts within the MAI ADACS unit, each with 4 thermopile sensors, one on the anti-ram (-X) facing end of the satellite, and the other on the cross-track (+Y) side. The sensors are canted downward at an angle of 22 degrees, corresponding to the sensors seeing the edge of the Earth for the particular orbit of MicroMAS (404 x 424 km). Three of the four thermopiles have masks on them to limit their field of view to 7 degrees, allowing for a much more precise interpolation of voltage to angle. The fourth sensor has no mask, and thus has the 70 degree field of view. This coarse sensor, as it is termed, helps give an estimate of whether the Earth is in the field of view of the sensors. The fine sensors are then used for more precision calculation of the limb location. See paper by T. Nguyen on the details of the algorithm. [26]

The advantage of using the Earth horizon sensors as compared with visible light detectors is that, if the satellite is close to its desired nadir-pointing attitude, the sensors do not lose information in eclipse. The other advantage is that, based on simulation, the EHS algorithm can give knowledge to less than 0.5 degrees.

### 2.1.2 TRIAD Algorithm

The TRIAD algorithm was developed by Harold Black in the 1960s, when he was working for the U.S. Navy to develop a solution to solving for spacecraft attitude. [27] While it is not the optimal solution to attitude estimation, it is simple and not computationally intensive. However, “simulations show that the TRIAD estimate is almost as accurate as the optimal estimate in representative test scenarios”[3].

The algorithm takes two non-parallel reference vectors in an inertial frame, and compares them to two measured vectors in the body frame. [3] It assumes that one vector measurement in the body frame is more accurate than the other, and relies on that measurement for two axes of attitude knowledge. The user can select whichever measurement is more accurate to use as this “more trusted” vector. The TRIAD algorithm then uses the second measured vector to deduce rotational information about the third axis. From this information, a direction cosine matrix is developed, and from that, attitude can be recovered. [3]

The vectors from the magnetometer, the sun sensors, and the Earth horizon sensors are then compared with their respective reference vectors in the inertial frame. The reference vectors are: solar ephemeris for the sun vector; position vector, obtained from the orbit propagator, from the Earth to the satellite is used as a reference for the nadir vector; a vector estimate of the magnetic field, from the International Geomagnetic Reference Field (IGRF) magnetic field model, is used as a reference for the magnetometer measurement.

Each of these reference vectors is dependent on the position and velocity information of the satellite in its orbit. This information is generated by a two-line element uploaded to the satellite, [28] which uses an orbit propagator running on board. The propagator gives orbital position and then calculates the IGRF magnetic field vector and solar ephemeris at that location. Because the TRIAD method only uses two inputs to generate attitude knowl-

edge, it only ever uses two of these sensor options listed in Table 2.1 at a time. Thus, there is a ranking system that uses logic to select which sensor to use to give the most accurate estimate of the attitude at any given time. It should be noted that the accuracy of each sensor measurement is an estimate based on simulation.

Table 2.1: Sensor Rankings for use in TRIAD Algorithm

<b>Expected Error <math>1\sigma</math></b>	<b>Sensor</b>	<b>Measurement Vector</b>	<b>Source of Reference Vector</b>
0.2°	EHS Fine	Nadir Vector	S/C Position
0.7°	EHS Coarse	Nadir Vector	S/C Position
0.5°	Magnetometer	Magnetic Field Vector	IGRF Model
1.5°	Sun Sensors	Sun Vector	Solar Ephemeris

### 2.1.2.1 Sensor Selection

The satellite's attitude determination algorithms use logic to select the highest accuracy sensor options that are available when determining what inputs to use in the TRIAD algorithm. However, because there are two algorithms to solve for the nadir vector (fine and coarse), only one of the EHS nadir vectors can be used by the TRIAD algorithm. If it tried to use both the fine and coarse estimates as measurements, it would be comparing them both to the same reference vector, which still leaves ambiguity about knowledge along one axis. It violates the aforementioned stipulation that TRIAD use two non-parallel reference vectors. Without two non-parallel reference vectors, a direction cosine matrix cannot be constructed. The sensor algorithms will produce all zeros when they do not have enough information to produce a vector, and likewise the references are zeroed until they contain a valid estimate.

Evaluating the validity of each sensor and its corresponding reference is performed via a simple calculation of the magnitude of the vector equal to a non-zero value. Once the two most accurate sensors are selected by the logic, the TRIAD algorithm calculates a quaternion, and this quaternion is then passed into the Extended Kalman Filter.

## 2.2 Extended Kalman Filter (EKF) Application to Attitude Estimation for Satellites

Raw sensor measurements can only give a rough estimate of a state. For this reason, a common choice for real-time state estimation is to use filtering. “Filtering is determining the current state using current (and past) observations”[29]. The Kalman Filter is very popular due to its optimal estimates of the state through propagation and updating, and its relatively simple implementation. By using assumptions of linear dynamics and zero-mean white Gaussian noise processes, the processes can be modeled using linear algebra. “The extended Kalman filter uses the current state estimate to generate a new reference trajectory at each observation....We *predict* the new state estimate based on previous data, and then *update* that result with the new observations”[29].

An extended Kalman filter was used because of the non-linear dynamics involved in spacecraft attitude estimation. The main reference used for this particular implementation of the EKF for is “Kalman Filtering for Spacecraft Attitude Estimation” by E. J. Lefferts, F. L. Markley, and M. D. Shuster. They set forward an application that uses the quaternion estimate of the attitude as the state “augmented by means of additional state vector components for the gyro biases”[30].

Because the estimate of attitude must be updated often in order for a satellite to maintain its true attitude and fight disturbances, it is important for the model of the system to be as accurate as possible. “The Kalman filter uses a dynamical model for the time devel-

opment of the system and a model of the sensor measurements to obtain the most accurate estimate possible for the system state using a linear estimator based on the present and past measurements.” [30] As *Lefferts et al.* remind the reader, using a Kalman filter relies on an accurate dynamical model of the system, which they go on to develop:

*The development of the Kalman filter for the quaternion representation was motivated by the requirement of real-time autonomous attitude determination for attitude control and the annotation of science data. The quaternion parametrization was chosen for several practical reasons: 1) the prediction equations are treated linearly, 2) the representation is free from singularities (thus the gimbal-lock situation is avoided), and 3) the attitude matrix is algebraic in the quaternion component (thus eliminating the need for transcendental functions). [30]*

### 2.2.1 General State Space Representation

In order to illustrate how the filtering process works, it is best to model the state using the state space representation. The general state space representation of a linearized system is represented by the following equations:

$$\dot{\mathbf{x}}(t) = \mathbf{A}(t)\mathbf{x}(t) + \mathbf{B}(t)\mathbf{u}(t) + \mathbf{w}(t) \quad (2.3)$$

$$\mathbf{y}(t) = \mathbf{C}(t)\mathbf{x}(t) + \mathbf{D}(t)\mathbf{u}(t) + \mathbf{v}(t) \quad (2.4)$$

where  $\mathbf{x}(t)$  is the state vector,  $\mathbf{u}(t)$  is the input vector, and  $\mathbf{y}(t)$  is the output vector. The state transition matrix  $\mathbf{A}(t)$  describes the rate of change of the state vector with respect to time. The input matrix  $\mathbf{B}(t)$  describes how the input vector (the controlled input) affects the state. The output matrix  $\mathbf{C}(t)$  describes how the output of the system is related to the state

vector.  $\mathbf{D}(t)$  is the feedthrough matrix, which describes how the input vector affects the output vector. The  $\mathbf{w}(t)$  and  $\mathbf{v}(t)$  terms are represent process and sensor noise respectively in the system. Both are assumed to be white, uncorrelated Gaussian noise processes. These equations are for continuous time.

The model can then be discretized using a power series approach in order to account for the fact that the system will be sampled and updated at discrete time intervals. The subscript  $k$  indicates discretization at a specified time step  $\Delta t$ . [31] For MicroMAS, that  $\Delta t$  is not constant, because the filter is updated both by gyro measurements, which come in at 6.4 Hz, and by attitude estimates, which are sampled at 4 Hz. However, this is not a problem, as long as the  $\Delta t$  is known to the filter. MicroMAS uses an avionics elapsed time (AET) calculated from the microcontroller's crystal oscillator, which gives a time reference for all software events. Thus, each  $\Delta t$  is known.

### 2.2.1.1 State Space Representation of MicroMAS System

For the case of satellite attitude dynamics with the state defined as the quaternion with gyro biases, there is no input vector  $\mathbf{u}$ . To be clear, this is strictly for the filtering case. There is an input vector  $\mathbf{u}$  for control torque that will be discussed in Section 2.3. But, for the purposes of filtering the attitude estimate, there is no input. This means that the second terms are deleted, leaving us with the following discretized state space representation of the system:

$$\mathbf{x}_{k+1} = \mathbf{A}_d \mathbf{x}_k + \mathbf{w}_k \quad (2.5)$$

$$\mathbf{y}_k = \mathbf{C}_d \mathbf{x}_k + \mathbf{v}_k \quad (2.6)$$

### 2.2.1.2 Quaternion Explanation

As *Lefferts et al.* explain, the quaternion representation of the state seems to be the best solution for fast, low-computation attitude estimation. [30] Because of the way a quaternion is defined (its four elements must sum to a unit norm), it only has three independent measurements, while the fourth (or zeroth, in this case) is dependent. Quaternions represent a rotation  $\theta$  along the eigenaxis  $\lambda$  from an arbitrarily defined starting point. Borrowing notation from *Lefferts et al.*, full four-element quaternions will be represented with an overbar  $\bar{\mathbf{q}}$ . Without the overbar, the  $\mathbf{q}$  refers to just the vector components.

$$\bar{\mathbf{q}} \equiv \begin{bmatrix} q_0 \\ q_1 \\ q_2 \\ q_3 \end{bmatrix} \quad (2.7)$$

where

$$q_0 = \cos\left(\frac{\theta}{2}\right) \quad q_i = \lambda_i \sin\left(\frac{\theta}{2}\right), i = 1, 2, 3 \quad (2.8)$$

It is constrained by the following equation:

$$\bar{\mathbf{q}}^T \bar{\mathbf{q}} = 1 \quad (2.9)$$

### 2.2.2 Definition of State Vector

The state vector has seven elements: the four quaternion elements and the three biases from the rate gyros, as shown in equation 2.10. For ease of calculation, all attitude and rate estimates are in the body frame of the satellite, unless otherwise indicated.

$$\mathbf{x} = \begin{bmatrix} q_0 \\ q_1 \\ q_2 \\ q_3 \\ \beta_0 \\ \beta_1 \\ \beta_2 \end{bmatrix} \quad (2.10)$$

In this application, it turns out that the first four elements of the output matrix  $\mathbf{y}_k$  are equivalent to the first four elements of the state matrix  $\mathbf{x}_k$ , because the measurements that are taken are the quaternion  $\bar{\mathbf{q}}_M$ , where the subscript  $M$  indicates a measured quaternion that has not been filtered. The last three elements, the biases on the angular rate, are calculated from the gyroscope measurement  $\bar{\omega}$ , and will be discussed in more detail later.

### 2.2.3 Propagating the State

The process for propagating and updating the state is shown in Figure 2-7. The first equation, starting from the block on the far left of Figure 2-7, is the relationship of the expected next state from the previous state. In discrete time,  $k + 1$  indicates the next time, while  $k$  represents the current time. The state, or system, matrix contains the expression that takes the state,  $\hat{\mathbf{x}}$ , from time  $k$  to time  $k + 1$ . The hat over the  $x$  indicates that it is an estimate of the state, as the actual true state is unknown. The covariance of the state is described by the  $\mathbf{P}$  matrix. It is made up of pre and post multiplication of the previous covariance by the state matrix, as well as an addition of the  $\mathbf{Q}$  matrix, which contains information on the process noise in the system.

To have the most optimal filtering solution, the strategy is to use all information avail-

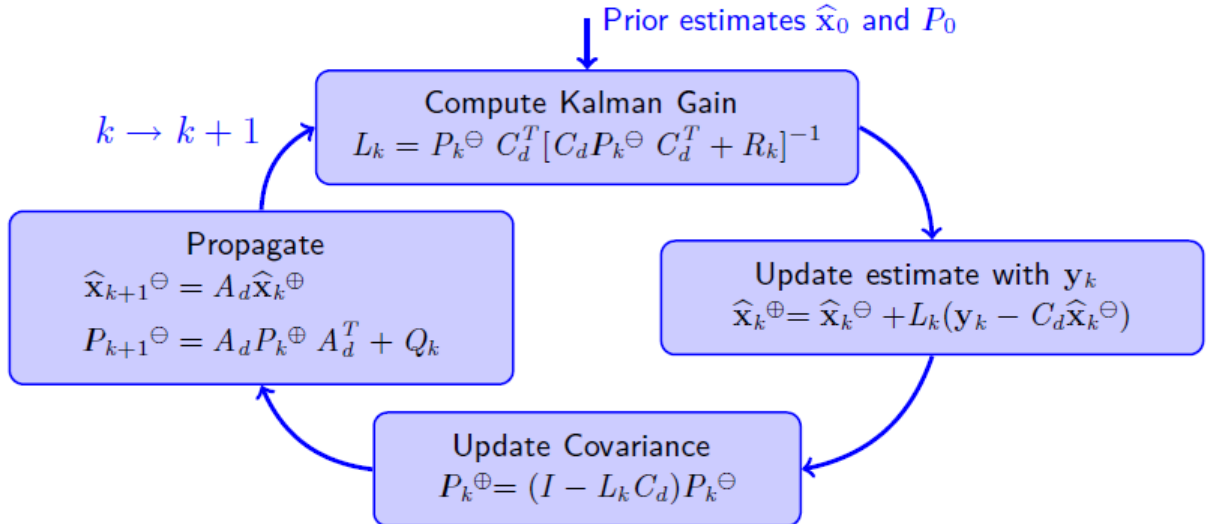


Figure 2-7: Discrete Kalman Filter Recursive Loop [32]

able: all past measurements as well as present measurements. The superscripts  $\oplus$  and  $\ominus$  represent these notions. The  $\ominus$  symbol represents an estimate that uses all past information, while the  $\oplus$  represents an estimate that uses both past and present information. An estimate before a measurement update is denoted by  $\ominus$ , and an estimate after it has been updated is represented by  $\oplus$ .

$$\hat{x}_{k+1}^\ominus = \mathbf{A}_d \hat{x}_k^\oplus \quad (2.11)$$

$$\mathbf{P}_{k+1}^\ominus = \mathbf{A}_d \mathbf{P}_k^\oplus \mathbf{A}_d^T + \mathbf{Q}_k \quad (2.12)$$

Each matrix represented in equations 2.11 and 2.12 will be discussed in more detail in the following sections.

### 2.2.3.1 Modeling Angular Rate

The estimated angular rate  $\boldsymbol{\omega}$  is a vector containing three elements of angular rate in right-hand rule orthogonal reference frame. The angular rate estimate comes from the direct measurement of angular rate  $\bar{\boldsymbol{\omega}}$  from the inertial measurement unit, with a bias  $\boldsymbol{\beta}$  and noise  $\boldsymbol{\eta}_v$  subtracted. It is modeled as a first-order Markov process, as shown in equations 2.13 and 2.14 [31].

$$\boldsymbol{\omega} = \bar{\boldsymbol{\omega}} - \boldsymbol{\beta} - \boldsymbol{\eta}_v \quad (2.13)$$

$$\dot{\boldsymbol{\beta}} = \boldsymbol{\eta}_u \quad (2.14)$$

The noise is modeled as a zero-mean Gaussian white noise, and the bias is expected to drift, with its rate of change also a zero-mean Gaussian white noise process. The relationship of the angular rate to the attitude estimate is that of a rate of change. Thus, the gyro rates are used to help predict how the attitude estimate will change over a discrete period of time  $\Delta t$ .

### 2.2.3.2 Defining the State Matrix

Because of the quaternion dynamics, and the estimation of the bias of the gyro being directly related to the attitude estimate itself and not its own dynamics, the quaternion is the only part of the state that is propagated. In other words, the gyro biases are dependent upon the attitude estimate and are not independent variables. Therefore, the state matrix  $\mathbf{A}_d$  is only 4x4, as shown in equation 2.15. Thus, the state matrix shows the direction relationship between the estimate of angular rate  $\boldsymbol{\omega}$  and the corresponding prediction of the attitude over a specified amount of time,  $\Delta t$ .

$$\mathbf{A}_d = \begin{bmatrix} \cos\left(\frac{|\omega| \Delta t}{2}\right) & \frac{\omega_x}{|\omega|} \sin\left(\frac{|\omega| \Delta t}{2}\right) & \frac{\omega_y}{|\omega|} \sin\left(\frac{|\omega| \Delta t}{2}\right) & \frac{\omega_z}{|\omega|} \sin\left(\frac{|\omega| \Delta t}{2}\right) \\ -\frac{\omega_x}{|\omega|} \sin\left(\frac{|\omega| \Delta t}{2}\right) & \cos\left(\frac{|\omega| \Delta t}{2}\right) & \frac{\omega_z}{|\omega|} \sin\left(\frac{|\omega| \Delta t}{2}\right) & -\frac{\omega_y}{|\omega|} \sin\left(\frac{|\omega| \Delta t}{2}\right) \\ -\frac{\omega_y}{|\omega|} \sin\left(\frac{|\omega| \Delta t}{2}\right) & -\frac{\omega_z}{|\omega|} \sin\left(\frac{|\omega| \Delta t}{2}\right) & \cos\left(\frac{|\omega| \Delta t}{2}\right) & \frac{\omega_x}{|\omega|} \sin\left(\frac{|\omega| \Delta t}{2}\right) \\ -\frac{\omega_z}{|\omega|} \sin\left(\frac{|\omega| \Delta t}{2}\right) & \frac{\omega_y}{|\omega|} \sin\left(\frac{|\omega| \Delta t}{2}\right) & -\frac{\omega_x}{|\omega|} \sin\left(\frac{|\omega| \Delta t}{2}\right) & \cos\left(\frac{|\omega| \Delta t}{2}\right) \end{bmatrix} \quad (2.15)$$

### 2.2.3.3 Defining the Covariance Matrix

The covariance matrix  $\mathbf{P}_k$  represents the uncertainty of the estimate of the state. The diagonals of the matrix represent the error expected on the estimate, and the off-diagonal terms represent coupling between the various elements of the states. Initially, the covariance matrix is set to correspond to the three-sigma bounds of error expected for each element of the state. This comes from noise on the sensors, as well as process noise.

The covariance matrix for this particular implementation is a 6x6 matrix, as it contains information on the attitude estimate as well as the bias on the angular rate estimate. Again, the quaternion, though it contains four elements, contains only three independent measurements. Essentially, the scalar element is a scaling factor and can be disregarded in terms of calculating error. *Lefferts et al.* and *Crassidis* go into a more detailed explanation of the singularity involved in a full 7x7 covariance matrix, and various ways to get to a 6x6 matrix. Those methods are not presented here, but the initial state of the 6x6 covariance matrix is shown in equation 2.16.

$$\mathbf{P}_{k=0} = \begin{bmatrix} \sigma_{q_1}^2 & 0 & 0 & 0 & 0 & 0 \\ 0 & \sigma_{q_2}^2 & 0 & 0 & 0 & 0 \\ 0 & 0 & \sigma_{q_3}^2 & 0 & 0 & 0 \\ 0 & 0 & 0 & \sigma_{\beta_0}^2 & 0 & 0 \\ 0 & 0 & 0 & 0 & \sigma_{\beta_1}^2 & 0 \\ 0 & 0 & 0 & 0 & 0 & \sigma_{\beta_2}^2 \end{bmatrix} \quad (2.16)$$

As seen in Figure 2-7 and equation 2.12, the covariance will change each time the EKF runs, so equation 2.16 simply represents the initial conditions for the covariance.  $\mathbf{P}_k$  will adjust to accurately represent the uncertainty in the filter's estimation of the state based updates from measurements of the state  $\mathbf{y}_k$ .

The  $\mathbf{Q}_k$  matrix is formulated in equation 2.17, where  $\sigma_u^2$  and  $\sigma_v^2$  are the constant estimates of the covariance of the process noise, and  $\Delta t$  is the amount of time from the previous estimate to the current estimate. Thus, the  $\mathbf{Q}_k$  matrix is re-calculated during each Kalman filter update, since the time between updates  $\Delta t$  will vary slightly.

$$\mathbf{Q}_k = \begin{bmatrix} \sigma_u^2 \Delta t + \frac{\sigma_v^2 \Delta t^3}{3} & 0 & 0 & \frac{\sigma_v^2 \Delta t^2}{2} & 0 & 0 \\ 0 & \sigma_u^2 \Delta t + \frac{\sigma_v^2 \Delta t^3}{3} & 0 & 0 & \frac{\sigma_v^2 \Delta t^2}{2} & 0 \\ 0 & 0 & \sigma_u^2 \Delta t + \frac{\sigma_v^2 \Delta t^3}{3} & 0 & 0 & \frac{\sigma_v^2 \Delta t^2}{2} \\ \frac{\sigma_v^2 \Delta t^2}{2} & 0 & 0 & \sigma_v^2 \Delta t & 0 & 0 \\ 0 & \frac{\sigma_v^2 \Delta t^2}{2} & 0 & 0 & \sigma_v^2 \Delta t & 0 \\ 0 & 0 & \frac{\sigma_v^2 \Delta t^2}{2} & 0 & 0 & \sigma_v^2 \Delta t \end{bmatrix} \quad (2.17)$$

Essentially, this  $\mathbf{Q}_k$  matrix tells the filter how much noise to estimate, based on the expected process error and the amount of time the estimate was propagated before being updated.

#### 2.2.3.4 Kalman Gain

The Kalman gain term,  $\mathbf{L}_k$  is formulated from a combination of the covariance matrix  $\mathbf{P}_k$ , the sensor noise  $\mathbf{R}_k$ , and the output matrix,  $\mathbf{C}_d$ . Of course, since this gain term is applied to propagate the state, it has the superscript  $\ominus$  indicating that the covariance has not been updated by the measurement yet. This optimal gain term yields the minimum mean-square error estimates of the state, provided that all of its inputs accurately reflect the system.

$$\mathbf{L}_k = \mathbf{P}_k^\ominus \mathbf{C}_d^T [\mathbf{C}_d \mathbf{P}_k^\ominus \mathbf{C}_d^T + \mathbf{R}_k]^{-1} \quad (2.18)$$

#### 2.2.4 Updating the State with the Innovation

The Kalman gain is then applied to the measurement to update the estimate of the state. The subtraction of the last state estimate  $\hat{\mathbf{x}}_k^\ominus$  multiplied by the output matrix  $\mathbf{C}_d$  from the measurement  $\mathbf{y}_k$  is called the innovation. The innovation is then multiplied by the Kalman gain  $\mathbf{L}_k$  and added to the previous state estimate  $\hat{\mathbf{x}}_k^\ominus$  to solve for the most updated state estimate  $\hat{\mathbf{x}}_k^\oplus$ . Thus, this innovation term reveals how close the estimate of the state is to the measurement, and the gain weights the new measurement against its prediction, to compute the best estimate of the true state, as shown in equation 2.19.

$$\hat{\mathbf{x}}_k^\oplus = \hat{\mathbf{x}}_k^\ominus + \mathbf{L}_k (\mathbf{y}_k - \mathbf{C}_d \hat{\mathbf{x}}_k^\ominus) \quad (2.19)$$

The covariance is updated in a similar manner, shown in equation 2.20.

$$\mathbf{P}_k^\oplus = (\mathbf{I} - \mathbf{L}_k \mathbf{C}_d) \mathbf{P}_k^\ominus \quad (2.20)$$

#### 2.2.4.1 Quaternion Innovation and Update

Because quaternions cannot simply be added or subtracted to find the sum or difference due to their unique definition (see equations 2.8 and 2.9), quaternion multiplication is used. The difference in quaternion from the propagated estimate  $\hat{\mathbf{q}}^\oplus$  to the measured quaternion  $\bar{\mathbf{q}}_M$  is the quaternion innovation, where quaternion multiplication of the inverse of the the estimate represents a subtraction.

$$\delta\bar{\mathbf{q}} = \hat{\mathbf{q}}^\oplus \otimes \bar{\mathbf{q}}_M^{-1} \quad (2.21)$$

Assuming that the estimated quaternion is very close to the measured quaternion, the following approximation can be made, where the scalar term is dropped and the vector terms of the innovation are doubled. [31]

$$\delta\mathbf{q} = \begin{bmatrix} 2q_{e1} \\ 2q_{e2} \\ 2q_{e3} \end{bmatrix} \quad (2.22)$$

This three-dimensional vector representing attitude innovation can be multiplied by the 3x3 Kalman gain matrix, in order to update the estimate of the quaternion. The resulting change in scalar can be calculated based on the requirement that the unit norm of the 4-element quaternion be 1.

$$\hat{\mathbf{q}}_i^\oplus = \hat{\mathbf{q}}_i^\oplus + \frac{1}{2}(\mathbf{L}_k \delta\mathbf{q}), \quad i = 1, 2, 3 \quad (2.23)$$

$$q_0^\oplus = \sqrt{1 - 1/4(\delta\mathbf{q} \cdot \delta\mathbf{q})} \quad (2.24)$$

The update for the other three elements of the state, the biases from the gyro measurements, are calculated via subtraction of the vector quaternion error  $\delta\mathbf{q}$  multiplied by the Kalman gain. For small angles, the vector quaternion error can be approximated in units of half

radians. Thus, a multiplication by 2 is required to convert to radians. Qualitatively, the bias on the angular rate must agree with the quaternion innovation – that is, with the difference between the propagated estimate and the measurement as scaled by the Kalman gain.

$$\boldsymbol{\beta}^{\oplus} = \boldsymbol{\beta}^{\ominus} - \mathbf{L}_k (2\delta\mathbf{q}) \quad (2.25)$$

### 2.2.5 Summary of EKF Process

To summarize, the process for filtering the estimates is as follows:

1. Take a measurement of the system,  $\bar{\mathbf{y}}_k$ .
2. Propagate the state from the previous time to the time of measurement,  $\hat{\mathbf{x}}_{k-1}^{\oplus} \rightarrow \hat{\mathbf{x}}_k^{\ominus}$ .
3. Compute the innovation, based on the measurement and the propagated estimate,  $(\bar{\mathbf{y}}_k - \mathbf{C}_d \hat{\mathbf{x}}_k^{\ominus})$ .
4. Update the state estimate with the innovation,  $\hat{\mathbf{x}}_k^{\ominus} \rightarrow \hat{\mathbf{x}}_k^{\oplus}$ .

Thus, the Extended Kalman Filter works by the interweaving of propagation and update steps, and uses all information available to get the best estimate of the state.

## 2.3 Control Law Theory

### 2.3.1 Actuators

The law of conservation of momentum is the driving idea behind actuation in most nanosatellites. Thrusters, which operate using Newton's third law, can also be used for rotation and translation, but are not often used in nanosatellites, due to complications with launch requirements and inherent propellant limitations. MicroMAS uses a Maryland Aerospace



Figure 2-8: Maryland Aerospace Incorporated 400 Mini ADACS Unit [33]

Incorporated (MAI) 400 Miniature Attitude Determination and Control System (ADACS) unit, which includes three orthogonally mounted reaction wheels and three magnetorquers.

### 2.3.1.1 Reaction Wheels

Reaction wheels are simply wheels that are driven by motors with the purpose of introducing momentum into the satellite system. Because momentum must be conserved in a closed system, the addition of this momentum causes the satellite to rotate. Thus, applying torque to the system via reaction wheels is a means of rotating the satellite along the axis of rotation of the wheel. With three wheels mounted orthogonally, a rotation about any arbitrary axis is achievable through the correct combination of torque to the three wheels.

Of course, there is a limit on the amount of torque that the wheels can provide. Once the reaction wheels have reaches their maximum speed, they are no longer able to provide torque. The process of lowering the wheel speed slowly, while offsetting the torque produced during this spin-down, is called de-saturating the reaction wheels. Magnetorquers are often used for this process.

### **2.3.1.2 Magnotorquers**

Magnetorquers, or torque rods, are rods of metal to which electric current is applied. This current is flowed through these metal rods, which produces a magnetic dipole moment, in units of current multiplied by area. When this dipole interacts with the ambient magnetic field, it produces a torque that is perpendicular to both the induced current and the ambient magnetic field. This torque can also induce rotation. The torque able to be generated by the magnetorquers is of about a factor of 10 lower than the torque produced by the reaction wheels. However, the magnetorquers never saturate, because they can always carry electric current. Thus, using magnetorquers together with reaction wheels is the best option to have the most control torque available. Magnetorquers can be used to help dump momentum from, or de-saturate, the reaction wheels such that they can continue to provide torque.

The maximum torque that the wheels can provide is 0.635 milliNewton-meters (mN-m), with a momentum storage capacity of 0.10 milliNewton-meter-seconds (mN-m-s). The wheels can spin up to  $\pm 10,000$  revolutions per minute (rpm), and can receive commands by torque or speed. The resolution of the torque commands is 0.005 mN-m. The maximum dipole that can be commanded to the magnetorquers is  $\pm 0.15$  Ampere-meters-squared ( $\text{Am}^2$ ), at a 72% duty cycle, which yields an approximate dipole of  $\pm 0.108 \text{ Am}^2$ . The resolution of the magnetorquer commands is about  $\pm 0.6\%$  duty cycling. Duty cycling can be linearly scaled to approximate the resultant dipole for the purposes of calculating torque, since the torque depends on the strength of the magnetic field over a period of time.

### **2.3.2 B-Dot Algorithm**

One objective of satellite attitude control is simple rate damping. Observations of how the magnetic field changes as a function of time are used in a simple but powerful way to mitigate

tumbling, called B-dot control. This consists of simply applying a torque in the opposing direction that matches the rate of change of the magnetic field. [34]

$$\dot{\mathbf{B}}(t) = -\boldsymbol{\omega}(t) \times \mathbf{B}(t) \quad (2.26)$$

$$\mathbf{m}(t) = -k\dot{\mathbf{B}}(t) \quad (2.27)$$

$$\boldsymbol{\tau}_C(t) = \mathbf{m}(t) \times \mathbf{B}(t) \quad (2.28)$$

The rate of change of the magnetic field  $\dot{\mathbf{B}}(t)$  can be sensed by the angular rotation of the satellite  $\boldsymbol{\omega}(t)$  crossed with the instantaneous magnetic field vector  $\mathbf{B}(t)$ . The dipole that is desired to be applied by the torque rods in order to damp out this rotation is represented by  $\mathbf{m}$ , where it is simply proportionally related by some selected gain  $k$  applied to that observed rate of change. Thus, the control torque that results  $\boldsymbol{\tau}_C$  is the cross product of that dipole with the magnetic field. This dipole that effects the torque is applied by magnetorquers. The B-dot control law shown in equations 2.27 and 2.28 is commonly used for Earth-orbiting spacecraft for slowing the rate of rotation, and allows the spacecraft to damp out motion in any direction except that which is aligned directly along the magnetic field vector. [34]

### 2.3.3 Linear Quaternion Feedback Estimator

After a satellite has reached a low enough angular rate that it can be controlled, control theory can be applied to the system to direct its dynamics. Control is near impossible at higher rates because the amount of torque that would be required exceeds the abilities of the actuators of MicroMAS, and most nanosatellites. [20] It has been shown that the most optimal rotational maneuver in terms of conservation of total distance traveled is what is called an eigenaxis rotation. The control algorithm implemented here is based on a controller

for spacecraft eigenaxis rotations developed by *Wie et al.* in 1989. The quaternion feedback regulator “consists of linear feedback of error quaternions and body rates, and includes decoupling control torque that simply counteracts the natural gyroscopic coupling torque” [35].

### 2.3.3.1 Definitions of Torque

The design *Wie et al.* presented is essentially a proportional-derivative controller with an added gyroscopic-torque canceling term. It is developed below. First, we begin with the definition of torque as the time rate of change of angular momentum of a system, seen in equation 2.29.

$$\boldsymbol{\tau} = \frac{d\mathbf{L}}{dt} \quad (2.29)$$

Torque and angular momentum are both 3x1 vectors, in the body frame of the satellite. Angular momentum is defined as the product of the mass moment of inertia of a rigid body with its angular rotation rate, shown in equation 2.30. The moment of inertia is a 3x3 matrix, representing the major inertias about each axis, as well as all of the cross-coupling terms.

$$\mathbf{L} = \mathbf{J}\boldsymbol{\omega} \quad (2.30)$$

Using the assumption of rigid body dynamics, the mass moment of inertia (or just inertia for short)  $\mathbf{J}$  of the system has a time rate of change of zero. It is standard to make this assumption for satellites, and is a good approximation to first-order. Of course, deflection of solar panels and rotation or translation of any components will shift the inertia. However, this motion is considered to be negligible for the development of the controller presented here, but is being actively studied by another graduate student at MIT. [17]

Using the rigid-body assumption, the torque can then be derived to be the product of the inertia with the time rate of change of the angular rate of a rigid body about its fixed

center of mass.

$$\boldsymbol{\tau} = \mathbf{J}\dot{\boldsymbol{\omega}} \quad (2.31)$$

Knowing this, we define Euler's equations of rotational motion of a rigid body about its fixed center of mass in the body frame.

$$\mathbf{J}\dot{\boldsymbol{\omega}} = \boldsymbol{\Omega}\mathbf{J}\boldsymbol{\omega} + \mathbf{u} \quad (2.32)$$

where  $\boldsymbol{\omega}$  is the 3x1 vector containing angular rate of the satellite in the body frame and  $\mathbf{u}$  term is the 3x1 vector containing the control torque applied to the system. Unlike in the Kalman filtering case, the control input is non-zero. The  $\boldsymbol{\Omega}$  term is a 3x3 skew-symmetric matrix defined in equation 2.33.

$$\boldsymbol{\Omega} \equiv \begin{bmatrix} 0 & -\omega_3 & \omega_2 \\ \omega_3 & 0 & -\omega_1 \\ -\omega_2 & \omega_1 & 0 \end{bmatrix} \quad (2.33)$$

This term is necessary in describing the dynamics of rotational motion.

### 2.3.3.2 Describing Attitude Error

Quaternions were defined and described in Section 2.2 as arguably the best way to describe angular rotation of a rigid body, since they avoid singularities and are computationally simple. As described in Section 2.2.4.1, a simple subtraction to solve for attitude error will not suffice. The measured and filtered quaternion  $\hat{\mathbf{q}}$  must be inverted and then quaternion multiplied by the commanded quaternion  $\bar{\mathbf{q}}_C$  to get the innovation, in a similar manner as before in equation 2.21.

$$\bar{\mathbf{q}}_e = \bar{\mathbf{q}}_C \otimes \hat{\mathbf{q}}^{-1} \quad (2.34)$$

For small attitude changes, and for cases where the reference quaternion is [1,0,0,0], the error quaternion can be approximated as again as it was in equation 2.22, where the vector elements of the quaternion innovation are multiplied by 2 to convert to radians. In fact, for small angles, this approximation of attitude error is equivalent to the traditional Euler angles.

$$2q_{e,i} = \theta_i \quad i = 1, 2, 3 \quad (2.35)$$

where  $\theta_i$  corresponds to roll, pitch, and yaw, respectively. The subscript  $e, i$  on the quaternion represents the error in the vector components of the quaternion, as represented in equation 2.22. This approximation converts the calculated error in quaternion from a 4-dimensional term to a three-dimensional term that can be used in a controller with a three-axis system.

### 2.3.3.3 Introducing the Proposed Control Torque

The quaternion feedback regulator proposed by *Wie et al.* “for eigenaxis rotations consists of linear error-quaternion feedback, linear body-rate feedback, and a nonlinear body-rate feedback term that simply counteracts the gyroscopic coupling torque”[35]. The control torque is the **u** term represented in equation 2.32, and the only term over which control systems engineers actually have any control, as the other terms are all parts of the system. (There may be limited ability of the engineer to change the mass moment of inertia **J** of the system. But, since it is largely determined by other factors, the control engineer must deal with it as a reality of the system.)

The control torque given by *Wie et al.* is a combination of the non-linear dynamics of gyroscopic forces internal to the system introduced by spinning reaction wheels, a derivative feedback term, and a proportional feedback term. The torque due to the gyroscopic forces

is represented by the skew symmetric matrix  $\boldsymbol{\Omega}$  (as defined in equation 2.33) multiplied by the inertia  $\mathbf{J}$  and the angular rotation rate  $\boldsymbol{\omega}$  of the system. The derivative term is simply a 3x3 constant gain matrix  $\mathbf{K}_d$  multiplied by the measured angular rotation rate  $\boldsymbol{\omega}$  of the satellite. The proportional term is also a constant 3x3 gain matrix  $\mathbf{K}_p$  multiplied by the measured attitude error  $\delta\mathbf{q}$ , as defined in equation 2.22.

$$\mathbf{u} = -\boldsymbol{\Omega}\mathbf{J}\boldsymbol{\omega} - \mathbf{K}_d\boldsymbol{\omega} - \mathbf{K}_p\delta\mathbf{q} \quad (2.36)$$

As the angular rotation rates and the quaternion error, and inertia are all pre-determined (measured or fixed) by the response of the system, the tools at the engineer's disposal for this controller are the 3x3 constant gain matrices  $\mathbf{K}_d$  and  $\mathbf{K}_p$ . *Wie et al.* go on to describe how to define these derivative and proportional gain terms to best achieve the eigenaxis rotation and ensure stability. They conclude that the gain terms should be scalar multiples of the inertia matrix  $\mathbf{J}$ , termed  $d$  and  $k$ . The next steps are how to select the scalar values  $d$  and  $k$  appropriately.

#### 2.3.3.4 Solving for Gain Terms

An eigenaxis rotation is defined as the shortest angular path between two orientations. The angle  $\phi$  through which an eigenaxis rotation takes place is always smaller than the algebraic sum of the three Euler angles. As it turns out, the three vector parts of the quaternion form a unit vector along the eigenaxis. [35] If we let  $\boldsymbol{\lambda}$  represent this unit vector along the eigenaxis, the vector components of the quaternion can be defined as in equation 2.37.

$$\mathbf{q} = \sin\left(\frac{\phi}{2}\right)\boldsymbol{\lambda} \quad (2.37)$$

If one then assumes that angular rate is small, and that the gyroscopic term can be neglected, the control law from equation 2.36 can be re-arranged to form equation 2.38. [35]

$$\left( \ddot{\phi} + d\dot{\phi} + k \sin\left(\frac{\phi}{2}\right) \right) \mathbf{J}\boldsymbol{\lambda} = 0 \quad (2.38)$$

In equation 2.38 describing eigenaxis rotation through an angle  $\phi$ , the general second-order order equation of motion is proportional to the product of  $J$  and the unit vector along the eigenaxis  $\boldsymbol{\lambda}$ . Knowing that both the inertia of the rigid body and the eigenaxis unit vector are non-zero allows those terms to be dropped. For the purposes of selecting gains, *Wie et al.* make the small angle approximation for  $\frac{\phi}{2}$ , such that  $\sin\left(\frac{\phi}{2}\right) \approx \frac{\phi}{2}$ , so that equation 2.38 reduces to a clean second-order linear equation:

$$\ddot{\phi} + d\dot{\phi} + k \left( \frac{\phi}{2} \right) = 0 \quad (2.39)$$

This then allows for the gains to be selected using the damping coefficient and natural frequency via the relationships derived from the traditional second-order canonical form:

$$\ddot{\phi} + 2\zeta\omega_n\dot{\phi} + \omega_n^2\phi = 0 \quad (2.40)$$

where  $\zeta$  is the damping coefficient and  $\omega_n$  is the natural frequency of the system. By setting equations 2.39 and 2.40 equal to each other, the relationships governing the determination of the scalar gains  $d$  and  $k$  can be found.

$$d = 2\zeta\omega_n \quad \frac{k}{2} = \omega_n^2 \quad (2.41)$$

The control engineer can select damping coefficient and natural frequency to get the desired response, and then use equation 2.41 to solve for the gains to apply to the controller to effect

this response.

*Wie et al.* point out that due to the non-linearity introduced by the  $\sin\left(\frac{\phi}{2}\right)$  term, a modified settling time relationship of  $\frac{8}{\zeta\omega_n}$  should be employed when selecting  $\zeta$  and  $\omega_n$ , rather than the usual  $\frac{4}{\zeta\omega_n}$ . [36] Practically speaking, this modification simply means that when choosing the desired response of the system, a slightly different equation must be used to solve for the parameters  $\zeta$  and  $\omega_n$ .

Global stability is guaranteed by this choice of gains, since  $d$  and  $k$  are positive scalars, and the inertia matrix of the rigid body  $\mathbf{J}$  is positive definite, as *Wie et al.* show in Section IV of their paper. In addition, they studied the effect of uncertainty of the inertia matrix - an important practical sensitivity analysis, since it is often difficult to quantify the exact inertia properties of an object. They concluded that their presentation of gain selection is not only optimal, but also globally stable and robust to uncertainty in the inertia matrix. However, the caveat is that, “[t]he price we pay for robustness is that the rotation is not performed about the eigenaxis” if the inertia estimate is not exactly correct [35].

## 2.4 Control Law Implementation for a Dual-Spinner CubeSat

It is this presentation of a globally stable, eigenaxis rotation based on quaternion error and rate gyro feedback upon which the control law for MicroMAS is based. We started with the control torque presented in *Wie et al.*, shown above in equation 2.36. The gains were selected according to the method presented in equation 2.41, with  $\zeta$  chosen to be the standard choice of  $\frac{1}{\sqrt{2}}$ , and  $\omega_n$  chosen as  $\frac{2\pi f_s}{100}$ , where  $f_s$  is the controller sample frequency. Thus, the

proportional and derivative terms of the control law are:

$$\boldsymbol{\tau}_k = \omega_n^2 \mathbf{J} (2\delta\mathbf{q}) \quad (2.42)$$

$$\boldsymbol{\tau}_d = 2\zeta\omega_n \mathbf{J} \delta\boldsymbol{\omega} \quad (2.43)$$

where the  $2\delta\mathbf{q}$  term is the quaternion innovation, from equation 2.22. The error in angular rate is described in equation 2.44, where the subscript  $C$  indicates the commanded rate, and the subscript  $M$  indicates the measured rate (with gyro biases added).

$$\delta\boldsymbol{\omega} = \boldsymbol{\omega}_C - \boldsymbol{\omega}_M \quad (2.44)$$

The gyroscopic term is employed as presented in equation 2.36, with the addition of the angular momentum due to the rotation of the reaction wheels as well as that of the spinning payload. Thus, the gyroscopic-canceling term is:

$$\boldsymbol{\tau}_g = \boldsymbol{\Omega} (\mathbf{J}\boldsymbol{\omega} + \mathbf{L}) \quad (2.45)$$

where  $\boldsymbol{\Omega}$  is the skew symmetric matrix as defined in equation 2.33 and  $\mathbf{L}$  is the angular momentum of the reaction wheels and the payload, as expressed below:

$$\mathbf{L} = J_{RW} \boldsymbol{\omega}_{RW} + (J_P \boldsymbol{\omega}_P) \hat{\mathbf{n}} \quad (2.46)$$

$J_{RW}$  is the scalar value of the inertia of a reaction wheel about its axis of rotation. It is assumed that the three orthogonally-mounted reaction wheels are all share the same mass and inertia properties, which allows that term to be a scalar, rather than a 3x1 vector. The  $\boldsymbol{\omega}_{RW}$  term refers to the 3x1 vector of angular velocity of the reaction wheels, each respectively about its axis of rotation. Since the wheels are orthogonally mounted, their angular

velocities can be combined neatly into a 3x1 vector. The  $J_P$  term contains the scalar value of the rotating payload, along with the components of the motor that rotate with it, about its axis of rotation. For MicroMAS, this payload is axi-symmetric about its axis of rotation, and aligned along one of the body axes. That reduces the angular velocity to a scalar term, since its freedom of rotation is only along one axis. To preserve the final term as a vector, it is simply multiplied by the unit vector  $\hat{\mathbf{n}}$ , which converts the term to a 3x1 vector. For MicroMAS,  $\hat{\mathbf{n}}$  is  $[1,0,0]^T$  since the payload's spin axis is aligned with the body x-axis of the satellite.

## 2.4.1 Introducing New Terms to the Control Vector

### 2.4.1.1 Integrator

The terms presented in equations 2.42, 2.43, and 2.45 cover the three terms presented by *Wie et al.* in their quaternion feedback regulator control design. However, as mentioned in the introduction, MicroMAS implements a PID control law, which means that it contains, in addition to the proportional and derivative terms outlined above, an integral term. Traditionally, integrator terms are added to control laws in order to help drive the system to its desired state faster, as well as eliminate any steady-state error due to disturbances. The danger of integral terms is that they can cause a system to overshoot its desired state, and – if the gain is chosen improperly – can cause the system to become unstable.

Since the PD controller presented by *Wie et al.* was shown to be globally stable, the reader may question why we decided to add an integral term. The decision was made during testing of the algorithms on hardware, when we observed that the system appeared to have a constant steady-state attitude error. Thus, the integral term provides extra torque in the same direction as the proportional term to help the satellite get to its desired attitude. Because of the known dangers of introducing an integral term, and having no desire to

introduce instability into the system, the gain for the integrated error term was selected to be only 10% of the proportional gain.

$$\boldsymbol{\tau}_i = \frac{\omega_n^2 \mathbf{J}}{10} \int_0^t (2\delta\mathbf{q}) dt \quad (2.47)$$

In addition to making the integral term a factor of ten smaller than the proportional term, saturation on the attitude error was imposed. This limits runaway integrator error, and ensures slower rotations, or slews. The saturation on the attitude error is 5 degrees, and on the integral of the error it is 10 degrees. This limitation will prevent the proportional and integral terms from dominating the control torque, and thus keep the rotation actuation slower.

To illustrate this in an example, the satellite is poised at some arbitrary attitude and some initial small, but non-zero, tumbling rate. For the MicroMAS mission, this control law is not implemented until after the satellite has detumbled, so it is safe to assume that this rate is less than one degree per second. If this arbitrary attitude in which the satellite finds itself is 100 degrees from its commanded position, and if the quaternion error were not saturated, this attitude error would drive the control law and saturate the control torque commands to the actuators. It would begin to slew at a high rate toward its commanded attitude. The problem with a high slew rate is that the satellite's momentum is entirely self-contained. Thus, any momentum that it introduces to the bus by slewing, it must then transfer back to the reaction wheels once it reaches its commanded attitude. A fast transfer of momentum requires a large amount of torque, which is limited in a reaction wheel set sized for CubeSats. To avoid saturating the reaction wheels, and because the maneuver for the MicroMAS mission does not need to be fast, saturation terms were imposed.

### 2.4.1.2 Feed Forward

The dynamics of a dual spinner require another term to counter the torque provided by the spinning up of the payload. Once the rotation reaches a constant rate, the gyroscopic term in equation 2.36 would account for the extra momentum added to the system. But, during that spin-up phase, we determined that a feed-forward torque term should be added to cancel the torque provided by the motor and its attached payload.

The addition of this term is extremely simple and based on the definition of torque, presented above in equation 2.29, where the torque on a system is equal to its inertia multiplied by the angular acceleration. When the spinning object, in this case the payload, is spinning up, its acceleration is non-zero and introduces a torque to the system. If it is not accounted for, the bus will begin to rotate, observing the law of conservation of momentum. It is for this reason that a new term must be introduced into the control torque,  $\mathbf{u}$ .

$$\boldsymbol{\tau}_{ff} = (J_P \alpha_P) \hat{\mathbf{n}} \quad (2.48)$$

The subscript indicates that this is the feedforward term, and it consists simply of the product of the inertia of the rotating payload and the angular acceleration of the payload. It is multiplied again by the unit vector  $\hat{\mathbf{n}}$  that relates the orientation of the payload's spin axis to the body frame.

Thus, the overall control law implemented for the dual-spinning case is the following:

$$\mathbf{u} = -\boldsymbol{\Omega}(\mathbf{J}\boldsymbol{\omega} + \mathbf{L}) - \omega_n^2 \mathbf{J}(2\delta\mathbf{q}) - \frac{\omega_n^2 \mathbf{J}}{10} \int_0^t (2\delta\mathbf{q}) dt - 2\zeta\omega_n \mathbf{J}\delta\boldsymbol{\omega} - (J_P \alpha_P) \hat{\mathbf{n}} \quad (2.49)$$

The first term in equation 2.49 accounts for gyroscopic forces due to angular momentum of internal components. The next three terms account for proportional, derivative, and integral feedback, respectively. The last term is the feed-forward term, which accounts for the

acceleration of the payload. This control law can be applied to any small satellite, and it is the testing of this control law, on real satellite hardware, that will be discussed further in Chapters 4, 5, and 6.

# Chapter 3

## Constraints and Facilities for ADCS Tests

### 3.1 Space Environment

The overarching goals of testing the attitude determination and control system of a satellite in a laboratory environment are to validate that the system will, in fact, work as it was designed to. The previous control engineer on the project, 1Lt Evan Wise, USAF, wrote his master's degree thesis on a very detailed and thorough simulation of the satellite, including the Extended Kalman Filter and control theory presented in the previous chapter. With this simulation in place, the next logical step to ready the satellite for flight was to test these algorithms on hardware, and to try to simulate as many aspects of space environment as possible, bearing in mind not only the limitations in the test environment, but also of the actuation capabilities of a CubeSat. Due to its constrained size, any actuators must also be very small, limiting their actuation abilities. These abilities are even further constrained when placed in a test environment where the disturbances are an order of magnitude higher than the expected disturbances on orbit. [15]

Some of these aspects of the space environment are: microgravity, Earth's magnetic field, radiation, extreme cold, and vacuum. Of course, there are limitations in the ability to simulate all of the aspects of the space environment, and often they have to be tested one at a time, rather than all at once. For testing attitude determination and control, the constraints of microgravity and the Earth's magnetic field are the most relevant. However, it is important to address the concerns that the other hazards present, and how best to mitigate them.

### 3.1.1 Microgravity

Every object with mass is attracted to every other object with mass in proportion to the product their masses, and with inverse proportion to the square of the distance between the objects. Earth is the most massive object that is close enough to a satellite to exert a strong force. But as objects escape into orbit, that distance between the masses increases, and due to the inverse relationship to force, the gravitational force on the satellite decreases.

$$F_G = G \frac{m_1 m_2}{r^2} \quad (3.1)$$

On orbit, a satellite experiences what is commonly referred to as microgravity. This is simply a condition where the force  $F_G$  experienced by the less massive object  $m_2$  is virtually zero (or very small) because the distance  $r$  from the more massive object  $m_1$ . This allows the satellite to have complete freedom of rotation, or tumble as it is often called. Because satellites often have requirements to be pointed in a certain way in order to accomplish their mission, they must be able to maneuver in this environment to orient themselves to their desired attitude.

### 3.1.2 Earth's Magnetic Field

Earth's magnetic field is another aspect of the space environment that satellites, especially small satellites, rely heavily upon. The Earth is surrounded by a magnetic field, generated largely by electric currents in its liquid iron outer core. [37] The geodynamo, as it is called, is called is a rotating, convecting, and electrically conducting fluid which creates a magnetic field. This field nominally acts as a dipole, although it is distorted by solar wind, which causes a magnetosphere around the Earth. [37]

The Earth's magnetic field vector over various altitudes and locations has been modeled by

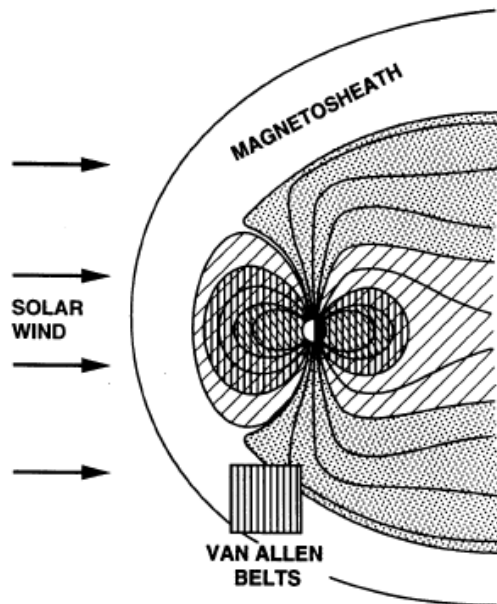


Figure 3-1: Earth's Magnetic field and magnetosphere [37]

the International Association of Geomagnetism and Aeronomy (IAGA). The Earth's magnetic field varies according to altitude and location in orbit, and a satellite can be controlled by taking advantage of this knowledge. Spacecraft magnetometers measure the magnetic field in three orthogonal axes, which are then compared against a model of magnetic field values of Earth at the altitude and inclination of the satellite's orbit. This measurement,

when coupled with other sensor knowledge, helps to provide the satellite's attitude determination and control subsystem (ADCS) with some knowledge of location and pointing direction. The magnetic field experienced by a satellite in orbit is different than that on the surface of the Earth. For example, on the surface of the Earth, the magnetic field mainly acts as a dipole, where the magnetic field vector points to magnetic north; on orbit, the field direction fluctuates in a roughly sinusoidal manner, since the satellite is circling the dipole. The actual numerical values of the field components on orbit are of the same orders of magnitude as on the surface (in the neighborhood of  $50 \mu\text{T}$ ), with the major difference being that on orbit, the field will be changing as the satellite travels around the Earth, while in a laboratory environment on the surface of the Earth, the field is roughly constant.

MicroMAS uses a 6th order IGRF 2010 model to map the magnetic field. According to Wise's analysis, having only six coefficients can lead to attitude errors of up to almost a degree. However, the ADACS unit was constrained by limited CPU availability. [33] In addition, internal sources of magnetism within the spacecraft can lead to biases in the magnetometer measurements. Many spacecraft do residual dipole tests in order to characterize this interference. This was a particular concern for MicroMAS, since it has a relatively large motor that rotates using permanent magnets. However, preliminary testing showed that the placement of the magnetometer on the bottom interface board (farthest away from the motor) was sufficient to reduce any disturbance in measurement to noise.

### 3.1.3 Radiation

Radiation is a difficult phenomenon to simulate over extended periods of testing. If a project's schedule and budget allows, total ionizing dose (TID) radiation testing can be done on hardware. For low-earth orbit (LEO) missions, the TID effects are limited, because the satellite is still largely protected by Earth's magnetic field. However, single-event upsets (SEUs) caused

by electromagnetic radiation striking a sensitive component, can be a concern. Most large satellite programs implement countermeasures such as triple-mode redundancy and voting circuits. [19]

However, CubeSats do not have the luxury of this kind of architecture, due to their constrained processing capabilities. What MicroMAS does to mitigate risk of SEUs is to use what is called a watchdog timer, which catches software faults and takes appropriate measures if a fault is detected. [19] For attitude control testing, the importance is that the dangers have been considered and mitigated as well as budget, schedule, and design constraints allow. [38]

### 3.1.4 Cold Space and Vacuum

Thermal and vacuum tests often occur simultaneously for testing spacecraft. Vacuum chambers are sealed containers that allow the air pressure to be pumped down from the ambient air pressure to a desired value, thus representing the vacuum environment of space. These chambers also often can be connected with liquid nitrogen tanks, which lower the temperature inside the chamber, simulating the cold of space. Heater plates can be placed inside to simulate solar flux or heating from other internal components. Walls of these thermal vacuum chambers have high-emissive properties that allow the temperature to be maintained at the desired level.

However, because resting a satellite inside a chamber limits any freedom of motion, the application to validation of ADCS algorithms and hardware is limited. Thermal and vacuum are more functionality tests to ensure that the hardware performs as expected under those conditions. An important consideration that the MicroMAS team learned from thermal vacuum testing is that biases on sensors can be affected by a hot or cold environment. These biases should be monitored, and if possible, modeled and compensated for in order to ensure

that the sensor still gives representative information on-orbit.

## 3.2 Simulating Microgravity

### 3.2.1 Challenges and Constraints

When testing a system, there are two important considerations: objectives and constraints.

In order to design a test, the object of the test must be clear: the test must prove  $x$  to within  $y$  bounds. But in order to design the test, the engineer must understand the constraints imposed by resources available. In testing small satellites, the environments listed above are all challenges that are unique from that of systems that operate on the Earth's surface. Simulating the space environment to an acceptable level, while considering resource and timing constraints of the project is the challenge of small satellite testing.

The Space Systems Laboratory at MIT has a spherical air bearing surrounded by a Merritt 4-coil design Helmholtz Cage for attitude determination and control testing. [37] This set-up enables simulation of the two aspects of the space environment that are most relevant for attitude determination and control: free tumble and magnetic field actuation. In fact, the magnetic field provides both determination and control for MicroMAS, since its attitude control law uses the magnetometer as a sensor to an attitude estimate, and it contains torque rods which enable actuation against the ambient magnetic field.

### 3.2.2 Spherical Air Bearing

A common way to simulate the freedom of rotation that an object experiences in microgravity is to use what is called an air bearing. Spherical air bearings allow for complete freedom

of rotation without external torque along one axis, and limited freedom of rotation along the other two axes. This is achieved by suspending a hemisphere in a cup with a constant supply of air, which allows the hemisphere freedom of motion within the cup. The test object is then secured, usually by screws, to the flat part of the hemisphere. The freedom of rotation is achieved using the same principles that allow a puck to float on an air hockey table. This allows complete freedom of rotation about one axis, as well as observance of coupling to other axes, since the two off-axes still have limited freedom of rotation. A photograph of a spherical air bearing is shown in Figure 3-2.

The spherical air bearing located in MIT's Space Systems Laboratory allows for com-



Figure 3-2: Spherical Air Bearing [39]

plete freedom of rotation about its vertical axis, and up to 30 degrees of tip and tilt along the other two axes. It has mounting holes that allow various objects to be mounted to it, and can support loads of up to 10,000 kg. [39] An air hose is connected up through an aluminum post that supports the cup, allowing the hemisphere to float. Innovative mounting schemes allow one the option of testing any axis of control for small (or not so small) satellite systems.

One of the challenges of using the spherical air bearing set up is the extreme precision required when balancing the test articles. Because the hemisphere operates in free float, it is critical that the center of mass is co-located with the center of rotation. For systems to

be pendulum stable, the center of mass should be below the center of rotation. If the center of mass is above the center of rotation, the system will be unstable. The optimal situation is to have the center of mass coincident with the center of rotation, so that the system is neither pendulum stable nor dynamically unstable, and will thus respond more like it would in a microgravity environment.

Co-locating the center of mass precisely with the center of rotation turns out to be quite difficult in practice. Even with a very well-planned design, with the mass and inertia properties calculated in a three-dimensional mechanical computer-aided design (CAD) program, centering the mass with the center of rotation is an iterative process. MicroMAS initially had a “flat-sat” design that mounted its components on the underside of a quarter-inch aluminum plate, as shown in Figure 3-3. The boardstack, with the sensors attached, as well as the MAI-400 ADACS unit are shown on the left. The scanner assembly and a payload simulator are on the right. Six C-cell batteries are mounted on the top left, for power and also to help to balance the rig. There is also an antenna that enables the “flat-sat” to communicate wirelessly. The air bearing rig has three mass adjusters with micrometer stages, one for each axis, to help incrementally shift the center of mass.

### 3.2.3 Limitations of Air Bearing Tests

While this platform was designed with much care, it proved to less than optimal. Even though the mass moment of inertia had been predicted and was adjustable with the masses mounted on the micrometer stages, centering the mass of the test rig proved extremely challenging. Any shift in distribution of mass would offset the system’s total center of mass. For a CubeSat program that is testing attitude determination and control of a dual-spinner, this becomes a real problem.

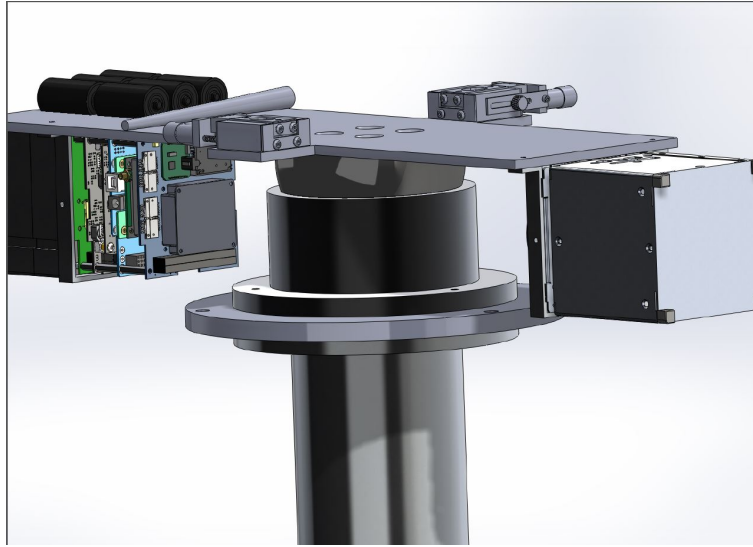


Figure 3-3: MicroMAS “Flat-Sat” for Air Bearing Testing [17]

### 3.2.3.1 Co-Location of the Center of Mass with the Center of Rotation

A payload simulator, also known as the payload “mass mock-up” was machined out of aluminum for demonstration purposes and attitude control tests. Even though it was machined to reflect the inertia properties of the real payload, the simulator was not perfectly axi-symmetric about its axis of rotation, due to machining tolerance limitations. [17] Because of this, the payload’s rotation necessarily causes a change in mass distribution of the system, which makes it near impossible to keep the center of mass co-located with the center of rotation. The result is that the test platform becomes either unbalanced or unstable, making attitude control tests difficult.

Another graduate student working with the same spherical air bearing set-up in the SSL encountered similar problems, with an even more minute mass offset. The student was testing fine pointing control with a piezo stage, which would move only a few micrometers and had a mass of about 200 grams [15]. This proved to both students that any mass shift at all had an effect on their pointing control tests. Since MicroMAS’s rotating payload simulator was mounted all the way out on the end of the platform, the inertia of the rig changed even

more drastically.

The initial solution that we adopted was to test the system in a dynamically stable mode, where the center of mass was located just below the center of rotation. This essentially limited the tests to one axis of freedom of rotation (yaw), since any rotation in tip (pitch) and tilt (roll) would be fighting a very strong gravitational torque. This torque due to gravity exceeds the torque capabilities of the actuators. Even after making the test platform just barely pendulum stable, it still had to be re-balanced after each test, due to rotation of the payload simulator during the test.

Attempts at this method of testing imposed two hardships on the validation of the MicroMAS ADCS algorithms. The first was that only one axis could be tested, and even the cross-axis terms could not be observed due to the inherent stability of the system. Coupled with this limitation is that the platform was designed such that the components would be permanently situated. In order to test more than one axis, the platform would have to be dis-assembled and subsequently reassembled. The system was also very sensitive to any initial torque imparted when it was released. Even with the stability, an oscillation could take many minutes to damp out, and also frustrate the controller.

The second limitation was the immense amount of time that had to be expended to balance the system before every trial. Even to get the system to be pendulum stable took at least half an hour at the beginning of each day of testing, and 10-15 minutes between tests. On a budget and schedule-constrained program like a CubeSat, this time loss was a major limitation.

### 3.2.3.2 Inflated Inertia Properties

Another limitation in this design was the large mass moment of inertia of the test platform. The components had to be mounted below the plate, in order to keep the center of mass

at least as low as the center of rotation of the hemisphere. In order to avoid coming in contact with the hemisphere, they had to be mounted at a distance out from the center of the system. Because the moment of inertia  $J$  of a rigid body is proportional to the square of the distance from its center of mass, any offset  $r$  causes a large increase in inertia.

$$J = mr^2 \quad (3.2)$$

The inertia of the “flat-sat” turned out to be approximately a factor of three greater than the inertia of the real satellite. Since torque required to effect rotation is proportionally related to the object’s moment of inertia, a design with a large moment of inertia severely limits the angular acceleration that the torque can effect. Actuators for CubeSats are already limited in their ability to provide torque. In practical terms, the inflated inertia of the test platform means that the ability of the actuators to effect rotational maneuvers is severely limited. Due to these limitations in the design space to utilize the spherical air bearing for attitude determination and control tests, we took another approach.

### 3.2.4 Uniaxial Attitude Control Tests: “Piñata” Rig

In order to avoid the frustrations that using the spherical air bearing for testing involved, we sought another way to test the satellite’s control algorithms involving freedom of rotation. Another approach to test control algorithms which allows for some freedom of rotation is suspension. The ExoCube satellite by Cal Poly also used this approach in their ADCS tests. [40] The specific test set-up that was devised entails a monofilament string with tensile strength rated to hold up to 50 pounds with a hook on the end to hold the test article. An engineering model (EM) of the satellite was constructed, which includes duplicates of the printed circuit boards that are relevant to the ADCS. A CAD model of this EM unit is

shown in Figure 3-4.

It has a few modifications that are different from the actual satellite, such as a dif-

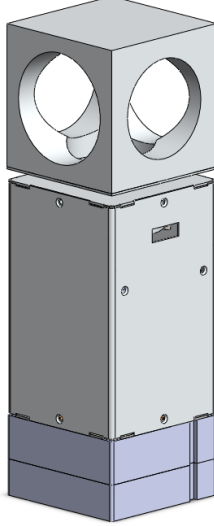


Figure 3-4: CAD Model of Engineering Unit MicroMAS Satellite [17]

ferent battery board and a different radio. However, these differences do not affect ADCS testing. The EM satellite also has engineering units of all sensors and actuators, excluding sun sensors and Earth horizon sensors. The inertia of this EM unit is roughly the same as inertia of the flight satellite without solar panels deployed, to first order. Figures 3-5a and ?? show CAD models of the two satellites side by side, with the chassis transparent so that the boardstacks within are visible.

Suspending the EM satellite by a string allows it limited freedom of rotation about the axis perpendicular to the floor. It is limited because the string exerts a restoring torque on the EM satellite, which can be modeled as a simple damped harmonic oscillator:

$$\tau_r = -k\theta_d - c\dot{\theta}_d \quad (3.3)$$

The restoring torque  $\tau_r$  has two terms: one proportional to the displacement in angular position from the neutral, untwisted string position  $\theta_d$ , and the damping term, which is due

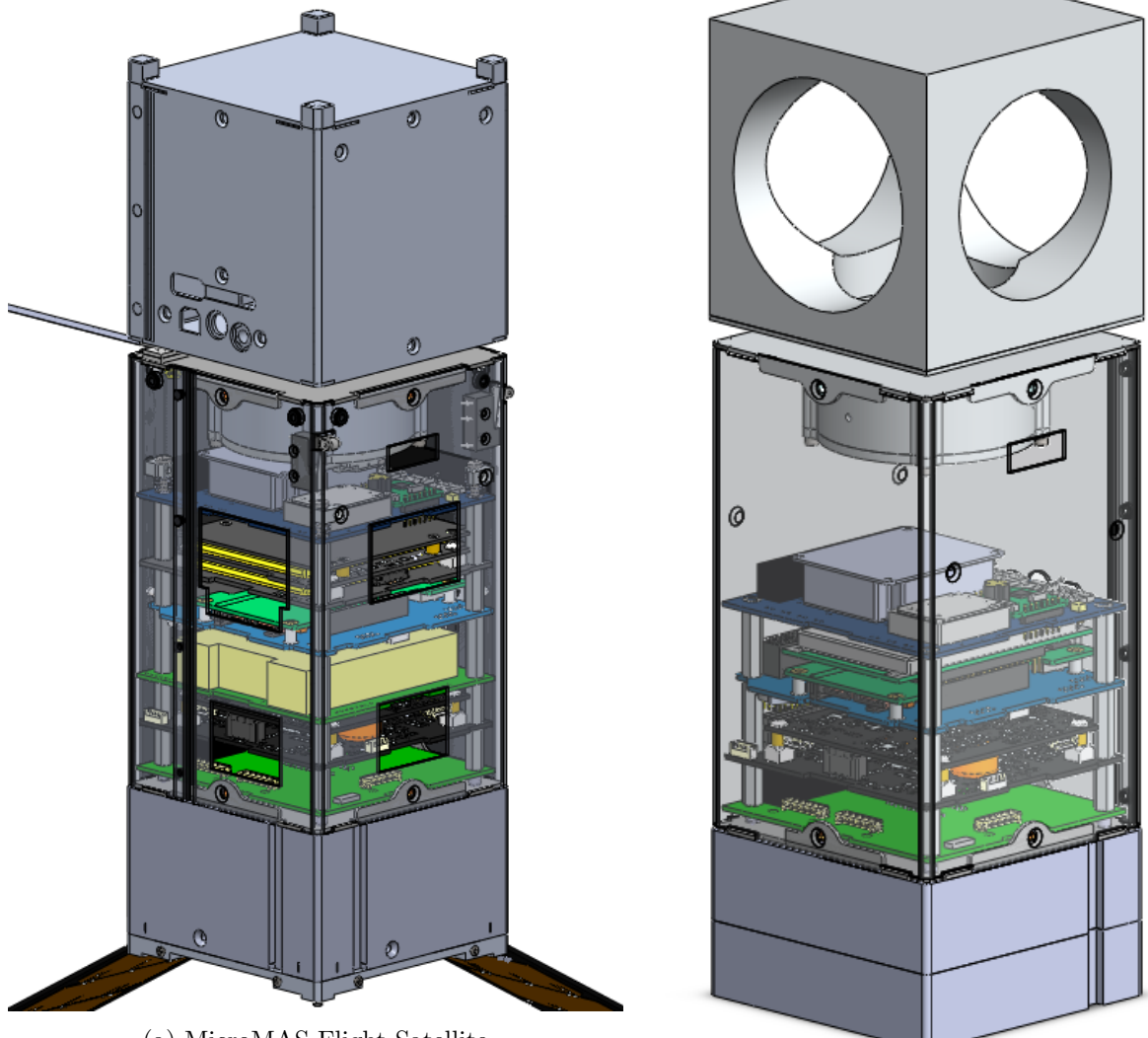


Figure 3-5: Comparison of EM and Flight Satellites with Transparent Chassis

to friction inherent in the system, which is simply proportional to the rate of oscillation  $\dot{\theta}_d$ . The proportional terms  $k$  and  $c$  are properties of the string, which determine how much it resists twisting. In this set-up, the goal is to have a string that is strong enough with factors of safety to hold the satellite, but also flexible enough to twist without providing much resistance (small values of  $k$  and  $c$ ).

While this suspension tactic for testing introduces a new torque term that the control law must fight, it can be limited by keeping the angular displacement small. Specific strategies for this testing will be discussed further in the Chapter 4. This set-up does allow for, like the spherical air bearing, relative freedom of rotation about one axis. It is also easy and quick to set up and take down, and does not impose extra inertia constraints on the system. If a modular rig is designed, the satellite can be rotated such that all three axes of actuation can be tested without much time lost to dis-assembly and reassembly. Thus, while the “piñata” rig’s freedom of rotation is more limited, it proved to be a useful set-up for attitude control testing of a CubeSat.

### 3.2.5 Zero-G Tests

Ideally, to test attitude control systems on small satellites, a true microgravity environment is desirable. MicroMAS was fortunate enough to have been selected by NASA’s Reduced Gravity Program to go on what is called a “zero-g” flight. These flights consist of a modified Boeing 727 aircraft that flies in parabolas in order to exert enough force within the aircraft to counter the force of gravity, thus simulating a microgravity environment. [41] Objects in the cargo bay of the aircraft experience the free-fall associated with a microgravity environment for limited periods of time.

These moments of “zero-g” only last about 20 seconds at a time, and thus great care must be taken in devising the tests to be accomplished. Because the aircraft environment

does not afford the stimuli for the sensors used in the satellite’s attitude determination, only the control aspect of the ADCS system was tested. Since the controller MicroMAS employs requires attitude information, a simple first-order numerical integration was performed on the rate gyro measurements. In this way, all three axes of the control law could be observed in a true microgravity environment, albeit in limited time intervals.

## 3.3 Earth’s Magnetic Field

### 3.3.1 Helmholtz Cage

Three-axis Helmholtz cages for small satellite and CubeSat ADCS testing have been developed at universities and commercial and government research facilities in the United States and abroad. Note that in this paper, the term “Helmholtz” cage refers to a multi-axis paired-coil system for controlling magnetic fields, as it was first described by Hermann von Helmholtz in 1849. [42] Helmholtz cages utilize the principle of the Helmholtz coil, but applied in three orthogonal axes. When current is applied to two coils of the same diameter, a uniform magnetic field is produced at the separation distance of one radius between the two coils. [37] The equation for a Helmholtz coil is derived from the Biot-Savart law:

$$\mathbf{B} = \frac{\mu_0}{4\pi} \int_C \frac{Id\ell \times \mathbf{r}}{|\mathbf{r}^3|} \quad (3.4)$$

which describes the magnetic field  $\mathbf{B}$  generated by a steady current  $I$  at a position specified in three-dimensional space  $\mathbf{r}$ . The differential  $d\ell$  term describes the length of wire over which the integral is being calculated, and  $\mu_0$  is simply a constant. Note that the field is largest when the length of the wire  $\ell$  and the position  $\mathbf{r}$  are perpendicular to one another, due to the cross product. The length of the wire is a 3x1 vector, representing which axes the length

of wire runs along with respect to the  $3 \times 1$  position vector. The integral is around a closed curve, as denoted by the subscript  $C$ . [42] The equation for the magnetic field generated at the center of two equally sized coils is then:

$$B = \left(\frac{4}{5}\right)^{3/2} \frac{\mu_0 n I}{r} \quad (3.5)$$

The reader will notice that equation 3.5 has only scalar terms, while the equation it was derived from, equation 3.4, has vector terms. This is because the field being calculated is in the direction perpendicular to the plane of the coils. The distance  $r$  is simply a scalar representing the distance between the coils, as well as the radius of the coils. The scalar term  $n$  represents the number of windings of the wire. It is interesting to note that the number of windings has a multiplicative effect overall field produced.

Taking equation 3.5 and applying it along three orthogonal axes, one can now have control over all three components of the magnetic field produced in the center of the coils. Thus, the purpose of a Helmholtz cage, for aerospace applications, is to simulate Earth's magnetic field (or a scaled version of it) in order to test the spacecraft's magnetometer, magnetically controlled actuators (e.g., magnetorquers), and control algorithms.

### 3.3.2 Merritt 4-Coil Helmholtz Cage

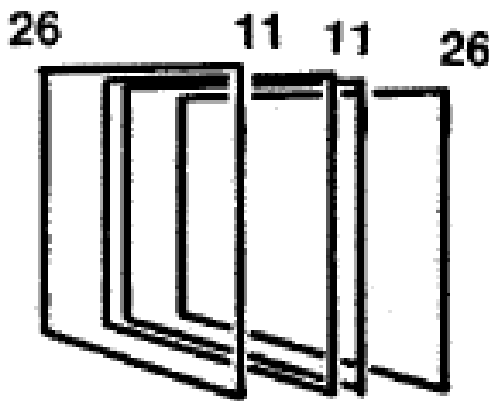
MIT's Space Systems Laboratory's Helmholtz Cage was built in January of 2013. Its purpose is to allow for control of the ambient magnetic field, including the reproduction of Earth's magnetic field on orbit, in order to stimulate the attitude determination and control for small satellites. The overarching objective of the cage was to implement a system that optimizes the volume of uniform magnetic field within the cage, while maintaining a size that is modular enough for CubeSats to ESPA-class satellites.

The approach often used in satellite pointing control assumes that the inertial rate of change of the magnetic field is negligible with respect to the command rate (the command rate is often between one to ten Hertz for many small satellite applications). Any changes in the magnetic field observed by the magnetometer in terms of the body reference frame in this short time scale are attributed to uncontrolled rotation (tumbling), rather than translation. A uniform field is important because control algorithms work from detecting slight changes in the field.

### 3.3.2.1 Merritt 4-Coil Implementation

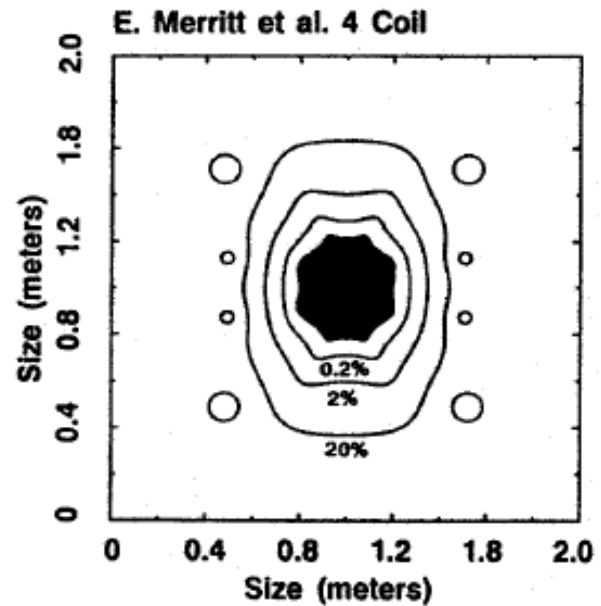
Ensuring a uniform field is critical to testing this control. Maximizing the volume of this uniform region allows for greater flexibility in the articles to be tested. *Kirschvink* used numerical methods in 1992 to calculate the field uniformity of six different types of magnetic coil systems, and found that the Merritt 4-Coil design optimizes the area of uniform magnetic field in one dimension[43]. In addition, this design does not compromise the interior access to the uniform field, and as such was the best candidate for creating a large volume of uniform, controllable, magnetic field for attitude control and determination testing. The Merritt 4-coil design requires four square coils for each axis, a total of 12 coils for a three-axis cage, twice as many as the standard 6-coil Helmholtz cages. Each axis has four square coils as shown below. The outer two coils each have 26 turns of wire, and the inner two each have 11 turns. Calculations estimate the generated field to be uniform within 0.1% in the center volume. According to Kirschvink, the Merritt 4-coil design “yield[s] the largest volume of uniform field space” of the six options numerically analyzed.

In Figure 3-6a, the four coil design is shown, where the numbers represent the relative ratio of coil wrappings, and the spacing shown represents the ratio at which the coils must be spaced apart to achieve the uniform field within. Figure 3-6b shows the volume of the



**E. Merritt et al. 4 Coil**

(a) Coil-Wrappings and Spacing [43]



(b) Uniformity of Magnetic Field Produced [43]

Figure 3-6: Properties of Merritt 4-Coil Design

uniform field within the coils, where the percentage represents deviation from the desired uniform field. The black octagonal shape in the middle shows the area of the field that is uniform to within 0.1%. The ratio of the wire wrappings, as well as the spacing between the coils, are the determining factors for the uniformity of the field produced inside. Table 3.1 summarizes the design parameters.

Table 3.1: Merritt 4-Coil Design Parameters [37]

Coil Shape	No. of Coils	Coil length or diameter	Coil space wrt center of system	Ampere-turn ratios	Central Field ( $\mu T/A$ )
square	4	d, d, d, d	-0.5055d, -0.1281d, +0.1281d, +0.5055d	26/11/11/26	46.65/d

This particular spacing of the coils, with the winding ratio listed, is able to produce a uniform magnetic field with about the magnitude of the Earth's magnetic field with only one Ampere of current applied.

### **3.3.2.2 Expanding to Three Axes**

To implement this design in three axes, a strategy was needed in order to fit the coils within each other. The four-coil per axis design of the cage led to a nesting of the coils within each other. In order for four coils in three axes to coexist, the coils for each axis must be of a slightly different size, which allows nesting during assembly. The z-axis square coils were selected to be the largest, at a side length of 59 inches (1.4986 meters). This size was chosen in order to encompass a large enough space for testing of a CubeSat engineering model, and small enough to fit within the existing volume in the lab around the spherical air bearing. The x-axis coils are the medium coils, at a side length of 57 inches (1.4478 meters). The y-axis coils are the smallest, at a side length of 55 inches (1.397 meters).

Each axis of the 4-coil design is shown in Figure 3-7. The field produced by each set of coils is perpendicular to the plane of the coils. With all three sets of coils combined, a magnetic field in all three axes can be produced, with individual control over each axis. The final construction is shown in the photograph in Figure 3-8.

### **3.3.2.3 Controlling the Magnetic Field Within the Cage**

The desired magnetic field is then converted to the current required to drive the coils, based on the number of turns. Simply converting equation 3.4 to solve for the current given the commanded field, the equation for the commanded electrical current is:

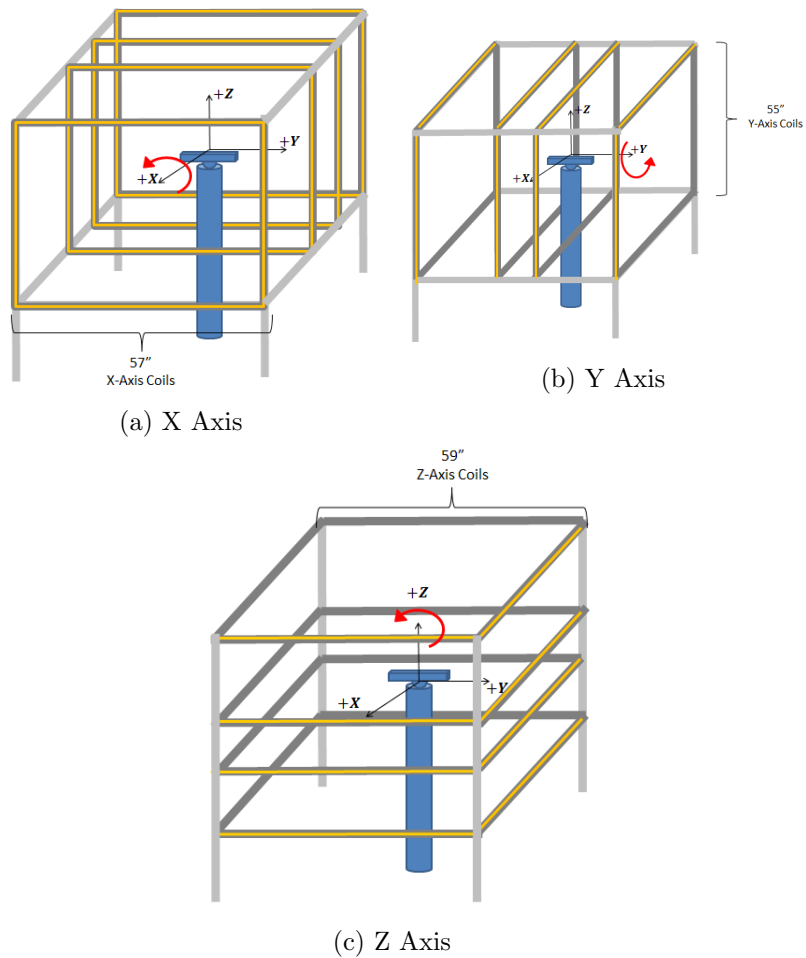


Figure 3-7: Implementation of 4-Coil Design around Spherical Air Bearing [37]



Figure 3-8: MIT Space Systems Laboratory's Helmholtz Cage [37]

$$\mathbf{I} = \mathbf{B} \frac{\mu_0}{4\pi} \int_C \frac{nd\ell \times \mathbf{r}}{|\mathbf{r}^2|} \quad (3.6)$$

The variables for each coil were the number of windings  $n$ , the length of each side and its orientation with respect to the center of the cage  $d\ell$ , the radial distance of the center of the side with respect to the center of the cage  $\mathbf{r}$ . So, for each set of coils, there were in fact sixteen different calculations (4 coils times 4 sides) involved to calculate what the current should be in order to produce a desired magnetic field along that one axis. Because each coil is made up of four straight pieces of wire, each side could be approximated as a line integral and the center of each segment was taken to be its position.

The desired current is calculated for each of the three components of the magnetic field.

This value is then quantized between 0 and 255, passed through an open-source microcontroller, and converted to an analog signal to a power amplifier, which then is connected with audio wire to the coils. The design uses audio power amplifiers which have adjustable gain values, and also allow for a constant bias adjustment. Each axis is controlled by one channel on the power amplifiers, which is in turn controlled by the serial interface with the microcontroller. The wire used to connect the power amplifiers to the copper wire of the coils is 16 gauge speaker cable. A block diagram of the system is shown in Figure 3-9.

A method for adjusting the gain and bias was developed in order to command the same

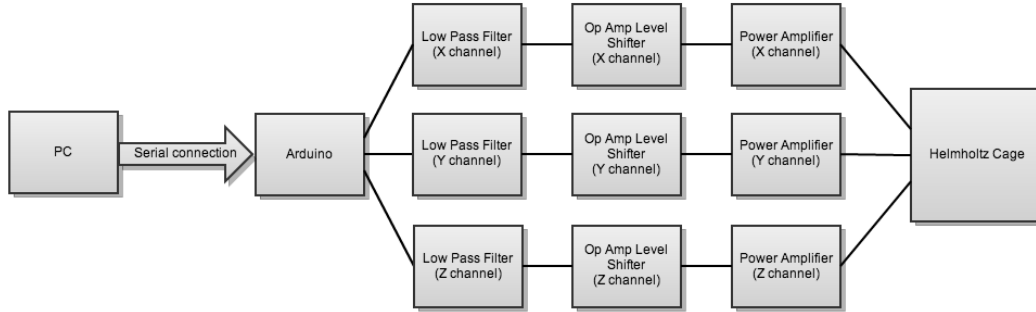


Figure 3-9: Block Diagram of Helmholtz Cage Interface [37]

increment of field change with each serial command, as well as to zero the ambient magnetic field. A sensitive magnetometer was placed in the center of the cage, and its readings were used for calibration of the commands. The cage was calibrated using an Applied Physics Systems' Fluxgate 520 magnetometer, which has a resolution of  $10^{-10}$  Tesla [44], a factor of  $10^3$  more precise than was needed for a small satellite application.

First, the gains on the power amplifiers were adjusted such that the maximum serial command would produce  $50 \mu\text{T}$  and the minimum serial command would produce  $-50 \mu\text{T}$  for each axis. Since each the coils for axis are a slightly different size, this gain is slightly different on each axis to achieve the same resultant increment of magnetic field. Next, the

biases were adjusted for each axis such that at a median serial command, the field inside the cage would be  $0 \mu\text{T}$ .

The uniformity, as well as the cross-coupling between axes, of the magnetic field produced within the cage was measured. Figures 3-10 and 3-11 show the magnetic field measured along the x-axis and y-axis, respectively, inside the cage when all three axes were commanded to  $0 \mu\text{T}$ . The z-axis was more difficult to measure, since the post holding the air bearing pedestal was in the middle. However, the x- and y-axes results give information about the plane of uniform field, and their results can be extrapolated to the z-axis.

At each location along the axis, there are 600 data points collected by the magnetometer

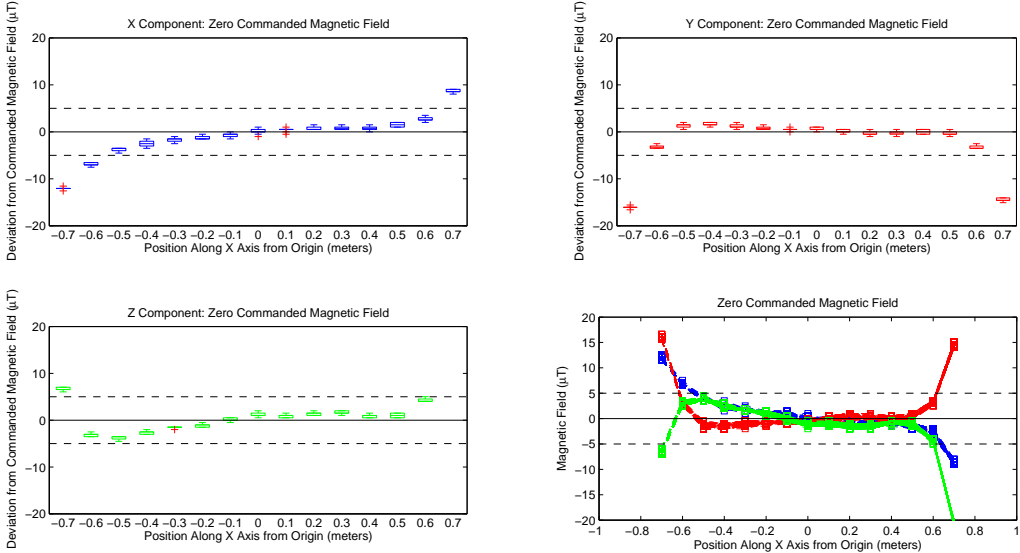


Figure 3-10: Uniformity of Helmholtz Cage Along X-Axis

over the course of 6 seconds. The top two and bottom left plots show boxplots that represent the deviation of the measured field from the commanded field. The top left plot shows the x-component of the field in blue, the bottom left plot shows the y-component of the magnetic field in green, and the top right plot shows the z-component of the magnetic field in red. The bottom right plot shows all three components plotted on top of each other. The dotted lines represent  $\pm 5 \mu\text{T}$ .

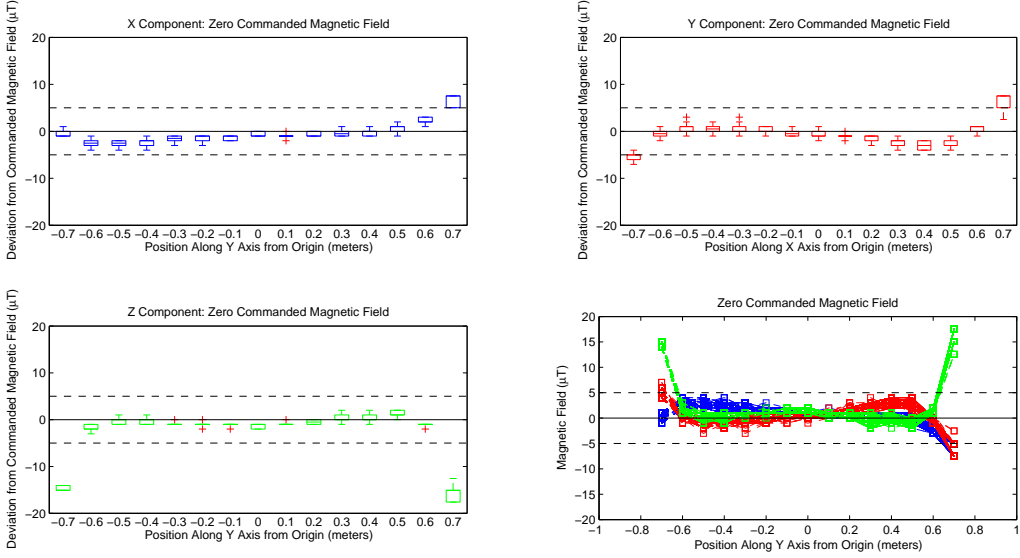


Figure 3-11: Uniformity of Helmholtz Cage Along Y-Axis

The results show that the cage produces a magnetic field with accuracy of  $\pm 5 \mu\text{T}$  within a central area of a square half-meter, which is more than adequate space to fit a CubeSat. While the magnetometer can detect changes as small as  $\pm 0.015 \mu\text{T}$ , the change in the uniformity happens slowly enough from one position to another that the assumption of a constant field in a certain location is valid. This can be seen visually in Figures 3-10 and 3-11 by the size of the boxplots per location - each is about  $1 \mu\text{T}$  wide in its middle quartiles, which represents the 25th to the 75th percentiles. [45]

In addition, there is still a lot of ambient magnetic noise in the laboratory environment that even producing a large field cannot entirely cancel out. However, it turns out that  $\pm 5 \mu\text{T}$  is sufficient for testing the attitude determination and control algorithms for MicroMAS.

# **Chapter 4**

## **Mission Concept of Operations: Requirements and Test Descriptions**

### **4.1 Goals and Requirements of Small Satellite ADCS Testing**

The goal of testing the attitude determination and control subsystem of a satellite is to validate that its estimation and control algorithms operate in conjunction with its actuators as expected, in harmony with the overall software architecture of the entire satellite. This is a non-trivial task, involving the coordination of many pieces of both software and hardware. In the previous sections, the constraints of testing and available facilities were presented. Given these, the objectives and requirements of tests developed for MicroMAS's ADCS will be set forth.

In general, a satellite will have a mission objective and concept of operations (conops) to achieve its objective. Often, this conops includes various modes or states that the satellite will proceed through, where it will accomplish a stepping stone on its way to its overarching mission objective. Each mode is specifically designed to have certain subsystems active and

are defined with entry criteria, exit criteria, and the processes that occur within the mode to take it from entry to exit. Entry and exit criteria are defined with requirements. Evaluating how these requirements can be validated is where test plans begin.

The process for generating test plans is to evaluate the requirements and determine a way to show, with some level of confidence, that they can be met, given the constraints of the testing environment. To use MicroMAS as an example, there are four nominal ADCS modes, each defined with their own entry and exit criteria. The overall conops of its mission dictated the definition of these modes. The science objective of MicroMAS is to hold steady in a local-vertical-local-horizontal attitude while it orbits the Earth, with its spinning payload collecting data. However, the satellite has to maneuver to this desired position, and be able to match the momentum generated by the spinning payload with its internal actuators so that it can hold steady. For MicroMAS, three transition modes were formulated, with one final mode being the mission objective, or science, mode.

## 4.2 ADCS Modes

MicroMAS's four modes are: Detumble, Slew, Spin-up, and Stabilization. When satellites are deployed, they will have some initial spin rate. The objective the Detumble mode is to slow that rotation enough that the satellite can then maneuver itself. The next mode, Slew, is where the satellite will rotate, or slew, from its arbitrary attitude after it detumbles to the desired attitude. The next mode, Spin-up, is when the motor responsible for rotating the payload will kick off. This will introduce a torque into the system that the satellite's actuators will have to account for, in order to hold the bus steady in its desired attitude while the spin-up of the payload occurs. [20] Finally, Stabilization or Science Mode is where the satellite is in the correct attitude to begin to accomplish its mission. This is the desired

mode for the satellite to stay in for the rest of its lifetime. Of course, there are safety modes if off-nominal conditions occur. A block diagram of the modes is shown in Figure 4-1.

Each ADCS mode has requirements it must meet in order to transition to the next

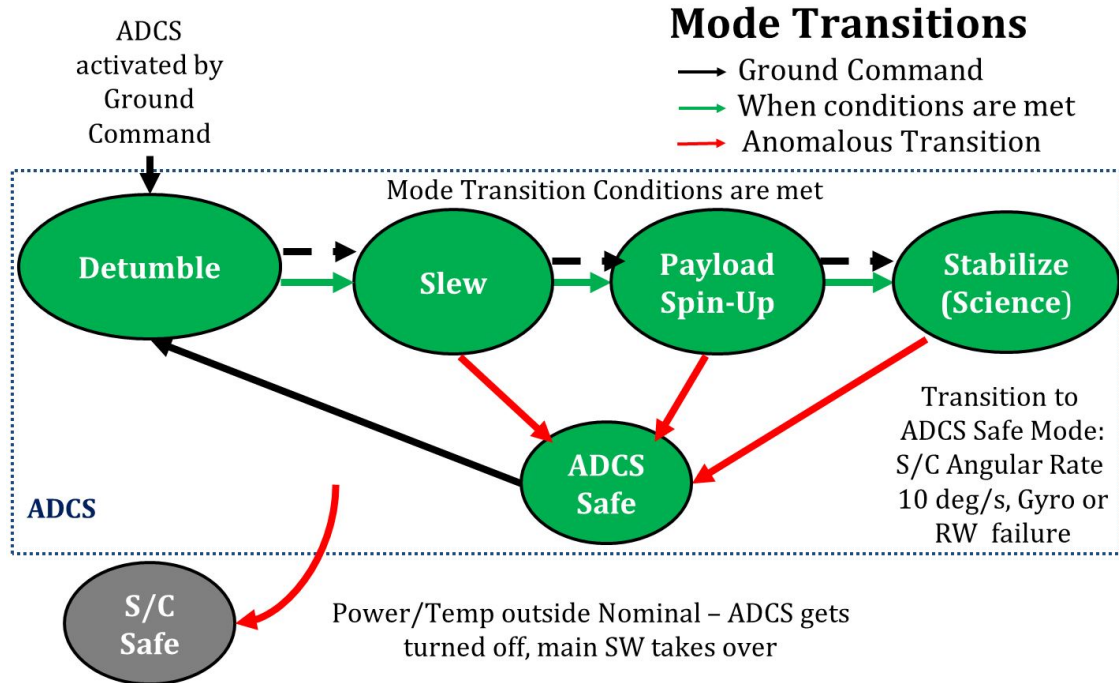


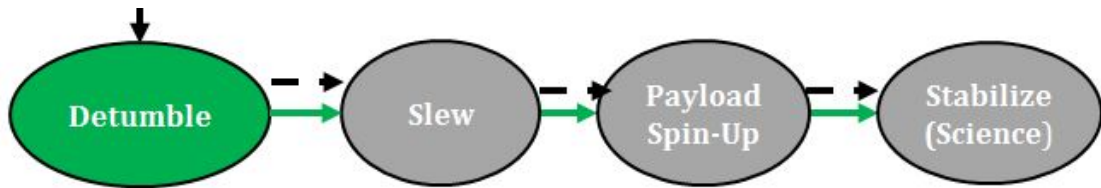
Figure 4-1: MicroMAS ADCS Mode Diagram

mode. These requirements will be discussed in detail in Sections 4.3- 4.6. The transitions between modes can happen either autonomously, when the required conditions have been satisfied, or via a ground command at any time.

## 4.3 Detumble Mode

### 4.3.1 Explanation of Detumble Mode

CubeSats are released into orbit by various deployment schemes. One of these is the poly-picosatellite orbital deployer (P-POD) developed by California Polytechnic State University



[46] and subsequently used by the National Aeronautics and Space Administration (NASA). It can hold multiple nanosatellites, and deploys them via a simple spring-loaded device. [46] Past CubeSat missions have shown that the expected angular rate from the deployment can be up to about 10 degrees per second. The objective of the Detumble mode is to slow the satellite's rate of rotation from its initial tip-off rate out of its deployer to a low enough rate that can be managed by the reaction wheels for maneuvers. Thus, the satellite must be able to damp out this motion, or detumble. The requirement for exiting this mode is that the angular rotation must be less than half a degree per second. This value was selected because it is large enough to be above the noise threshold of the rate gyroscope, but still small enough such that the actuators are able to supply enough torque to manage that residual momentum.

Table 4.1: Detumble Mode Operations Summary

Entry Criteria	Exit Criteria	Operations within Mode
<ul style="list-style-type: none"> <li>➤ Ground Command</li> <li>➤ Recovery from high angular rate</li> </ul>	<ul style="list-style-type: none"> <li>➤ Body frame angular rate <math>\omega &lt; 0.5^\circ/\text{s}^\dagger</math></li> <li>➤ Rate of change of magnetic field <math>\dot{\mathbf{B}} &lt; 1.0T/\text{s}^\dagger</math></li> <li>➤ Meet the above two requirements 100 times in a row</li> </ul>	Operate magnetorquers using B-dot control law to damp out initial angular rate

<sup>†</sup> Indicates parameters that were made adjustable via ground commands. The values listed in the table are the default threshold values, which were selected using a process that included a combination of simulation and test.

Another way to measure angular rate is by looking at the rate of change of the magnetic field. Both rate estimates are used in order to ensure that the satellite has indeed slowed

its rotation rate to the a manageable level. There was also a counter implemented in the flight software, that increments every time the requirement is met for all six cases (three axes each on the gyroscope and the time rate of change of the magnetic field). If any one of these exceeds the threshold, the counter is reset to zero. Once the counter reaches 100, if the software has been set to transition autonomously, the satellite will transition into Slew Mode. Otherwise, a ground operator can watch the counter increment and send the command when it has reached 100.

#### 4.3.2 Testing B-dot Control using the Helmholtz Cage

As presented in Chapter 2, MicroMAS, like many satellites, uses the B-dot control algorithm to damp its rate of rotation using solely torque rods for actuation. The sensors it uses are the magnetometer and the rate gyro. In order to exit Detumble Mode, both the rate of change of the magnetic field, calculated by taking a first-order derivative of the magnetometer measurement, and the satellite's angular rate must be below the required threshold.

In order to test this ability in the lab, the satellite was hung inside the Helmholtz cage and given an initial angular offset about its axis of rotation. It was then allowed to oscillate back and forth until it slowed naturally, due to the damping term provided by the restoring torque from the string. This test was performed with no actuators on, but with all sensors taking measurements. Then, this test was repeated, but with the B-dot control on and a large constant magnetic field generated in the cage. Recall from the B-dot control law presented in Chapter 2 that the torque provided by the torque rods is in fact normal to both the dipole produced by the rod and the magnetic field. Thus, in order for actuation to occur about the axis of rotation, which is perpendicular to the floor, the magnetic field must be parallel to the floor.

The drawing created by the author in Figure 4-2 shows a sketch of the 4-coil per axis

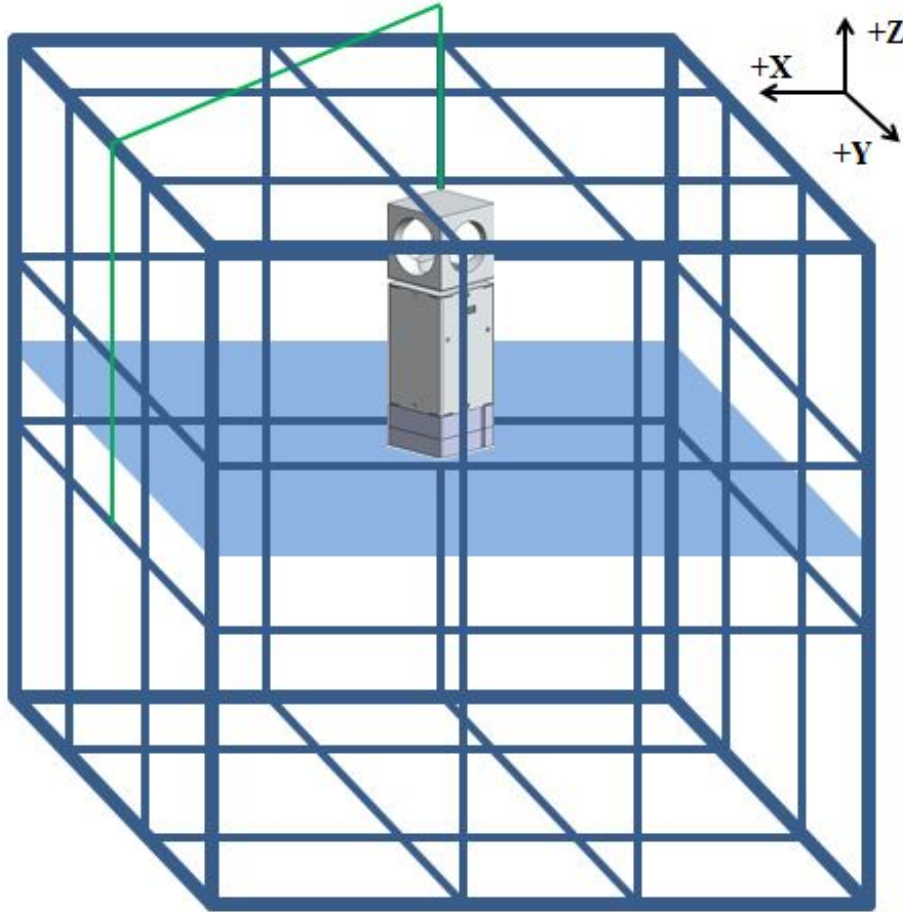


Figure 4-2: Drawing of Desired Magnetic Field within 4-coil per axis Helmholtz Cage for Magnetorquer Actuation with EM Satellite Shown Suspended

Helmholtz Cage, and the light blue parallelogram shows the desired magnetic field in order to allow actuation along the perpendicular axis. The satellite is hung inside the cage with its axis of rotation along the +Z axis in terms of cage coordinates (as shown in Figure 4-2). Thus, the magnetic field that the magnetorquers can actuate against must be in the X-Y plane, as shown.

The reason that the field generated within the cage is constant, rather than following the expected IGRF model, is from an assumption mentioned back in Chapter 2 about how the B-dot algorithm functions. It can be assumed that over short time periods on-orbit, that the magnetic field is static. Motion that the satellite experiences due to translation

along its orbit would not see a noticeable change in field over the control sample time (4 Hz). Any change in field that is greater than about 5% of the total magnitude of the field can be attributed to tumbling. Therefore, for the purposes of testing, the field generated in the cage was constant. This allows the rate of change of the magnetic field to essentially be used as a measure of angular rotation, and can be used in conjunction with the rate gyros to verify that the satellite has stopped tumbling.

### 4.3.3 Evaluating Performance of the B-dot Control

In evaluating the success of the tests, the control engineer should compare the response of the system in the two cases outlined above, namely the non-actuating case and the actuating case. The difference in the measured torque between the two cases should be equal to the torque applied by the magnetorquers. The system will be evaluated by measuring the angular position and velocity as a function of time. Sections 4.3.3.1- 4.3.3.3 describe the evaluation of this performance with a prediction based on a model of the relevant dynamics.

#### 4.3.3.1 Modeling the System as a Harmonic Oscillator

The torque on a system modeled as a harmonic oscillator can be equated to a restoring torque that is proportional via  $k_d$  to the displacement  $\theta$ . Since this oscillator is not in a perfectly friction-free environment, there is some damping effect due to the resistance of the air, captured by a term  $c_d$  that is proportional to the angular rate. These terms are all scalar since the system is limited to one axis in freedom of rotation, and the torque, angular displacement, angular rate, and inertia are all about this axis.

$$\tau = -k_d J\theta - c_d J\dot{\theta} \quad (4.1)$$

In this case,  $J$  is a scalar term that represents the moment of inertia about the axis of rotation. It is possible to solve for the terms  $k_d$  and  $c_d$  with measurements of the system, which will be described below.

#### 4.3.3.2 Solving for Parameters of the System

In an underdamped system, the time response can be modeled by a decaying exponential function. This function contains parameters that help define properties of the system, including its damping coefficient  $\zeta$ , undamped natural frequency  $\omega_n$ , and damped frequency of oscillation  $\omega_d$ .

$$f(t) = Ae^{-\zeta\omega_n t} \cos(\omega_d t + \phi) \quad (4.2)$$

The damped frequency of oscillation can be computed from simply taking the reciprocal of the measured period of the oscillation multiplied by  $2\pi$ . If the system is fitted to a general form exponential decay function, the following relationships can be exploited to solve for the damping coefficient of the system:

$$f(t) = ae^{-bt} \quad (4.3)$$

$$a = A \cos(\omega_d t + \phi) \quad (4.4)$$

$$b = \zeta\omega_n \quad (4.5)$$

$$\omega_d = \omega_n \sqrt{1 - \zeta^2} \quad (4.6)$$

Equations 4.5 and 4.6 can be solved as a system of equations to yield the damping coefficient  $\zeta$  and the natural frequency of the system  $\omega_n$ . Finally, the proportional terms  $k_d$  and  $c_d$  from equation 4.1 can be solved for via the following relationships:

$$k_d = \omega_n^2 \quad (4.7)$$

$$c_d = 2\zeta\omega_n \quad (4.8)$$

The damping ratio  $\zeta$  will be different for the two cases, but the natural frequency  $\omega_n$  of the system should remain constant. The difference in the damping coefficients will be related to the amount of torque produced by the magnetorquers in the second case.

#### 4.3.3.3 Comparing the Two Cases

Once the torque on the system has been found for both the non-actuating and actuating cases, they can be compared. The non-actuating case should only have torque due to the restoring torque provided by the string and damping due to the air. The actuating case should have a damping effect provided by the magnetometers in addition to those same terms. Since the B-dot control law is simply related to rate, it essentially just adds another  $c_d$  term to the equation. The dipole  $\mathbf{m}$  consists of the product of a scalar gain with the three-dimensional vector representing the rate of change of the magnetic field  $\dot{\mathbf{B}}$ .

$$\mathbf{m} = k\dot{\mathbf{B}} \quad (4.9)$$

The rate of change of the magnetic field, assuming a constant ambient field – which is accurate over short time periods in a non-rotating attitude on orbit – is simply the cross product of the angular rate with the magnetic field.

$$\dot{\mathbf{B}} = \boldsymbol{\omega} \times \mathbf{B} \quad (4.10)$$

In this particular test set-up, the field was generated such that it is always perpendicular to the rotation, so that equation 4.10 becomes simply the product of magnitudes of the magnetic field  $\mathbf{B}$  and the measured angular rotation rate in the body frame  $\boldsymbol{\omega}$ . Since we

assume that the magnetic field is constant for small time periods, the product of the gain  $k$  with the magnetic field  $\mathbf{B}$  is a constant.

$$\mathbf{m} = k |\mathbf{B}| \boldsymbol{\omega} \quad (4.11)$$

Recall that the torque produced by the dipole is the cross product of the dipole with the magnetic field. Knowing that the magnetic field is always perpendicular to the dipole, due to equation 4.10, the torque produced by the dipole  $\mathbf{m}$  is simply a function of angular rate, which is the time derivative of angular position. This relationship makes sense since the objective of the B-dot algorithm is to damp out the tumbling rate of the satellite.

$$\tau_m = k J |\mathbf{B}|^2 \dot{\theta} \quad (4.12)$$

It is important to bear in mind the physical limitation of  $\mathbf{m}$  able to be produced by the magnetorquers:  $\pm 0.108$  Ampere-square-meters ( $\text{Am}^2$ ). Taking this relationship and substituting it back into equation 4.1, it can be seen that the combination of  $k |\mathbf{B}|^2$  essentially becomes an extra damping term.

$$\tau_A = -k_d J \theta - (c_d J - k |\mathbf{B}|^2) \dot{\theta} \quad (4.13)$$

Compare equation 4.1 for the natural response with no actuators to equation 4.13 for the response with B-dot running. The torque in the actuating case (termed “case 1” and modeled by equation 4.13) differs from the torque in the non-actuating case (termed “case 2” and modeled by equation 4.1) by the product of the scalar gain of the B-dot algorithm multiplied by the square of the magnitude of the ambient magnetic field. This difference is illustrated by the different damping terms  $c_1$  and  $c_2$  in equation 4.14.

$$c_2 J = c_1 J + k |\mathbf{B}|^2 \quad (4.14)$$

The inertia  $J$  about the satellite's axis of rotation remains unchanged, as does the scalar gain  $k$  and magnitude of the magnetic field from equation 4.11. Knowing this, the damping coefficient of the actuating case (2) can be analytically predicted, knowing the results of the non-actuating case (1) and the strength and orientation of the magnetic field. Using equation 4.8 to substitute in for  $c_d$  yields:

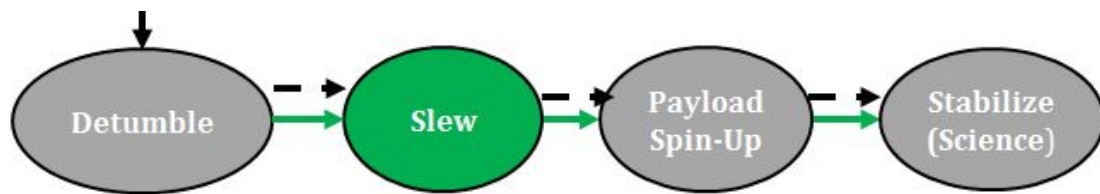
$$2\zeta_2\omega_n J = 2\zeta_1\omega_n J + k |\mathbf{B}|^2 \quad (4.15)$$

Now, solving for the damping coefficient of the actuating case (2), gives:

$$\zeta_2 = \frac{2\zeta_1\omega_n J + k |\mathbf{B}|^2}{2\omega_n J} \quad (4.16)$$

Thus, the measured damping coefficient of the actuating case can be compared with the predicted value from equation 4.16.

## 4.4 Slew Mode



### 4.4.1 Explanation of Slew Mode

The objective of Slew Mode is to rotate the satellite from whatever arbitrary non-rotating attitude it ends up in after Detumble Mode to the desired mission attitude. Because MicroMAS is taking measurements of the Earth's atmosphere, its mission is to point down at

the Earth, in an attitude called local-vertical local-horizontal (LVLH). In the body frame of reference, the x-axis is along the velocity of the satellite, the y-axis is in the in-track direction, and the z-axis is pointing up, away from Earth.

In order to rotate the satellite in a precision motion, the control law presented in Chapter

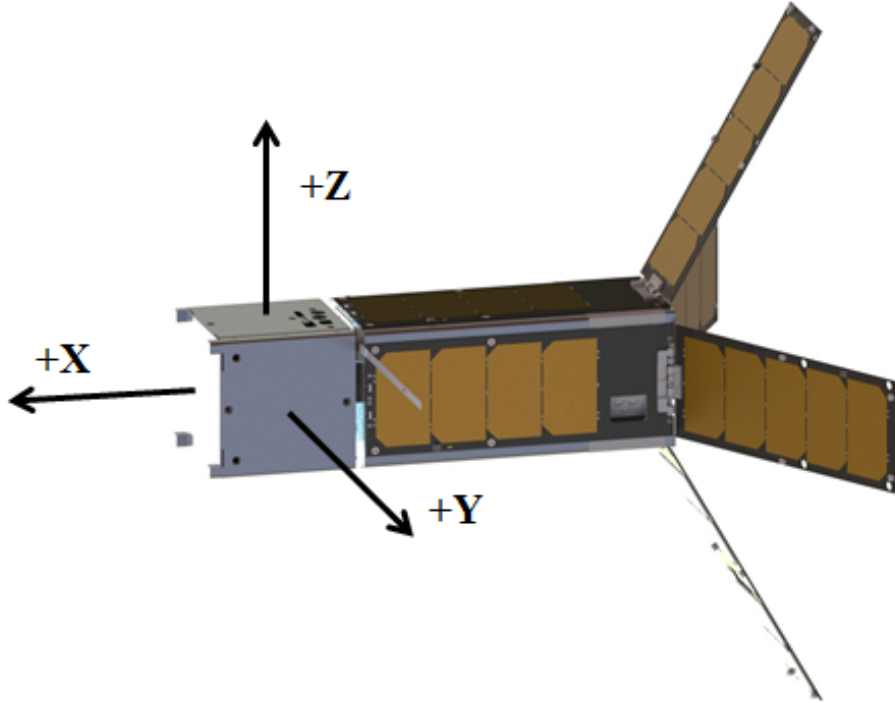


Figure 4-3: MicroMAS in its nominal LVLH attitude[17]

2 is implemented. Recall that the control law for MicroMAS was based on a Linear Quaternion Feedback Regulator, which means it uses its measured attitude and rate information to navigate to the desired attitude. Within Slew Mode, the satellite employs its reaction wheel set to apply the control torque, causing the bus of the satellite to rotate. The magnetorquers are also used throughout Slew Mode in order to help dump excess momentum that may be introduced to the system by disturbances.

The criteria to transition from Slew Mode to Spin-up Mode require that the satellite be in its LVLH attitude within a certain threshold, and that its angular rate is also less than a certain threshold. Also, because the satellite's next ADCS mode involves being able to

match the angular momentum produced by the motor and the spinning payload, there is a requirement on the speed of the reaction wheel aligned on the axis of rotation with the payload. Because of conservation of angular momentum, the momentum produced by the rotation of the payload will cause a rotation of the bus, unless it is countered by the reaction wheels. To prevent the rotation of the bus, and thus the loss of the desired pointing location, the conops of MicroMAS requires the reaction wheels to match the momentum of the spinning payload. The unit vector  $\hat{\mathbf{n}}$  represents the alignment of the momentum due to the payload, and therefore the required matching momentum by the reaction wheels.

$$(J_P \omega_P) \hat{\mathbf{n}} = (J_{RW} \omega_{RW}) \hat{\mathbf{n}} \quad (4.17)$$

The angular velocity of the reaction wheel at the end of the spin-up is proportional to the final desired angular velocity of the payload. Since the payload's speed is determined by the mission, the final reaction wheel speed can be calculated. Thus, the requirement is such that at the end of Slew Mode, the reaction wheel speed aligned along the spin axis of the payload must be  $\omega_{RW}$  less than the final reaction wheel speed desired. This final desired reaction wheel speed can be selected such that it is still able to provide some amount of torque.

It was determined that the allowable amount of torque actuation to damp out disturbances for this mission after payload spin up is 0.1 milliNewton-meters (mN-m), or about 20% of the full capacity of the reaction wheels at low speeds. According to simulations, this amount of torque would still be able to handle expected disturbance torques. [20] This decision imposed a constraint on the reaction wheel at its final speed being at approximately 8000 revolutions per minute (RPM). Thus, the total momentum caused by the payload spinning could not exceed the momentum of the reaction wheel spinning at 8000 RPM. The constraint is then that the reaction wheel speed must be less than the starting value. Because the payload spins in a positive direction with respect to the body frame, the reaction

wheel must spin in a negative direction to counter it. Thus, the constraint actually becomes that the reaction wheel must begin at a speed greater than 0 RPM, so that it can spin the 8000 RPM required to counter the spin-up torque, and still remain at -8000 RPM where it can still provide 0.1 mN-m of torque.

In addition to these two criteria (see Table 4.2), there is a third that has to do with attitude estimation. Recall from Chapter 2 that the Earth horizon sensors are used for finer pointing knowledge. In order to know the attitude of the satellite with greater precision and thus aid in the analysis of the science data collected, another requirement on the transition from Slew to Spin-up is that the Earth horizon sensors have valid information and are being used for attitude estimation.

Table 4.2: Slew Mode Operations Summary

Entry Criteria	Exit Criteria	Operations within Mode
<ul style="list-style-type: none"> <li>➤ Body frame angular rate <math>\omega &lt; 0.5^\circ/\text{s}^\dagger</math></li> <li>➤ Rate of change of magnetic field <math>\dot{\mathbf{B}} &lt; 1.0 \text{T/s}^\dagger</math></li> <li>➤ Meet the above two requirements 100 times in a row</li> </ul>	<ul style="list-style-type: none"> <li>➤ Attitude within <math>\pm 1</math> degree<sup>†</sup> of commanded attitude</li> <li>➤ Body frame angular rate <math>\omega &lt; 0.5^\circ/\text{s}^\dagger</math></li> <li>➤ Reaction wheel aligned with spin axis of payload <math>\omega_{RW}\hat{\mathbf{n}} &gt; 0 \text{ RPM}^\dagger</math></li> <li>➤ Earth horizon sensors valid (Y/N)<sup>†</sup></li> <li>➤ All three of these criteria are met 50 times, with less than 2 seconds between occurrences</li> </ul>	Using reaction wheels, rotate satellite to LVLH and hold steady at that attitude

<sup>†</sup> Indicates parameters that were made adjustable via ground commands. The values listed in the table are the default threshold values, which were selected using a process that included a combination of simulation and test.

Slew Mode, like Detumble Mode, also uses a counter to increment when the criteria have been successfully met. Again, all criteria listed must be met within the same command cycle

in order for the counter to increment. Unlike in Detumble however, the counter is slightly more noise-resistant. As long as it has been less than 2 seconds since all of the conditions were met, the counter will continue to increment. If it has been longer than 2 seconds, then the counter resets to zero. This slightly different approach allows for the counter to be robust to noise in the measurements. Again, as in Detumble Mode, if the satellite is set in its autonomous mode, once it reaches a count of 50 times of satisfying the exit criteria, it will transition autonomously. Otherwise, a ground operator can watch the counter and send a command.

#### **4.4.2 Testing Slew Mode using the Piñata Rig and the Helmholtz Cage**

Slew Mode is tested in a similar manner to Detumble Mode - with the satellite suspended on a string within the Helmholtz Cage. However, the evaluation of success comes from a model of the system, with the string parameters accounted for, as compared to the response of the system. The simulation models the attitude, angular rate, control torque, and reaction wheel speed - since each of these are measured values, they will be compared to see how well the system responded when compared to the prediction. Like Detumble, the satellite still only has one axis of limited freedom of rotation, and thus each set of tests must be run for all three orientations (each body axis aligned with the axis of rotation).

##### **4.4.2.1 Modifications to the Code Needed for Laboratory Testing**

The attitude estimation for the on-orbit conops requires either sun sensors or Earth horizon sensors to have valid information. This is a reasonable assumption for on-orbit operations, but is much more difficult to reproduce in a laboratory environment. Because the sun sensors

are mounted on solar panels, and because CubeSat programs are constrained by cost and schedule, the engineering model (EM) of the satellite did not have its own set of solar panels with sun sensors. Thus, the sun sensor algorithm could not be tested as part of the attitude determination and control tests. (It was tested on the fully-integrated satellite.)

Likewise, the engineering unit of the reaction wheel set did not have Earth horizon sensors. For a time, the flight reaction wheel set was tested on the EM satellite. However, the algorithm for detecting the Earth's limb relies on the specific geometry of the Earth with respect to the satellite on-orbit, and would have been rather difficult to simulate. Hot plates were used as initial calibrators for the sensors, to assess what temperature differential corresponded to the voltage differential. For a reliable test of the Earth horizon sensors, a more precise hot plate set up would have been required and is left as future work for CubeSat ADCS testing. On this particular program, the flight reaction wheel unit was needed for other tests with the fully integrated flight satellite, and the engineering unit did not have the Earth horizon sensors needed.

Thus, with these limitations, the only sensors for attitude control remaining are the magnetometer and the inertial measurement unit. The rate gyros are already used as rate measurements, and in order for the Extended Kalman Filter to work properly, could not be part of the attitude estimate. However, the linear accelerometers could be used for attitude estimation in the lab. This is because the gravity vector always points down, and can be used as a reference vector for estimation. Thus, for lab testing, the accelerometer is used in conjunction with the magnetometer as the two sensor inputs to the TRIAD algorithm.

In the laboratory environment, a quaternion can be generated for attitude knowledge, and the rate gyros are used for angular rate measurements, as in flight. The Extended Kalman Filter would function exactly as it would for on-orbit ops. There is only one other minor difference that must be implemented for ground tests, having to do with coordinate frame transformations. The desired attitude is calculated in the inertial frame from the orbit

propagator's estimate of position and velocity, and then rotated into the body frame via the rotation matrix calculated from the TRIAD algorithm. However, in the lab, the inertial frame can be set to any orthogonal coordinate frame, rather than the position and velocity provided by the orbit propagator. For simplicity, the rotation matrix was overwritten to be the identity matrix, which means that the inertial frame has the same coordinate frame as the satellite's body frame. This adjustment makes testing of the control law more intuitive, without losing any of the control terms.

#### 4.4.2.2 Further Ground Commands

Because Slew Mode requires validating that the satellite can slew to the commanded attitude, a test requires it to start at some attitude and rotate to the commanded attitude. However, unlike Detumble Mode, in Slew Mode, the satellite should start at an initial non-rotating attitude, with no external torque. The way we tested this slewing capability was to overwrite the reference vectors that determine the measured body-to-inertial quaternion. The reference vectors would be changed such that their new reference for a non-rotated attitude would be some angular offset  $\theta$  from the satellite's neutral position, along the axis of rotation. This would cause the attitude error to be non-zero and thus cause it to rotate  $\theta$  radians to its commanded attitude.

The calculation of the angular offset is just a multiplication by the magnetometer measurement by a rotation matrix.

$$\mathbf{v}_R = \mathbf{R}(\theta)\mathbf{v}_M \quad (4.18)$$

The  $R$  subscript represents the rotated vector, and the  $M$  subscript indicates the initial measured vector. The rotation matrix rotates the vector about the axis of rotation. The

possible choices are as follows, for  $x$ ,  $y$ , and  $z$  respectively:

$$\mathbf{R}_x(\theta) = \begin{bmatrix} 1 & 0 & 0 \\ 0 & \cos \theta & -\sin \theta \\ 0 & \sin \theta & \cos \theta \end{bmatrix} \quad \mathbf{R}_y(\theta) = \begin{bmatrix} \cos \theta & 0 & \sin \theta \\ 0 & 1 & 0 \\ -\sin \theta & 0 & \cos \theta \end{bmatrix} \quad \mathbf{R}_z(\theta) = \begin{bmatrix} \cos \theta & -\sin \theta & 0 \\ \sin \theta & \cos \theta & 0 \\ 0 & 0 & 1 \end{bmatrix} \quad (4.19)$$

This process of manipulating the attitude measurement for testing Slew Mode is performed in the following steps:

1. Hang satellite on string in cage and stabilize. Wait until its angular rate is below  $0.5^\circ/\text{s}$  and its measurement of the magnetic field has stabilized.
2. If it is not already, send a command to change the reference vector for the accelerometer to be equal to its present measurement.
3. Multiply the magnetometer measurement by a rotation matrix. This rotation matrix will vary depending on which axis is the axis of rotation. (See equations 4.18 and 4.19.) The angle  $\theta$  can be determined by the test arbiter. However, slews larger than about  $45^\circ$  may not be possible, depending on the restoring torque provided by the string. Smaller angles are preferable. We used a maximum of  $30^\circ$ .
4. Set the vector result of this rotation multiplication  $\mathbf{v}_R$  as the reference vector for the magnetometer. The control law should immediately recognize it now has non-zero attitude error and should slew in the appropriate direction along the axis of rotation  $\theta$  radians.

It should be noted that the satellite cannot hold this attitude indefinitely. This is due to the restoring torque outlined in Section 4.3.3.1. Because this torque is proportional to the angular offset  $\theta_d$  from the neutral, unrotated position, the restoring torque will be some constant non-zero value. Therefore, unlike operations on orbit, the reaction wheels will have

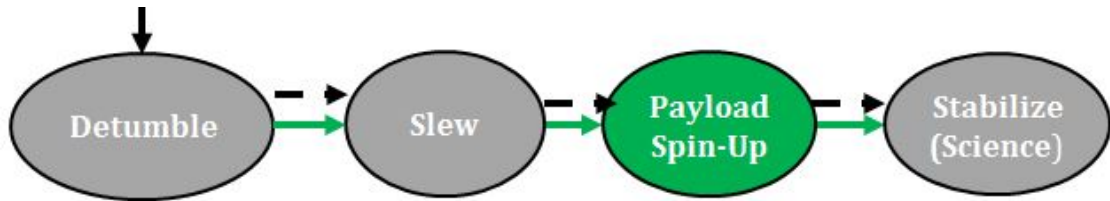
to continue to provide torque to remain at their commanded attitude because they will be fighting that restoring torque. Eventually, the reaction wheels will saturate and be unable to provide any more torque. At this point, the satellite will act like the non-actuating damped harmonic oscillator from the Detumble section, and will begin to freely rotate. However, this is not the motion that is important for validation of Slew Mode. The part of the motion that matters is the rotation to the desired attitude, which only takes a few seconds.

In terms of satisfying the exit criteria to transition from Slew Mode to Spin-Up Mode, most of the criteria are the same. The only difference in the transition requirements is the check on having information from the Earth horizon sensors, since that is not possible in the laboratory. However, having attitude error and angular rate error below thresholds are still constraints, as well as ensuring the reaction wheel speed is above 0 RPM. Thus, these conditions are still evaluated as completely as possible in the laboratory environment.

#### **4.4.3 Evaluation of Slew Mode**

The evaluation of Slew Mode that can be performed by this test is ensuring that the rotation takes place about the correct axis and in the correct direction, and results in the satellite holding that attitude to within the requirements. However, because this test is only partially representative of freedom of rotation, and holding any attitude offset from the neutral position requires a constant torque from the reaction wheels, the requirements for holding the attitude can be relaxed slightly. The evaluation of the slew itself will be quantitative comparisons of the attitude, angular rate, control torque, and reaction wheel speed with respect to the model which accounts for the string dynamics.

## 4.5 Spin-up Mode



### 4.5.1 Explanation of Spin-up Mode

The conops of MicroMAS requires the satellite to be holding its commanded attitude when it begins its spin-up profile. This allows for the actuators to account for disturbances and the spin up of the payload. The control law operating in Spin-up Mode is the same as for Slew Mode, as described in Chapter 2. The reaction wheel aligned with the spin axis of the payload spins up such that its angular momentum exactly matches that of the rotating payload. The entry criteria for Spin-Up Mode are the exit criteria for Slew Mode.

<sup>†</sup> Indicates parameters that were made adjustable via ground commands. The values listed in the table are the default threshold values, which were selected using a process that included a combination of simulation and test. The entry criteria for Spin-up Mode are fourfold: constraints on attitude, angular rate, reaction wheel speed, and sensor knowledge. The process for generating the attitude with the magnetometer and accelerometer yields an attitude estimate such that the first requirement can be met. The second requirement is met by starting the satellite in its neutral, non-rotating attitude so that it starts off with a close-to-zero initial rate (there is always some noise on the measurement). The third requirement, pertaining to the speed of the reaction wheel aligned with the spin axis, is sometimes more difficult to meet.

The reaction wheel aligned with the spin axis of the payload is required to be greater than 0 RPM, in order to be able to provide enough torque to counter the torque caused by the acceleration of the payload. On orbit, the satellite may arrive in a situation where it

Table 4.3: Spin-up Mode Operations Summary

Entry Criteria	Exit Criteria	Operations within Mode
<ul style="list-style-type: none"> <li>➤ Attitude within <math>\pm 1</math> degree<sup>†</sup> of commanded attitude</li> <li>➤ Body frame angular rate <math>\omega &lt; 0.5^\circ/\text{s}^\dagger</math></li> <li>➤ Reaction wheel aligned with spin axis of payload <math>\omega_{RW}\hat{\mathbf{n}} &gt; 0 \text{ RPM}^\ddagger</math></li> <li>➤ Earth horizon sensors valid (Y/N)<sup>†</sup></li> <li>➤ All three of these criteria are met 50 times, with less than 2 seconds between occurrences</li> </ul>	Autonomous: Payload has reached its final commanded angular velocity	Hold steady at commanded attitude to within $1^\circ$ and angular rotation less than $0.5^\circ/\text{s}$ while payload spins up to its commanded rate

has completed its slew maneuver and be in the commanded attitude, but its reaction wheels may not be back at zero RPM due to disturbances introduced into the system. These disturbances are not predictable, and the only solution is to wait and allow the control law to damp them out, and to allow the magnetorquers to use the magnetic field to provide torque to help unload the reaction wheels.

The final requirement to enter Spin-up Mode is having valid information from the Earth horizon sensors and using them in the attitude estimation process. In the lab, that is not really possible for reasons stated above. Thus, this part of the requirements was ignored for ground testing.

## 4.5.2 Testing Spin-up Mode using the Piñata Rig and the Helmholtz Cage

The test for Spin-up is very similar to the test for Slew Mode. In order to have feedback attitude information, the attitude information is modified in the same manner described in Section 4.4.2.1. The difference is that a slew is not necessary, so a rotation matrix is not needed for the second reference vector, as described in equation 4.18. Rather, the measurements of the accelerometer and magnetometer at the satellite’s unrotated, neutral hanging position can both be set as the reference vectors for the TRIAD algorithm. This will mean that the satellite “thinks” that it is at its commanded attitude, which is the desired result.

At this point, the satellite is then commanded by the ground station operator to enter slew mode. The motor that spins the payload will go through an initialization process that includes commutation. There is a wait period between this process and the actual spin up, since that commutation introduces a random, unpredictable disturbance. The feedback terms in the control law are able to handle it as a disturbance. The motor controller is then given a commanded acceleration and final target speed, and will start to accelerate until it reaches that target speed. The control law will apply torque in the opposite direction, since the  $\alpha_P$  term will be non-zero during this time. The objective of this test is to ensure that the torque caused by the spinning payload is properly matched by the combination of the control law with the reaction wheels.

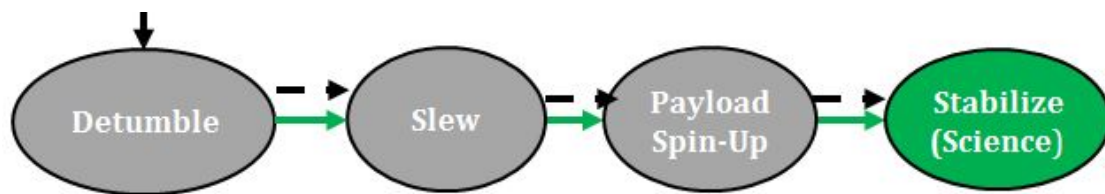
## 4.5.3 Evaluating the Spin-up

The evaluation of the success of this mode is rather simple. The attitude and rate estimates during the acceleration of the payload should stay within the requirements. If there is a rotation, the acceleration of either the payload or the reaction wheels must be adjusted such

that the payload reaches its final speed without perturbing the satellite. Since torque is simply the product of inertia and acceleration, theoretically any final speed could be reached by the spinning payload, as long as its acceleration was arbitrarily low.

However, there is a limitation imposed by the reaction wheels, as mentioned above. They can only provide torque up to a certain wheel speed, and then are no longer able to rotate any faster. Due to the constraints on the torque available in CubeSat-sized hardware, this torque is quite small (less than 1 milliNewton-meter). Thus, the acceleration of the payload is quite low. If the satellite is found to rotate, the accelerations of the reaction wheel and the payload can be adjusted in an iterative fashion to provide equal torques within the system capabilities.

## 4.6 Stabilization (Science) Mode



### 4.6.1 Explanation of Stabilization Mode

Stabilization Mode is the last nominal ADCS mode, and its objective is simply to hold the satellite in LVLH so that the payload can run and collect data. This mode uses the same controller as the previous two modes. The difference is simply in the conops, where the satellite is already in the correct attitude and the payload is spinning. It must simply remain there and fight any disturbances to hold its attitude.

Table 4.4: Stabilization Mode Operations Summary

Entry Criteria	Exit Criteria	Operations within Mode
➤ Angular velocity of the payload $\omega_P$ has reached its final commanded value	None	Hold steady at commanded attitude to within $1^\circ$ and angular rotation less than $0.5^\circ/\text{s}$ while payload spins at its commanded rate

#### 4.6.2 Testing of Stabilization Mode

The test of Stabilization mode is tacked onto the testing of Spin-up mode. The conops to be validated is that the satellite can maintain its attitude after spin-up is complete, and withstand disturbances. The test consists going through Slew Mode, transitioning to Spin-up Mode, and continuing to run the controller after payload spin-up is complete, to ensure that the satellite continues to internally provide the angular momentum with the reaction wheels such that the bus does not rotate. Again, there are limitations in only being able to test this in one axis at a time, but the most visible results in a mismatch of torques are along the spin axis of the payload.

#### 4.6.3 Evaluating Stabilization

The evaluation for Stabilization is the same for Slew: ensuring that the attitude and rates stay within the required bounds, and match the model of the test set-up. The difference for Stabilization Mode is determining the length of the test required to validate the robustness and endurance of the controller. Unfortunately, that time is limited because restoring torque of the string will eventually saturate the reaction wheels. But before that occurs, the errors in attitude and angular rate can be evaluated to make sure that they stay within requirements to within three sigma.

# Chapter 5

## Test Results

### 5.1 Overview

This chapter will go over the results of testing the hardware, the estimator, and the controller in various modes as described in the previous chapter. One challenge to bear in mind while evaluating test results is the limitations in testing algorithms designed for estimation and control in space in a laboratory. These limitations were presented in Chapter 3, and metrics for evaluating the tests were presented in Chapter 4. Despite these limitations, a lot can be shown by testing a system, and there are many lessons to learn in taking the leap from a simulation to implementing a system on real hardware and evaluating its performance.

First, the results of verifying the performance of the hardware will be presented. Next, some results of the Kalman filter will be discussed, in order to show that the filter is, in fact, giving the optimal estimate of the state. The remaining sections are devoted to presenting the results of tests of the controller for the four ADCS modes presented in Chapter 4. These tests are evaluated with respect to a model that was designed specifically to take into account the constraints of the test environment. Further discussion of results are in Chapter 6.

## 5.2 Verification of Actuator Performance

### 5.2.1 Magnetorquers

The actuators used in the Detumble Mode are three orthogonally mounted magnetorquers. Electric current flows through these metal rods, which produces a magnetic dipole moment, in units of current multiplied by area. When this dipole interacts with the ambient magnetic field, it produces a torque that is perpendicular to both the induced current and the ambient magnetic field.

Before testing that the algorithm would work in conjunction with the hardware, it is important to validate that both work individually. The B-dot algorithm is well-known, and has been shown to work in simulation. However, for every satellite, each piece of hardware is unique and must be tested. The magnetorquers for MicroMAS came as a unit with a reaction wheel set made by Maryland Aerospace Incorporated.

The magnetorquers are commanded via discretized dipole commands, with the raw values varying between -127 and 127, with a maximum dipole command of 0.15 Ampere-square-meters ( $\text{Am}^2$ ). Rather than producing various amounts of current to produce varying dipoles, the current is duty cycled. The control sample period is 250 milliseconds. Because the satellite also has a magnetometer intended to measure the ambient field, this duty cycle is timed such that current is never applied when the magnetometer is sampled. The maximum duty cycle is 180/250 milliseconds, or a 72% duty cycle, which results in a maximum resultant dipole of  $0.72 \times 0.15 = 0.108 \text{ Am}^2$  and a resolution of 0.00085  $\text{Am}^2$ .

In order to test the functionality of the magnetorquers, an additional magnetometer was required, which would be able to sample during the time that the current would be applied. A Fluxgate APS magnetometer, the same as was described for the calibration of the Helmholtz Cage in Section 3.3.2.3, was used. It was placed on top of the ADACS unit containing the torque rods, with its orientation such that the axes of the magnetometer were aligned to

match the axes of the ADCAS unit. An example with the test of the y-axis magnetorquer is shown in Figure 5-1.

The dotted lines in Figure 5-1 are the ambient magnetic field when the torque rods are

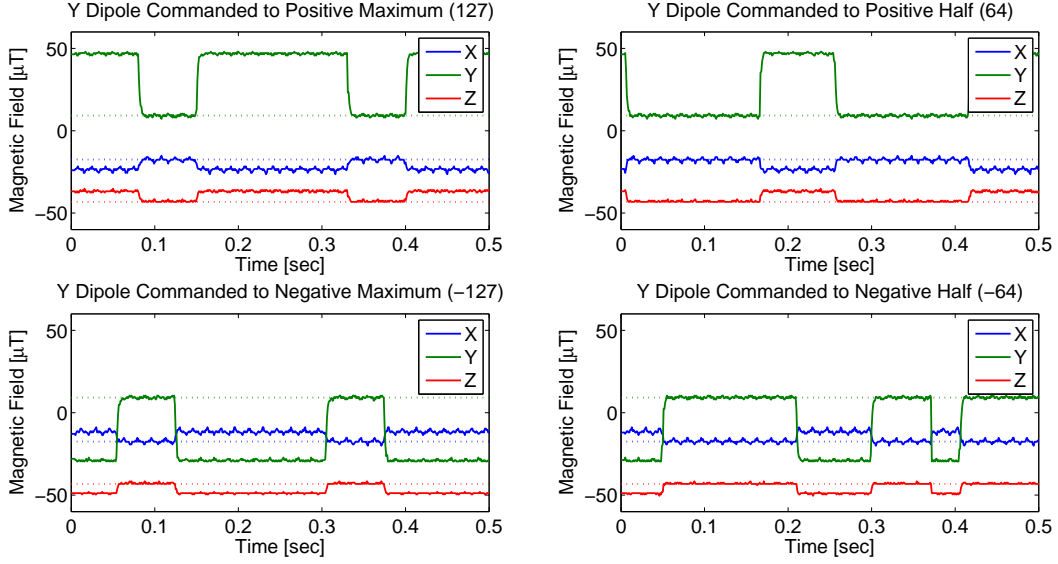


Figure 5-1: Y-Axis Magnetorquer Duty Cycling

not firing. The duty cycle is 72% when maximum and 36% when at half. This is exactly what is expected since the full duty cycle allows the magnetorquers to be on for 180 milliseconds out of the full 250 millisecond control cycle, and  $180/250 = 0.72$  and  $90/250 = 0.36$ . Likewise, for the negative commands, the duty cycles are the same, and one can see the magnetic flux is negative.

This test simply checks for functionality – that the torque rods do in fact turn on for the duty cycle expected given the command. There is some coupling between axes observable: one can see that the X and Z axes of the magnetic field also respond for Y dipole commands. This could be due to a slight misalignment between the magnetometer and the placement of the torque rods within the ADACS unit. There is some uncertainty in the exact location of the measuring device inside the magnetometer, as well as the exact location of the rods inside the unit. However, despite these uncertainties, these measured changes in magnetic

field roughly correspond to a first-order approximation of the flux that should be measurable at the approximated distance.

### 5.2.2 Reaction Wheels

The main actuators for controlling the attitude of the satellite are the three orthogonally-mounted miniature reaction wheels. Like any piece of the system, the wheels needed to be tested independently of the controller to verify performance specifications. The vendor gave specifications on maximum wheel speed and torque capacity, as well as a value for the inertia of the wheels. From these values, the speed and torque capability of the wheels could be evaluated.

A simple test was run on the flight ADACS unit for all three wheels to evaluate the maximum speed and torque they could produce. Each wheel was commanded to the maximum torque command and allowed to run until it reached its maximum speed. The measured torque was calculated by taking a first-order time derivative of the tachometer-measured wheel speed and multiplying it by the inertia value given by the vendor. The results of this analysis are shown in Figure 5-2.

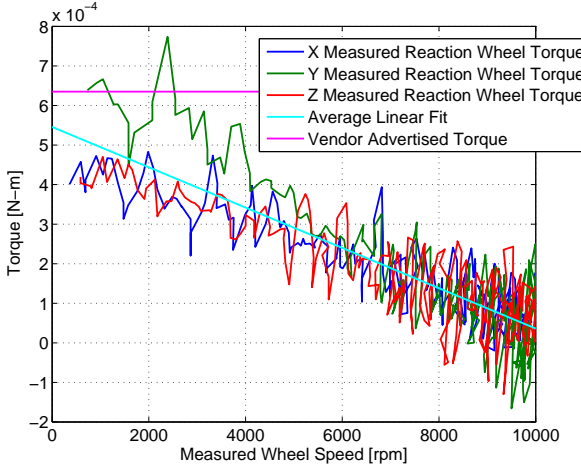


Figure 5-2: Measured Reaction Wheel Torque with a Linear Fit

The maximum torque estimated for the flight ADACS unit by the vendor was 0.635 mN-m [33], but it is to be expected that the wheel performance would degrade somewhat with wheel speed. This degradation is due to the electromotive force from the motors driving the wheels – commonly called back EMF – according to Lenz’s law. The spinning motor produces a flux which produces a torque which opposes its angular velocity. As more current is applied to the motor to continue its acceleration, the torque that the motor is able to supply decreases with a fixed voltage input. [47] This reduction in torque was modeled with a simple first-order linear best fit.

This fit was then used to estimate the ability of the reaction wheels to provide torque at any given time, knowing the speeds of the wheels. Based on other tests with lower torque commands, the results showed that as long as the commanded torque to the wheels was at or below the estimated value from the linear fit, the wheels were successfully able to produce that torque. This torque limitation important to bear in mind when evaluating the performance of the controller with the reaction wheels.

On-orbit, the magnetorquers should help to continuously desaturate the reaction wheels. However, in the laboratory environment, even with a strong magnetic field, the disturbances

are still too large for the magnetorquers to be able to overcome to keep the reaction wheels from saturation. *Pong* did an analysis of the power spectral distribution of the disturbances in a laboratory environment using an air bearing testbed, and showed that even in this very low-friction environment, the disturbances are more than an order of magnitude higher in the lab than on orbit. [48] *Wise* did an analysis of the torque that the magnetorquers could reasonably produce and the disturbances expected, and concluded that the disturbances on orbit are well within the torque rods' ability to manage momentum. [20]

## 5.3 Estimator Results

As described in Section 4.4.2.1, the attitude as estimated on-orbit could not be directly replicated in the laboratory environment. Thus, the magnetometer and the accelerometer were used for attitude estimation. While this combination of sensors will not be used in flight, they can still give valuable information about the performance of the Extended Kalman Filter.

### 5.3.1 Illustration of EKF Performance

One of the ways to look at the performance of a Kalman filter is to look at its covariance over time. If a filter converges to a good attitude estimate, the elements of its covariance matrix should decrease to some steady-state values. The intuitive approach, of course, is to look at the estimate of the state before and after filtering, and see if it looks cleaner.

Figure 5-3 shows the six elements on the diagonal of the covariance matrix with respect to time on a logarithmic scale. The reader can see that the elements briefly increase, and then settle by about 10 seconds after the filter begins. This settling of the covariance to

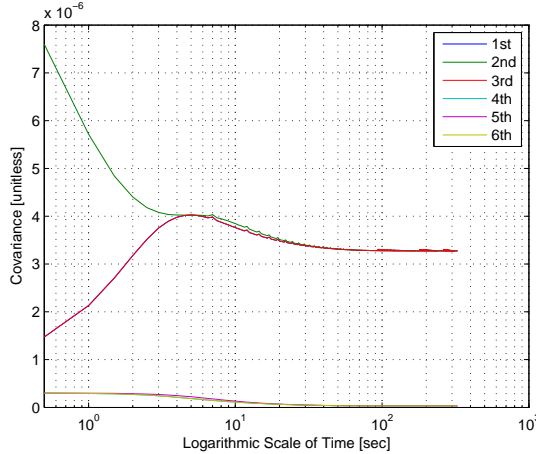


Figure 5-3: Covariance Matrix with respect to Logarithmic Time Scale

steady-state is exactly what we would expect.

Over that same time, Figure 5-4a shows the estimated quaternion vector elements before and after filtering. The filtering is easiest to see on the x-axis or vector 1, where the measurement is the noisiest. A zoomed-in look at the filtered estimate versus the measured estimate is shown in Figure 5-4b.

Some tuning was performed in order to achieve this performance. Noise characteristics of the sensors were observed and their characteristics were used as inputs to the covariance matrix. Some of this can be re-used for flight, since the magnetometer and the rate gyros will still be used for on-orbit operations.

### 5.3.2 Making the Filter Robust to Changes in Sensor Inputs

Figure ?? shows what happens to the estimates of the attitude and angular rate if the filter is not reset when a sudden change of sensors occurs in formulating the quaternion. The angular rate jumps up to account for the sudden change in attitude and takes about 4 minutes to recover. However, in reality, the satellite has not rotated. This shows that instantaneous

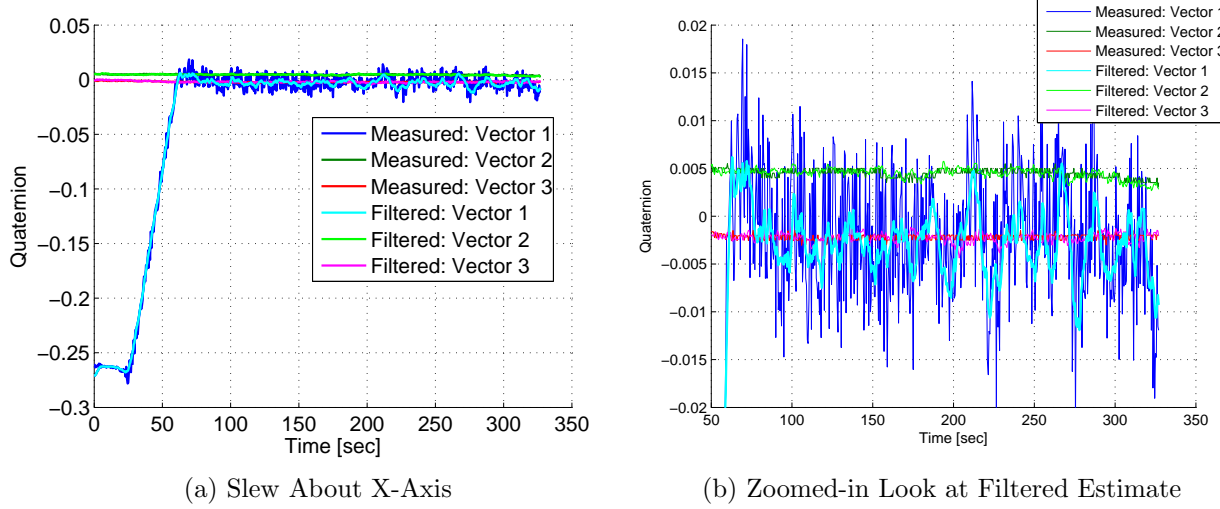


Figure 5-4: Measured vs Filtered Quaternion

change in sensor inputs for attitude estimates could cause serious problems with the attitude estimates, confusing the controller, and causing it to take action when it should not.

To address the problems of instantaneous jumps in attitude estimates from switching

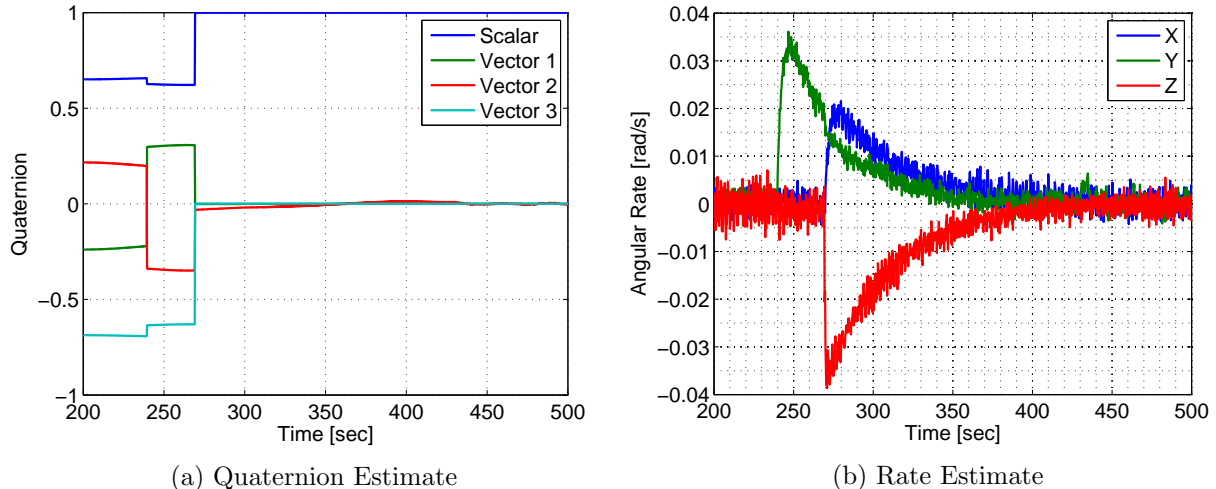


Figure 5-5: Instantaneous Change of Sensor Inputs to Attitude Estimate

sensors, a lot of logic checks were implemented. These logic checks ensure that the measurement and the estimate do not diverge by too much. If they do, the filter will prefer its estimate over its measurement. Whenever switching from an attitude estimate using one

suite of sensors to another, the attitude from both are computed. If they agree within a threshold, the sensor with the higher accuracy will be used. When this switching occurs, the filter resets. This initially results in high covariance estimates, and thus a slightly noisier attitude and rate estimate from the filter. However, these settle within a matter of a few seconds. This is much better than if the filter did not know about the switch to new sensors, and instantaneously switched to a new attitude measurement. The filter would then ignore the update if it did not agree closely enough with its previous estimates. Extensive testing was performed on all of these checks to ensure the transitions would be seamless for on-orbit operations.

Figure 5-6 shows the rate and the attitude estimate after a commanded EKF-reset

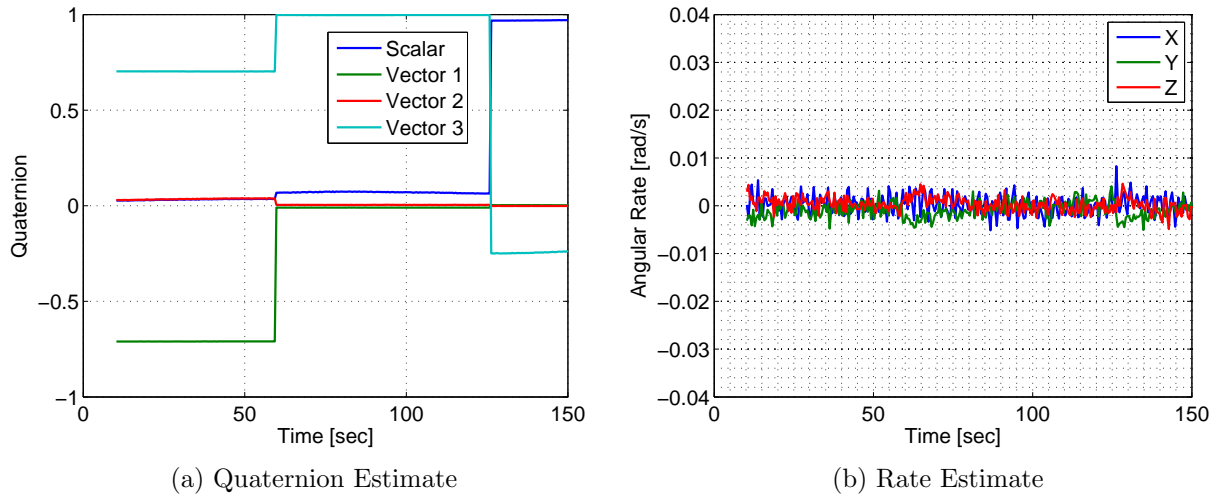


Figure 5-6: Kalman Filter Reset: Instantaneous Change of Sensor Inputs to Attitude Estimate

due to a change in attitude information. The quaternion, shown in Figure 5-6a, transitions cleanly and instantaneously. This kind of jump in attitude would not happen autonomously, because the estimates are so different. The logic would catch the difference not allow the change, because it would assume that the new sensor is in error. However, the EKF can be commanded to be reset, as in the case shown here. The estimated rate, on the right,

essentially shows no change. That is because the EKF only estimates the bias of the gyro, and does not actually filter the rate. Compare this to the rate from Figure 5-5 - it accurately reflects the actual state of the satellite, showing no rotation. Thus, these plots show the ability of an EKF reset to handle sensor changes without hiccups. This idea of a filter reset has been studied by *Diop et al.*, under conditions where the measurements are corrupted. They determine that resetting the filter is a way to achieve global convergence. [49]

## 5.4 Detumble Mode

Recall from Chapter 4 that the test for Detumble Mode consists of comparing the time responses of the non-actuating case with the B-dot algorithm case. Both should act as under-damped harmonic oscillators, with the difference being that the actuating case should show a significantly higher damping coefficient. Five trials on two different axes for each case were run. The results were then fitted to an exponentially decaying function and solved for to find the damping ratio and natural frequency, as described in equations 4.2- 4.6.

### 5.4.1 Piñata Tests about the X-Axis

The satellite is hung inside the Helmholtz Cage with its body x-axis oriented perpendicular to the magnetic field, as shown in Figure 5-7. The initial offset of the system is to approximately 90 degrees, or 1.57 radians. The satellite is then released from this angle and allowed to oscillate until it reaches its neutral non-rotated position. Figure 5-8 shows an example of a non-actuating case, followed by an actuating case with freedom of rotation in the x-axis. Recall that the B-dot control law uses magnetorquers, which produce torque normal to both the actuator and the magnetic field.

Figure 5-8 shows the x-axis attitude measurement in radians with respect to time, with

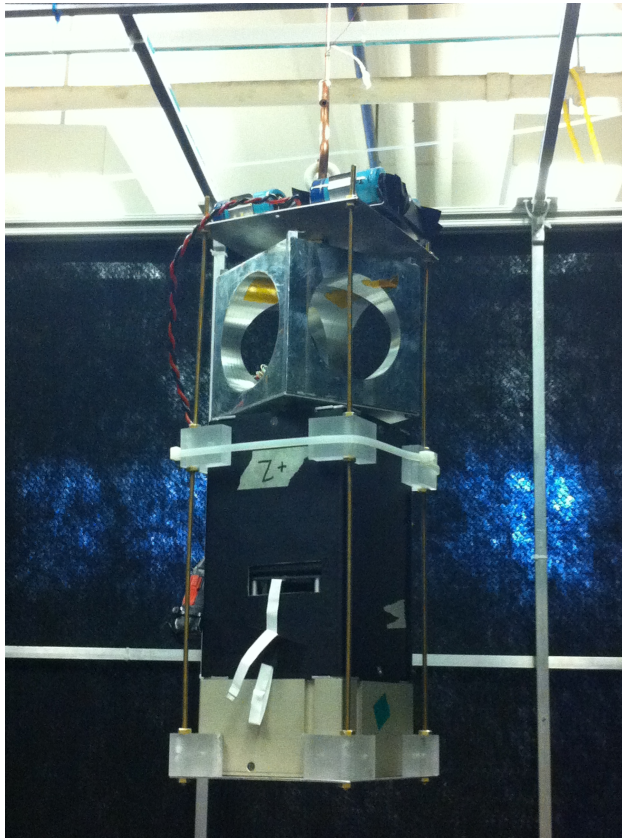
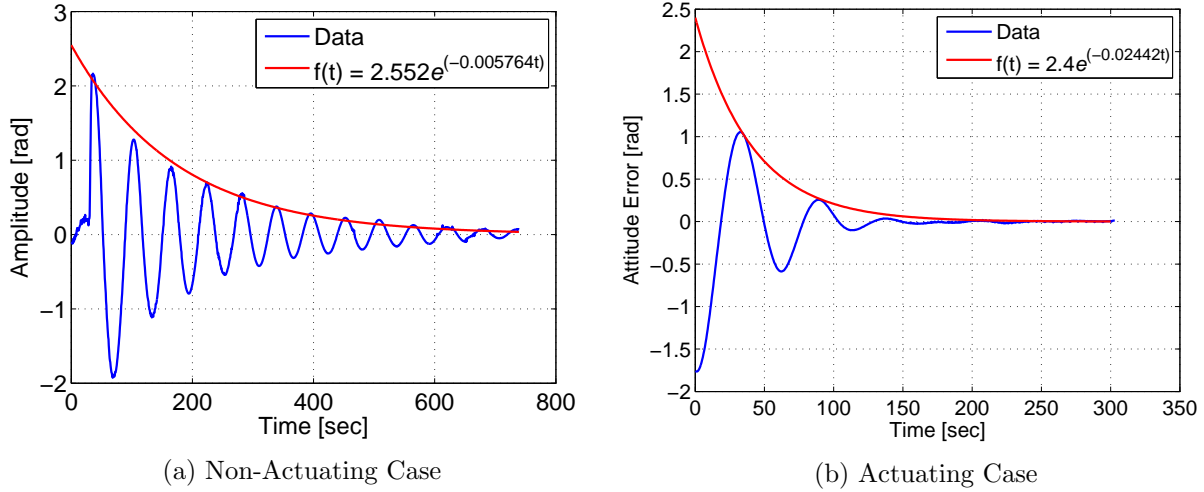


Figure 5-7: EM Satellite Hanging in Cage with its Body X-Axis Along Axis of Rotation

an exponential decaying function fitted to the responses. This fit was achieved by taking the points from the tops of the amplitudes with respect to time, and using a non-linear least squares best fit analysis for an exponential function.

Using the exponential coefficient  $b$  from equation 4.3 describing the exponential decay, and the measured damped frequency of oscillation  $\omega_d$  (simply the reciprocal of the measured period of the time response multiplied by  $2\pi$ ), the parameters of the system can be solved for, as described in Section 4.3.3. The values can be checked by evaluating them against a simulation, to see how well they match the actual response. The model simply has feedback of the angular rate and position, using the damping coefficient and the natural frequency to estimate the response.

Figure 5-8: Comparison of Detumble Tests along X Axis



The expected values for the actuating case (2) are based on the response of the non-

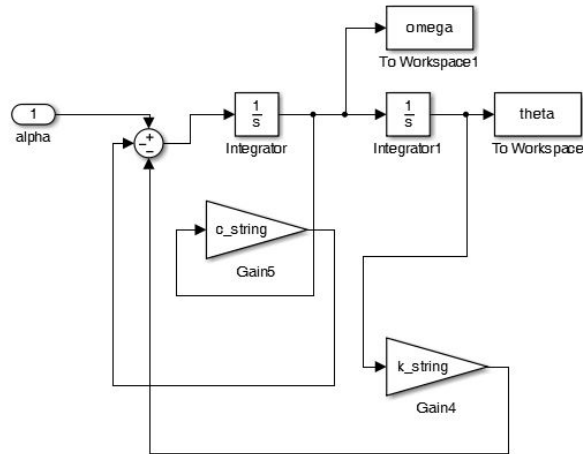


Figure 5-9: Simple Model of String as Second-order System

actuating case (1) and the known value of the magnetic field.

The damping of the measured actuating case is more than double that of the non-actuating case - a clear indication that increased damping is occurring. This effect is also visible from the more than halving of the settling time (defined as the time it takes to go

Table 5.1: Parameters of the Time Response: X-Axis

<b>Response</b>	<b>Damping Coefficient <math>\zeta</math></b>	<b>Natural Frequency <math>\omega_n</math> (rad/s)</b>
Measured: Non-Actuating Case	0.0520	0.1069
Predicted: Actuating Case	0.2137	0.1069
Measured: Actuating Case	0.2049	0.1191

from the initial offset to within 2% of the final steady-state value) seen in the actuating case - about 195 seconds in Figure 5-8b vs about 680 seconds in Figure 5-8a. Note the different time scales along the x-axis on the figures.

The predicted damping coefficient differs from the measured damping coefficient of the actuating case by about 4%. The natural frequency of the two cases, differed by about 11%. These differences are within the bounds of acceptable measurement error, based on the uncertainty of the measured period of the damped oscillatory motion. The  $1\sigma$  bound on the period is about  $\pm 6$  seconds, which translates to a  $1\sigma$  range in the natural frequency of about  $\pm 0.014$  radians per second and about  $\pm 0.024$  for the damping coefficient.

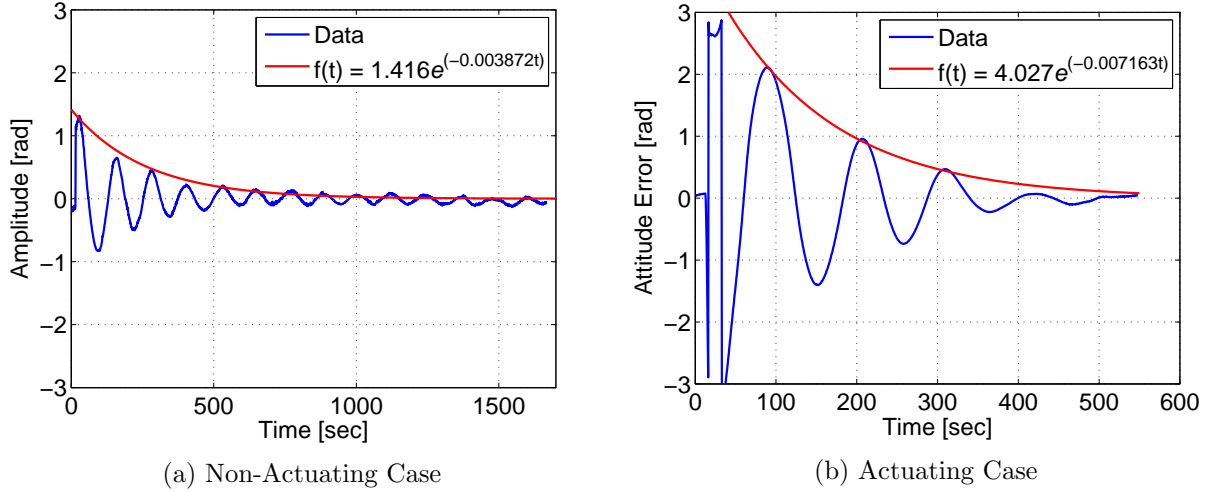
#### 5.4.2 Piñata Tests about the Y-Axis

The same result must be shown in one more axis, since actuation along the x-axis only proves that the magnetorquers in the y and z axes are working properly. Figure 5-10 shows results along the y-axis. Note that it takes much longer for the settling to occur in both cases - this is because the inertia about the y-axis is about a factor of 3.5 greater than the inertia about the x-axis. This means that the same amount of torque due to damping from both the air

and the magnetorquers will have less effect, due to the inverse relationship between inertia and angular acceleration with a constant torque.

Notice that the actuating time response starts at a higher amplitude. This is because

Figure 5-10: Comparison of Detumble Tests along Y-Axis



when the satellite was offset to only 90 degrees, it damped out so quickly it was difficult to capture the time response. Thus, the initial condition for that actuating case was an offset of 180 degrees. However, as long as the initial conditions for both cases are known – even if they are not identical – the response can still be described completely and compared to the prediction.

The measured damping coefficient matches the predicted  $\zeta$  within 5%, while the measured natural frequency matches the predicted  $\omega_n$  within 18%. There is uncertainty in capturing the frequency of the damped oscillation, as before, and the standard deviation of that period is 15.6 seconds. This yields  $1\sigma$  bounds on the damping coefficient of  $\pm 0.017$  and on the natural frequency of  $\pm 0.009$  rad/s. Again, these results fall within one standard deviation of the known measurement uncertainty.

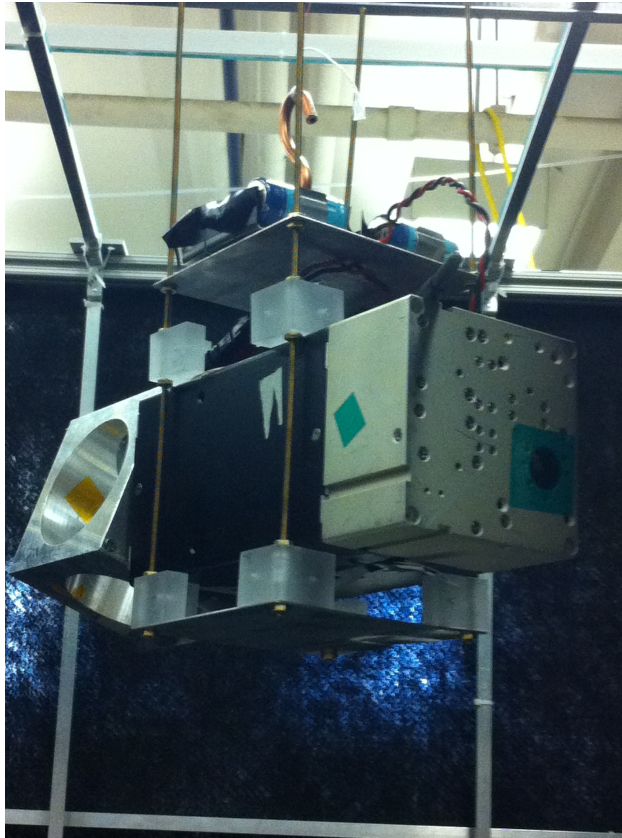


Figure 5-11: EM Satellite Hanging in Cage with its Body Y-Axis Along Axis of Rotation

Table 5.2: Parameters of the Time Response: Y-Axis

<b>Response</b>	<b>Damping Coefficient <math>\zeta</math></b>	<b>Natural Frequency <math>\omega_n</math> (rad/s)</b>
Measured: Non-Actuating Case	0.0797	0.0515
Predicted: Actuating Case	0.1089	0.0515
Measured: Actuating Case	0.1134	0.0608

### 5.4.3 Reading the Signs

Data processing is not all number crunching. Sometimes, it takes an attentive eye to evaluate the results qualitatively, in addition to quantitatively, to find if something is amiss.

The reader will recall that when the tests for the B-dot algorithm were outlined, it was mentioned that the response should be sinusoidal. The data in Figure 5-12 was collected for an actuating case oriented about the y-axis.

It is difficult to see unless one inspects the plot closely, but this sinusoid is not sym-

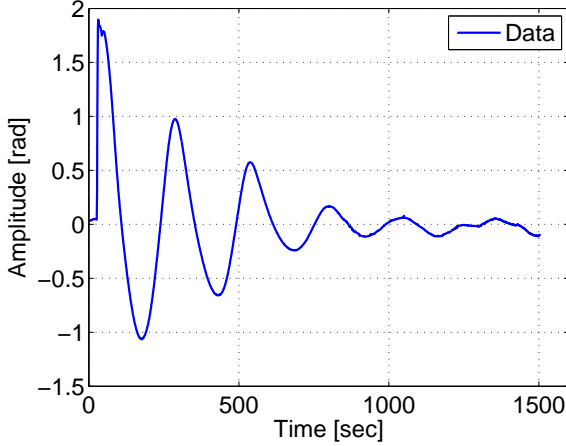


Figure 5-12: Actuating Case with One Sign Error

metric. It is especially visible on the third period, where the right edge rises faster than the left edge falls. Another graduate student who was helping review this data, and pointed it out. It turns out that this asymmetry was an indication of a sign error: the sign on the previously untested x-axis magnetorquer was incorrect.

To verify that this was the only magnetorquer with a sign error, we changed the sign on the z-axis magnetorquer as well, so that both would be the opposite of what they nominally should be. In theory, this change would not only not damp the system, but should provide torque in the opposing direction.

In Figure 5-13 when both signs are changed on the commands to the actuators, not only does damping not occur, but the control algorithms actually excite the system. The amplitude of oscillation increased and held indefinitely. This was a clear indication about the correct orientations of the signs on the controller, as well as the power of the magnetorquers when aligned with a strong magnetic field.

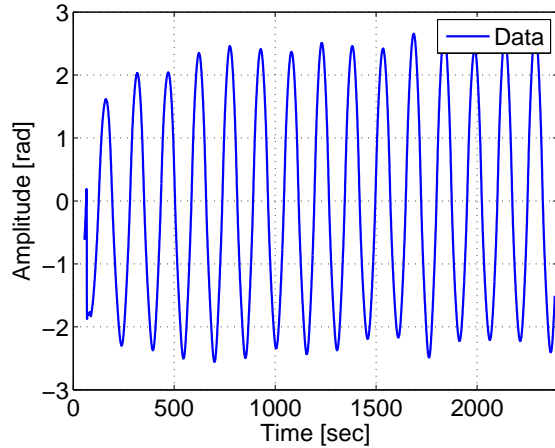


Figure 5-13: Actuating Case with Both Signs Incorrect

Finding problems like the sign error emphasizes the importance of testing all relevant test configurations that involve not only different aspects of software, but different pieces of hardware. Then, when a problem is found, the engineer must run tests to figure out whether the problem is in the software or the hardware, or both.

## 5.5 Slew Mode

Slew mode will be evaluated with the metrics discussed in Section 4.4. A model of the controller along with the string dynamics was created, in order to validate the test results. The string response was quantified via the damping coefficient and natural frequency parameters discussed in Section 5.4. The control torque of the controller is known (see Section 2.4) and the inertia of the satellite has been modeled. All of these parameters are then placed into a model to predict the system's response, and then the results are evaluated with respect to this model.

### 5.5.1 Setting up the Test

To evaluate Slew Mode, we had to create an environment where a rotation was possible, and then model that test set-up in order to evaluate the results. As discussed in Chapter 4, the test set-up consisted of hanging the satellite from a string inside the Helmholtz Cage, allowing limited freedom of rotation about the axis perpendicular to the floor. Since eigenaxis slews could not be verified in this set-up, each axis had to be tested independently.

The first step of setting up the test was to calibrate the response of the string, so that it could be modeled. Luckily, this was already done for two axes in the testing of Detumble Mode. Thus, all that was left was to calibrate the second order approximation of the string response about the z-axis. The damping coefficient and natural frequency of the string response was then used to solve for the proportional and derivative gains. These terms were then put into the model to see how the system would respond to slewing maneuvers, when it would be actively fighting that restoring force.

Next, a strong magnetic field (on the order of about  $150 \mu\text{T}$ , or approximately 3 times larger than the expected magnitude of the field on orbit) is set up within in the cage in the plane parallel to the floor, so that the magnetorquers would be able to produce torque in the axis perpendicular and thus aid in the rotation. The job of the magnetorquers during all modes after Detumble is to help desaturate the reaction wheels. Thus, since these tests are uniaxial, the magnetorquers can be directed to produce torque in that particular axis to aid the reaction wheel performing the maneuver.

Once the satellite is hung inside and is stationary at its neutral position, the slew can commence. The attitude is set such that the initial attitude is some angular distance away from the desired attitude in the axis of rotation. We chose a value of 30 degrees, because slews much larger than that cannot stabilize for long before the reaction wheels saturate (due fighting the restoring torque of the string). Then, the control law with the actuators are enabled, and the satellite begins to respond. The following are the results of these tests.

### 5.5.2 Modeling the Test Environment

The author created a simulation which models the controller, the string dynamics, and the reaction wheel response to the controller. The controller was modeled with its proportional, derivative, and integral terms and the string was modeled as a second-order damped harmonic oscillator. The other terms from the controller can be neglected. One of these terms accounts for the gyroscopic torques due to the reaction wheels spinning, which have also been left out of the model. The two torques should cancel each other, so they need not be included. Likewise, the feed-forward term for the payload has been neglected, since it should simply cancel the torque caused by the acceleration of the payload.

The terms for modeling the response of the string come from the same test described

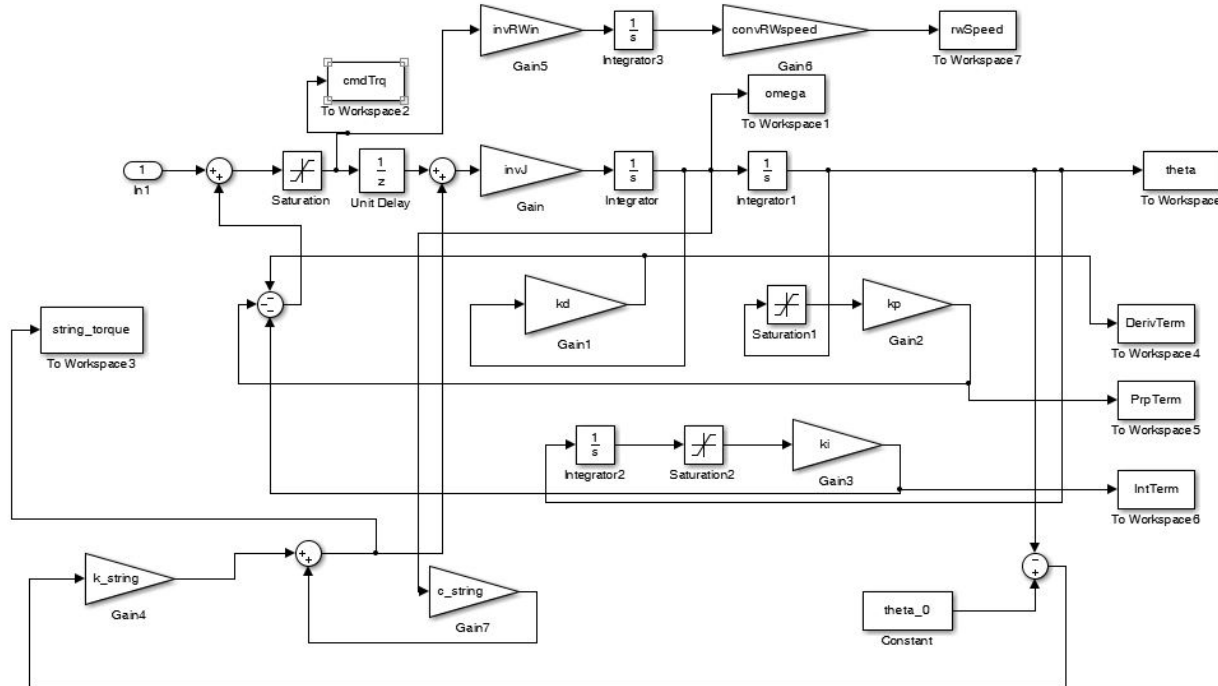


Figure 5-14: Simulink Model of Satellite with Restoring Torque due to String

as the control for testing the B-dot control law in Section 5.4, where the satellite is offset

and then allowed to oscillate until it comes to a stop at the neutral position of the string. The damping coefficient  $\zeta$  and natural frequency  $\omega_n$  solved for in Section 5.4 were used to find the terms  $k_d$  and  $c_d$  in the equation describing the response of the system. These gains  $k_d$  and  $c_d$  were then used in the simulation to describe the restoring torque that the string imparts on the system. It is important to remember that the gains are different for each axis, due to the differing responses of the system in different orientations. These terms are also multiplied by the inertia about the relevant axis, in order to be scaled properly.

All components were modeled as scalars, with the variables being changed with respect to each axis. The torque starts at the left side, then gets divided by the inertia, in order to get acceleration. The acceleration is then integrated, with an initial condition of the initial angular rate. This angular rate, called *omega*, is then integrated again with an initial condition of the initial attitude at the start of the test. Feedback terms *kd*, *kp*, and *ki* refer to the derivative, proportional, and integral gains discussed in Chapter 2. The derivative gain *kd* gets applied to the measured rate error, the proportional gain *kp* gets applied to the attitude error, and the integral gain *ki* gets applied to the integral of the attitude error. There are saturations on the proportional and integral terms, which limit them from becoming too large and driving the control torque. These three terms get summed to yield the control torque, as in equations 2.42, 2.43, and 2.47.

The string is modeled at the bottom of the diagram in Figure 5-14, with the angular rate multiplied by the term  $c_{string}$  and the angular position offset multiplied by the term  $k_{string}$ . These two gain terms include multiplication by the inertia about the axis of rotation, yielding the proper units for torque (see equation 4.1. The reaction wheel speed is also estimated (shown at the top of Figure 5-14, by taking the control torque, dividing by the inertia of the reaction wheel, integrating to get a rate, and then converting from radians per second to revolutions per minute.

### 5.5.3 Slewing about the X-Axis

Five tests were performed with the same initial condition of a 30 degree offset with no initial angular rate. The satellite slewed to the desired position. The initial conditions of each test were put in the model and the time response of the model was then compared with the actual data collected. Thus, the model in Figure 5-14 can be used as a metric from which to compare the responses of the system. The rise time, settling time, and steady-state error of the results and the model of the time response of the attitude will be compared in Table 5.3.

Figure 5-15 shows the results of a slew maneuver about the x-axis. The red shows the model based on the original parameters solved for using the damping coefficient and natural frequency found for the non-actuating test of the satellite about its x-axis, from Section 5.4.1, shown in red. Modifications were made to the model, shown in green. The adjustments will be discussed in more detail in Section 5.5.3.1.

Figure 5-15a shows the attitude error, converted from quaternions to radians. Figure 5-15b shows the angular rate as measured by the gyroscope. Figure 5-15c shows the control torque, as commanded to the reaction wheels. Figure 5-15d shows the speed of the reaction wheels.

#### 5.5.3.1 Accounting for Modeling Error

The model had to be adjusted from its initial parameters to more accurately model the torque of the string. The initial damping coefficient and natural frequency solved for from the B-dot case were not capturing the dynamics properly. We believe this is due to the fact that  $\zeta$  and  $\omega_n$  are coupled in the way that we have to solve for them. (See equations 4.3, 4.5, and 4.6.) The relationship of  $\zeta$  and  $\omega_d$  to the decay function fitted to the curve was maintained, but the relationship to the measured  $\omega_d$  was called into question. There is some uncertainty about this measurement, since the time between periods varies by about 8 seconds  $3\sigma$ . However,

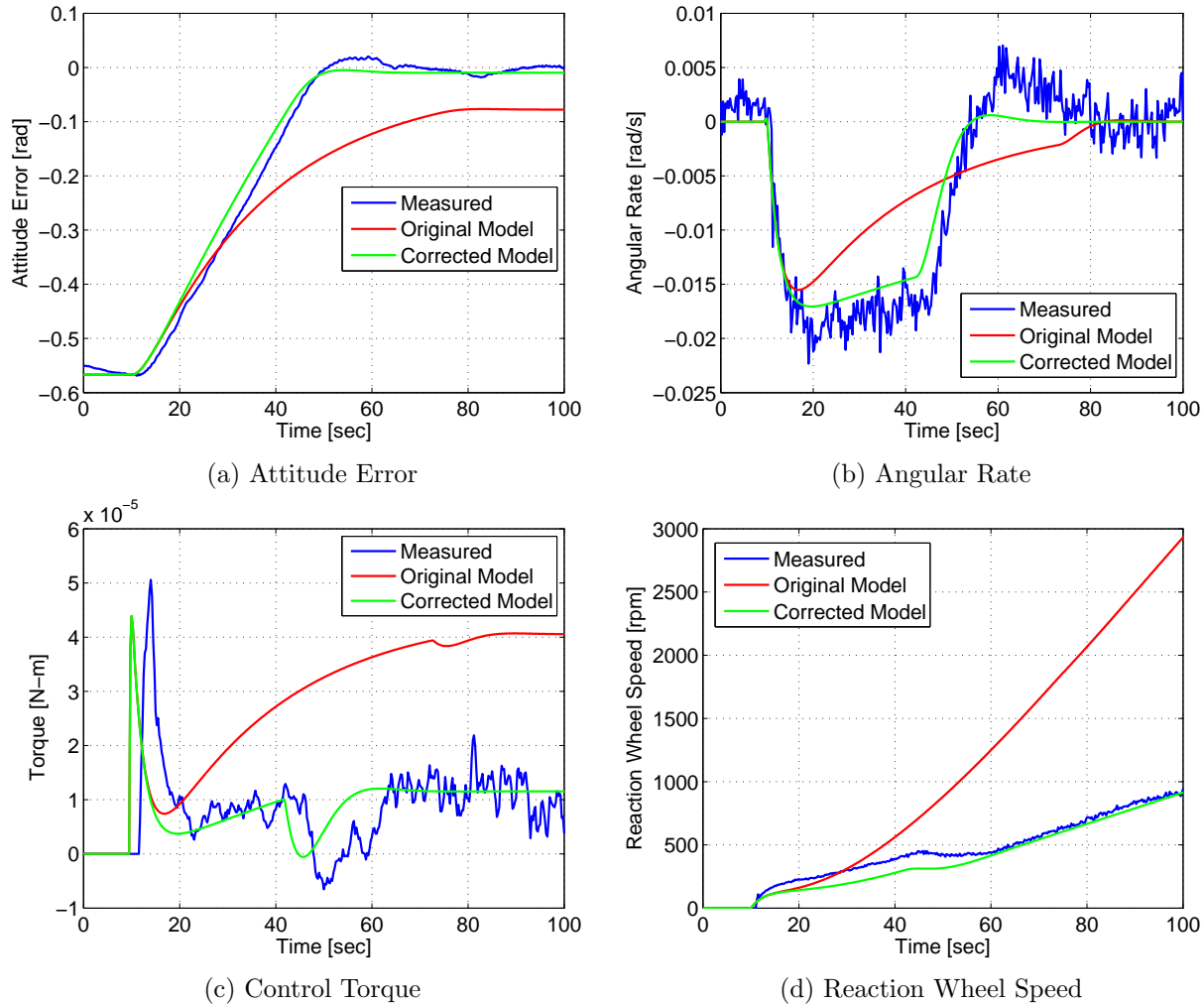


Figure 5-15: Time Response of a Slew about the X-Axis

even with this uncertainty accounted for, the difference between the original model and the corrected model is still too great.

Despite not knowing why the parameters would be so dramatically different, we have confidence that the corrected model is representative of the system. This confidence comes from the fact that the steady-state control torque from the simulation matches the commanded torque from the response (see Figure 5-15c). This constant non-zero torque that the controller must provide to maintain its attitude is a direct result of the torque provided by the string. In the original model, this torque was estimated to be much higher than what it was observed to be.

Accepting this corrected model, the rise time, settling time, and steady-state error of the time response of the attitude are shown in Table 5.3.

Table 5.3: Parameters of the Slew Maneuver: X-Axis

<b>Response</b>	<b>Rise Time <math>t_r</math></b>	<b>Settling Time <math>t_s</math></b>	<b>Steady State Error <math>e_{ss}</math></b>
Predicted: Example Case	28.75	60.0	-0.0096
Measured: Example Case	28.25	65.0	-0.0044
Percent Difference	1.7%	8.3%	0.9%

The rise times match up extremely well, with only a 1.7% difference between the corrected model and the data. However, the settling time doesn't match up quite as well. We believe this is due the inherent instability of the final attitude that the satellite must hold. A zoomed in look at this response is shown in Figure 5-16. The satellite is fighting the torque of the string, and has only feedback of attitude and rate error to account for that torque. This means that the controller can only correct for errors after they occur, rather than provide the necessary torque up front. We could have modeled this torque and put it back into the controller as a feed-forward term, but decided it would be better not to modify

the controller with terms it would not see in flight.

The time response of the attitude error shows that there is an overshoot, before the

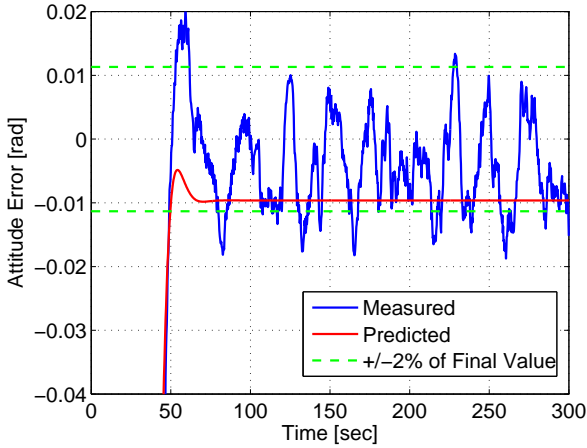


Figure 5-16: Zoomed-in Look at Steady State Response of Slew: X-Axis

error drops back down. However, it technically doesn't actually settle within the traditional boundaries of  $\pm 2\%$ , due to this instability. Thus, the settling time was defined as when the system reached its final steady-state value after its first overshoot. The oscillation after the overshoot is limitation of the test environment, and not indicative of the controller and hardware's performance on orbit in a much lower disturbance environment.

#### 5.5.4 Slewing about the Y-Axis

The same analysis was repeated for the a rotation about the y-axis. Five trials were run, with an example case shown in Figure 5-17. This case is representative of all five trials of a 30 degree slew about the y-axis. The model shown in red comes directly from solving for the response of the string from the non-actuating case about the Y-Axis, discussed in Section 5.4.2.

In Figure ??, the response about the y-axis appears to be critically damped, meaning it

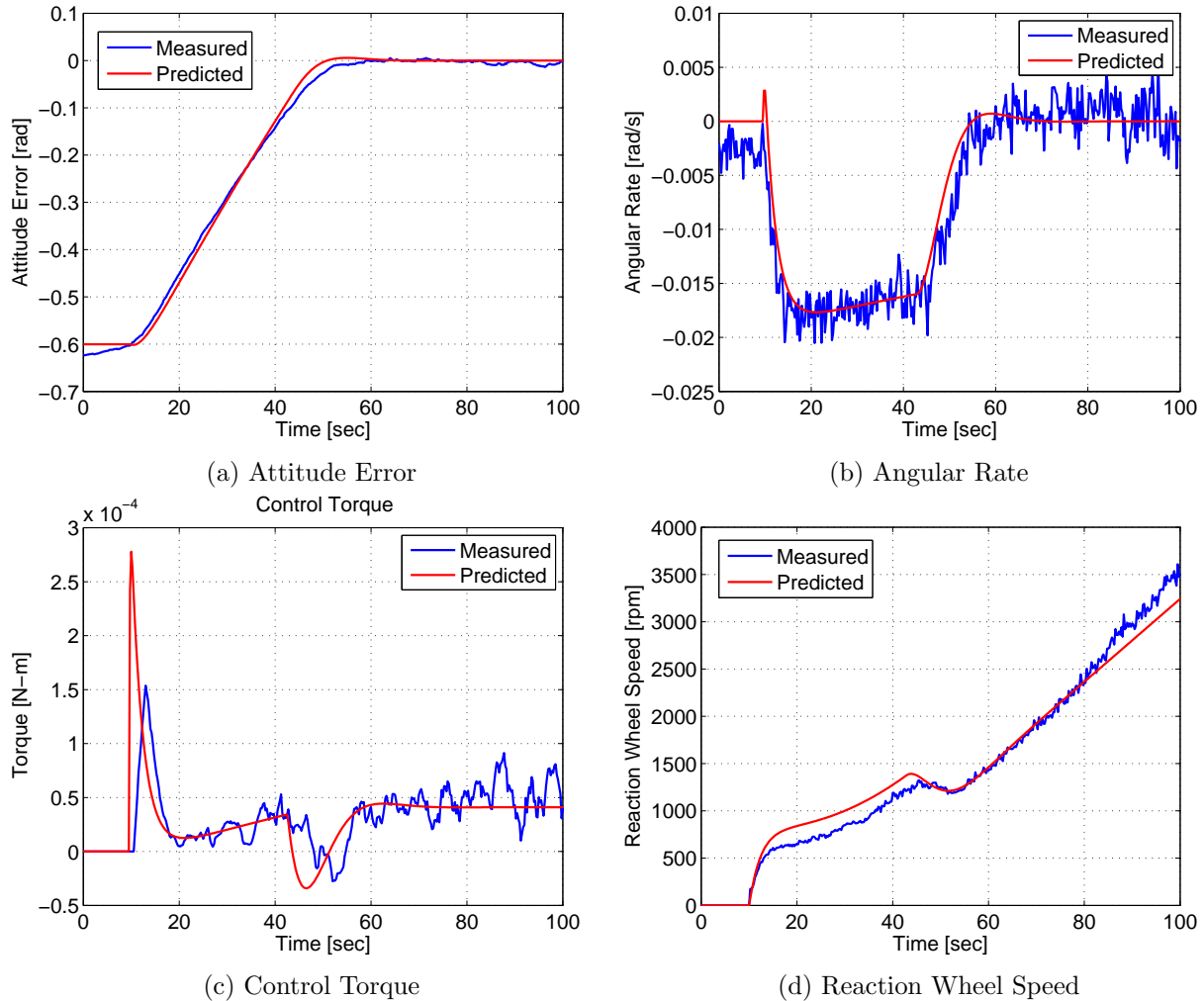


Figure 5-17: Time Response of a Slew about the Y-Axis

has no overshoot. The model actually shows a slight overshoot. Table 5.4 below summarizes the results of this trial, compared with the predicted responses from the model.

Table 5.4: Parameters of the Slew Maneuver: Y-Axis

Response	Rise Time $t_r$	Settling Time $t_s$	Steady State Error $e_{ss}$
Predicted: Example Case	28.5	38.25	0.0000
Measured: Example Case	31.25	40.75	-0.0054
Percent Difference	9.6%	6.5%	0.9%

The rise time matches the model to within 9.6%, the steady-state error matches to within 6.5%, and the average steady-state error matches to less than 1%. The measured response stays to within  $\pm 2\%$  of its final value for about 175 seconds, but then starts to emerge from those bounds. This is due to the reaction wheels spinning up to their maximum speed, where they are no longer able to provide torque.

Again, the reason this oscillation occurs is that the satellite is fighting a constant torque

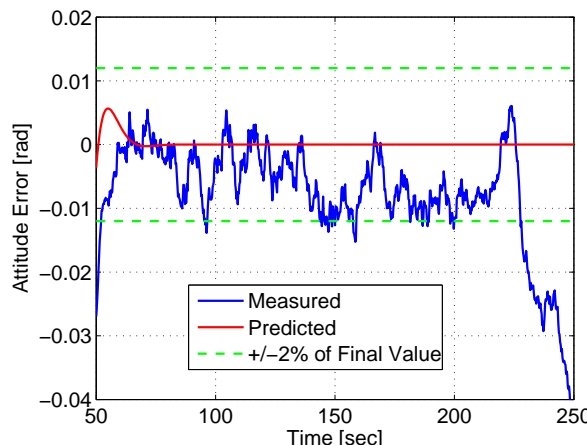


Figure 5-18: Zoomed-in Look at Steady State Response of Slew: Y-Axis

provided by the string when it has slewed to its commanded attitude. That is what causes the oscillations to occur around the steady-state value. Since the control law does not have a term accounting for this constant torque, it only can respond after a deviation has occurred. This will manifest itself in torque being applied to the reaction wheels in spurts to fight the attitude and rate error that the satellite senses. Thus, the response looks oscillatory. Eventually, the reaction wheels are unable to match the restoring torque of the string, which causes the satellite to lose its control authority.

However, this is not a concern for real on-orbit operations because there will be no constant restoring torques on the satellite, causing it to saturate its reaction wheels. It is assumed that disturbances the satellite will encounter on-orbit are expected to be lower frequency as well as lower torque, which the feedback control law can recover from. [15]

### 5.5.5 Slewing about the Z-Axis

The final axis that the control law in conjunction with the actuators needed to proven in is the z-axis. The results will be presented in the same manner as described above, beginning with an example of representative 30 degree slew maneuver about the z-axis. The model shown is from matching the parameters, as discussed for the other two cases, about the response of the satellite hung with its +Z axis along the axis of rotation.

The parameters of the time response of the attitude are enumerated in Table 5.5. The rise time and settling time match to 11.1% and 12.9%, respectively. The steady-state error is even closer, although – as in the other cases – the steady state error of the measured response is an average, rather than an actual steady value. As can be seen from the zoomed in plot in Figure 5-20, the slew about the z-axis has oscillates, similar to the responses seen in the other two axes.

Despite these limitations, the maneuvers are close enough to the model that they satisfy

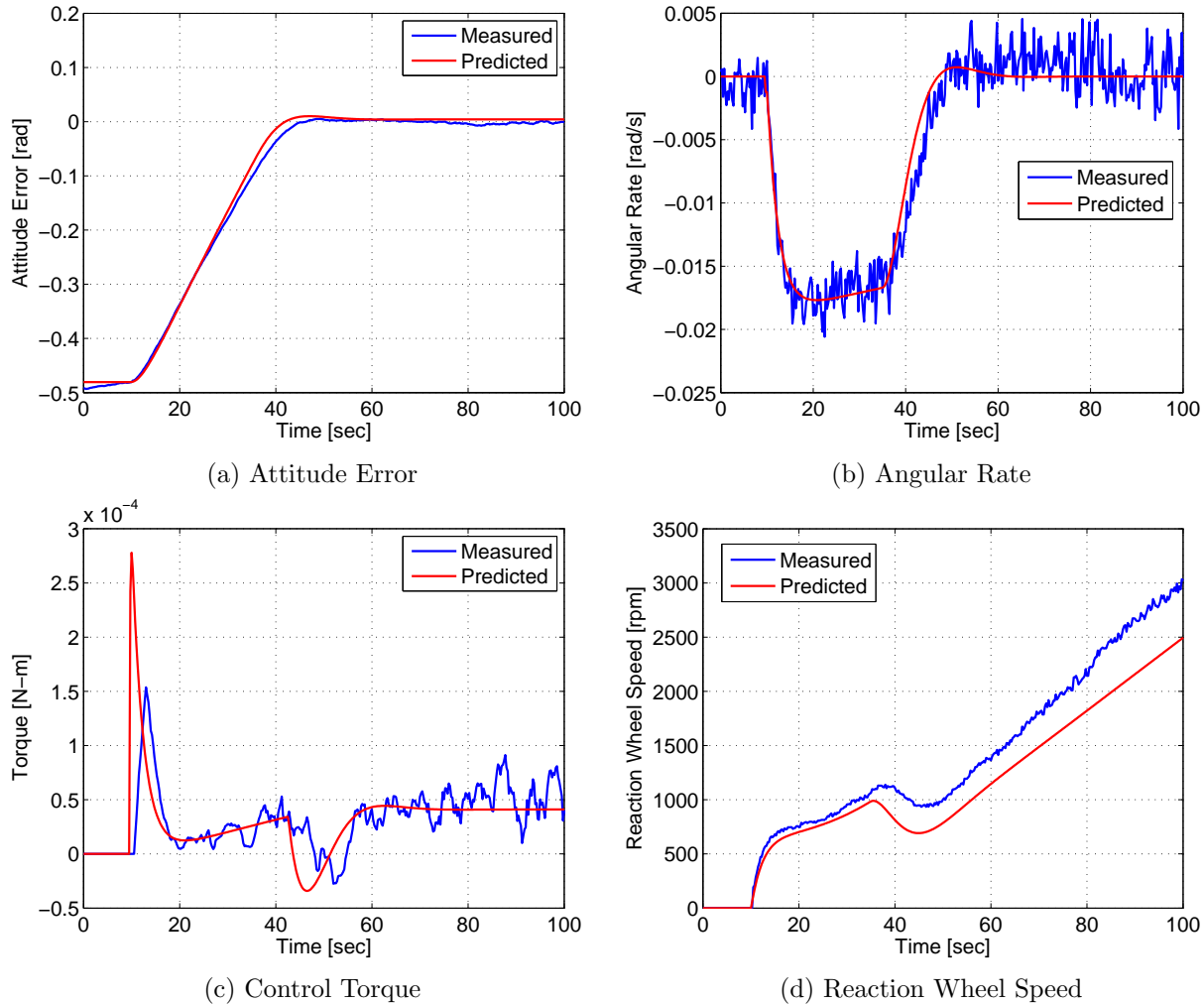


Figure 5-19: Time Response of a Slew about the Z-Axis

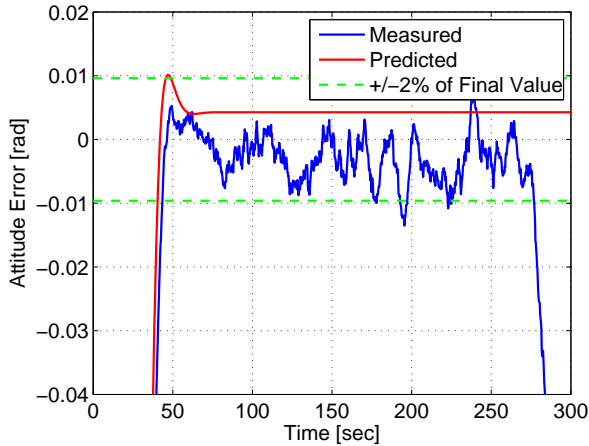


Figure 5-20: Zoomed-in Look at Steady State Response of Slew: Z-Axis

Table 5.5: Parameters of the Slew Maneuver: Z-Axis

Response	Rise Time $t_r$	Settling Time $t_s$	Steady State Error $e_{ss}$
Predicted: Example Case	22.5	52.5	0.0043
Measured: Example Case	25.0	59.25	-0.0031
Percent Difference	11.1%	12.9%	1.6%

the requirements of slewing to the correct angle within the defined threshold. The reason that they do not maintain that angle is due to a disturbance that will not be present on-orbit.

## 5.6 Spin-up & Stabilization Modes

### 5.6.1 Spinning up the Payload

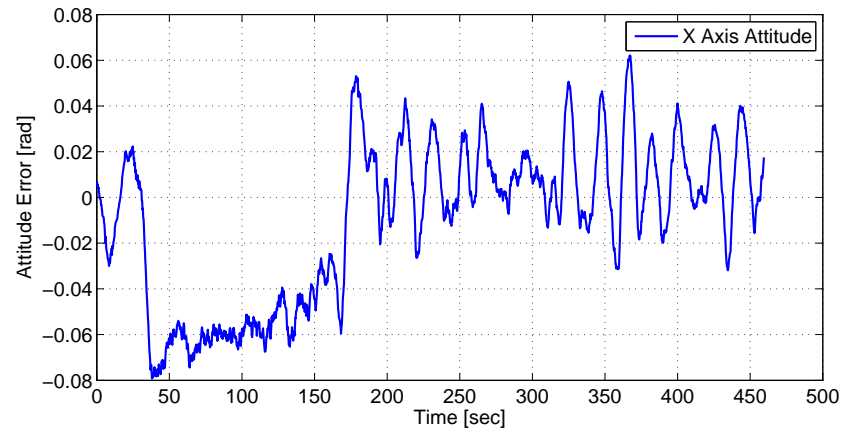
In the conops of MicroMAS, after it has slewed to its commanded attitude and been able to hold steady there for about 25 seconds without deviating from that attitude, it goes into its Spinup Mode. During this mode, the scanner assembly will accelerate from its initial zero speed to a final speed. The control law has a feedforward term to counter the torque on the satellite caused by this rotation. Essentially, with no delays, the satellite should remain motionless during the spin-up period.

The results of a spin-up test are shown in Figure 5-21. This test will only be presented about the x-axis, since that is the axis along which the scanner assembly is aligned and will impart torque. Figure 5-21b shows the attitude along the x-axis. Figure ?? shows the reaction wheel speed in revolutions per minute. Figure 5-21c shows the rotation rate of the payload simulator.

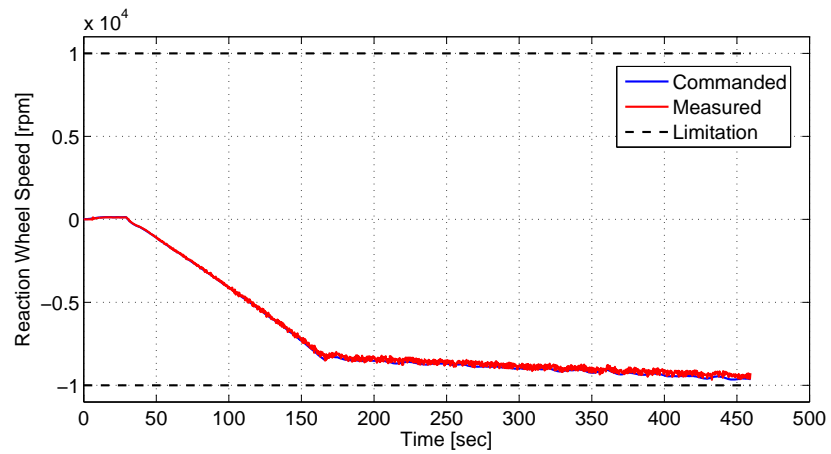
Despite our best efforts to alert the control law to the spin-up of the payload in the same control cycle, there is still a delay from command to actuation on the part of the reaction wheels. Thus, the initial “kick” from the start of the acceleration causes an offset of about 0.05 radians, or 2.9 degrees, as can be seen in Figure 5-21b. This behavior was observed repeatably, whenever the scanner assembly began its motion.

Initially, we thought this offset might be due to the control law not having enough time to recover from the disturbance provided by the initialization of the motor. This initialization consists of a commutation search by the motor, which imparts an unpredictable torque on the system. However, even after lengthening the time between the initialization and the commencement of the acceleration, the impulse response of the torque still causes the satellite to rotate a few fractions of a radian.

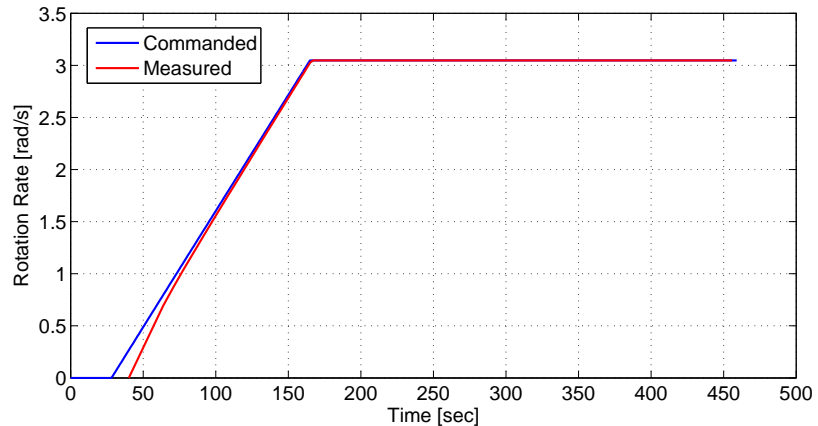
Mathematically, this makes sense. If the timing of the application of the feed-forward



(a) Attitude Error



(b) Reaction Wheel Speed



(c) Payload Simulator Rotation Rate

Figure 5-21: Payload Spin-up

term is not actualized by the reaction wheels at exactly the moment when the scanner assembly begins its acceleration, the torque imparted to the system acts like an impulse function. Thus, the system responds by an almost instantaneous attitude perturbation.

This initial offset was maintained throughout the spin-up profile. We attribute this to the canceling of the attitude error correction term with the feed-forward term. However, after the acceleration was completed, the system was able to recover back to a mean of zero attitude error, with a deviation of about 0.032 rad or 1.85 deg ( $3\sigma$ ).

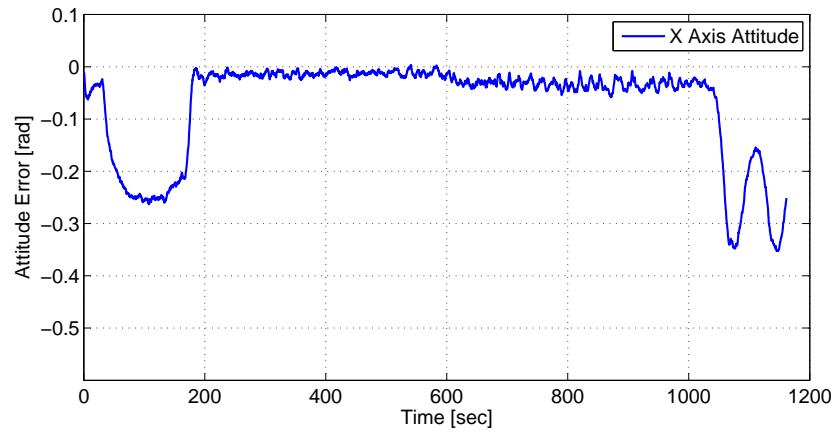
### 5.6.2 Stabilizing after Payload Spin-up

In order to analyze the ability of the controller to keep the system at its commanded attitude after spin-up, the satellite must be placed in a dynamically unstable attitude. In Section 5.6.1, the payload spin-up was performed with the satellite hanging from the string in its neutral, unperturbed position. Thus, the control law had to cancel out the effects of the spinning payload, by maintaining conservation of angular momentum in the system. It did this by spinning its x-axis reaction wheel up to a speed that would provide the same amount of momentum as the payload at its final speed.

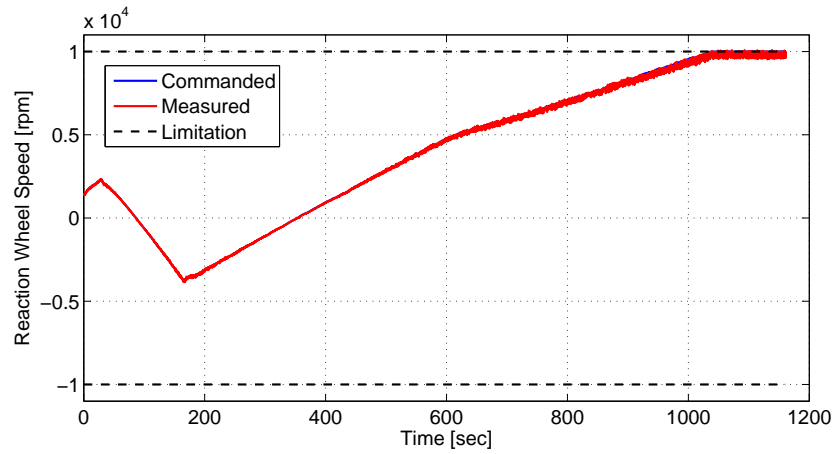
Since angular momentum is simply the product of angular rate with the inertia about the axis of rotation, the speeds of the payload and the reaction wheel are proportional to the ratio of their respective inertias, as discussed in Chapter 4. However, the system must also be able to respond to disturbances to maintain its attitude. In order to test this, a slew maneuver followed by an autonomous transition to payload spin-up was performed.

Figure 5-22 is analogous to figure 5-21 presented above. However, the response is quite different, due to the initial condition of dynamic instability for this case in order to show the controller's ability.

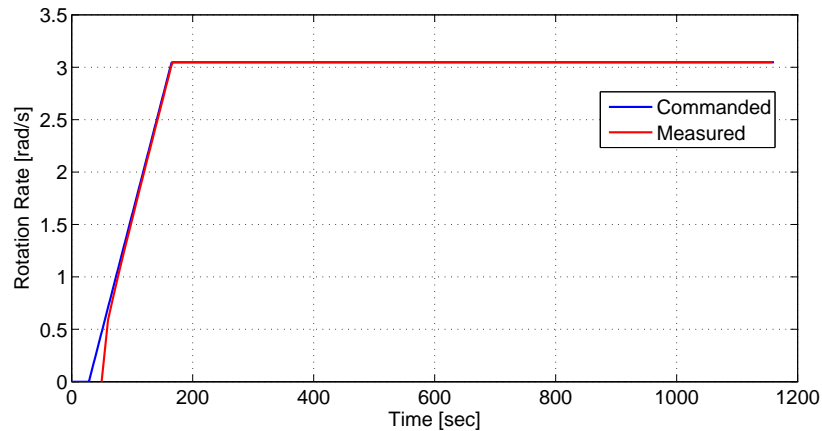
The reader will notice that the attitude offset during spin-up in this trial is about 8 times



(a) Attitude Error



(b) Reaction Wheel Speed



(c) Payload Simulator Rotation Rate

Figure 5-22: Stabilization During and After Payload Spin-up

larger than the previous one. It increased to about 0.25 radians, or almost 15 degrees. We attribute this to be due to the dynamic instability of the starting attitude, since the system completed a slew before beginning spin-up. It is thus about 30 degrees off from its neutral position on the string and is already fighting that restoring torque when the acceleration of the payload kicks off. In flight, the satellite should behave more like what was observed in Figure 5-21, since the satellite will not be in an inherently unstable position when it is on-orbit.

It is important to note that despite the larger initial offset in attitude during the spin-up, it remains roughly constant during the spin-up, and then the system successfully returns to its mean of zero attitude error state. This deteriorates only when the reaction wheels have reached their saturation limit. Recall from Section 5.2.2 that the torque capability of the reaction wheels degrades as their speed increases. This is noticeable from the slight deviation from zero-mean around 600 seconds, when the reaction wheels are around 7000 rpm. At that point, they are still able to apply torque, but not as much as is needed.

A plot of the reaction wheel torque over this same maneuver is shown in Figure 5-23. Four different torque values are shown. The first is the torque commanded from the controller. The second is the torque that the reaction wheel unit receives as a command from the software. The third is the torque that is measured by taking a first order derivative of the tachometer-measured wheel speed and multiplying it by the estimate of the reaction wheel inertia (given by the vendor). The fourth is the torque that comes from the first-order linear fit shown in Figure 5-2.

It is difficult to tell in Figure 5-23, but there is a quarter-second delay from when the command is issued from the controller and when it is reported in the next reaction wheel unit packet. The software was timed such that the computation involving the torque commanded by the controller would be finished within the 250 millisecond cycle to be able to be sent to the actuators. However, even meeting that constraint, there is still some non-zero time

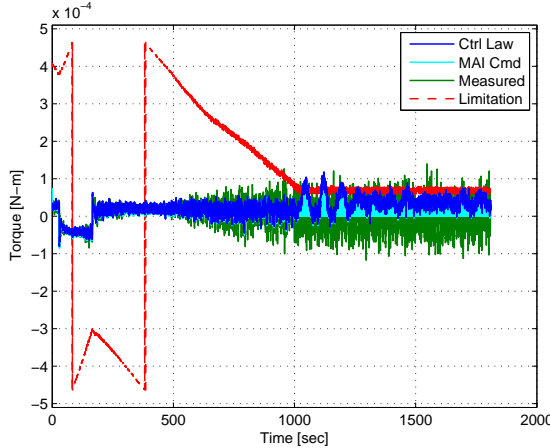


Figure 5-23: Torque of X Reaction Wheel During Spin-up and Stabilization

it takes for the reaction wheels, upon reception of the torque command, to increment their speed appropriately.

The reader will also notice is that measured torque gets very messy after about 1000 seconds, when the reaction wheels have saturated. The measured torque at that point is just the noise due to the tachometer measurements, and the system is providing very little torque. This illustration of torque degradation is important to take into account when evaluating the system response. However, in flight, the disturbances are much less, and the magnetorquers should be able to help to desaturate the reaction wheels continuously, thus avoiding the commanded torque reaching its limits.

### 5.6.3 Zero G Flight Results

MicroMAS was able to test its engineering model satellite on a Zero G flight in April 2014. Replicating the complete freedom of rotation that a satellite has on-orbit in a 1-g environment is difficult. However, even in the opportunity of a Zero-G flight, the microgravity environment only lasts about 20 seconds at a time. In this amount of time, it is difficult to

truly be able to see if a controller is responding appropriately to its environment.

Between the tops of the parabolas, which are the zero-g portions of the flight, there are higher-g periods during which the plane must dive and climb again. During these periods, the satellite must be secured. During the free float periods, the responsible parties must ensure that the satellite does not translate too far away and disturb another experiment.

Given these constraints, we observed that the EM satellite had at most four seconds of free float before it had to be nudged by a crew member in order to not exceed its allotted volume aboard the aircraft. We also observed that during each 2-g pull-out period, the reaction wheels immediately accelerated to their maximum speeds. This made it difficult to observe commanded rotations, since the satellite was severely limited in its torque-providing capabilities.

The results of these tests will be released in a later document. The preliminary conclusions are that the tests helped validate performance of hardware under both zero-g and higher-g loading conditions. The performance of the controller, due to the limitations mentioned, is more difficult to quantify. In the brief periods where the satellite was able to float without disturbances, the controller exhibited encouraging behavior. However, the zero-g tests were inconclusive in terms of validating ADCS algorithms, and the suspension tests elucidated in Sections 5.4- 5.6.2 are much more useful in the validation process.

# Chapter 6

## Discussion of Test Results and Model

This chapter will go over the test results, discuss the model used to evaluate the results, and come to conclusions about this method of testing the attitude determination and control of small satellites.

### 6.1 Discussion of Test Results

#### 6.1.1 Estimator

The Extended Kalman Filter was tested in the trials run for the various slew, spin-up, and stabilization mode tests. The attitude estimate, while not exactly made up of the same sensor information that will run on-orbit, is analogous to the flight attitude estimates. The TRIAD algorithm was shown to combine two vectors from two different sensors, compare them to references, and generate a quaternion. This quaternion was then passed into the EKF with gyro rates, just as it will on-orbit.

The filter ran exactly as it would on-orbit, with measured quaternion and angular rate as inputs, and a filtered quaternion and angular rate with updated biases as outputs. These were then used as the attitude and rate estimates for the feedback loop in the controller.

The plots of the covariance and the filtered quaternion in Figures 5-3 and 5-4a show that the filter does, in fact, work as expected. The covariance settles quite quickly to a steady-state value, which shows that the filter has good estimates of the process and sensor noise that become essentially constant. The plot of the filtered attitude estimate overlaid with the measured attitude estimate also show more intuitively that the filter is giving an optimal estimate of the state.

Figure 5-6 shows the filter after it is reset on two different occasions, where it recovers without a problem to new sensor inputs. Figure 5-5 shows plots where the filter is not reset when the sensor inputs are abruptly changed, and the resulting effect on the filter. Thus, it has been shown that the filter is robust to sensor input changes to the attitude estimate, which is critical for flight operations.

### 6.1.2 Detumble Mode

The results of the Detumble tests show that the measured responses were within 1 standard deviation of the predicted responses. One of the challenges in capturing that prediction accurately comes from properly accounting for the saturation of commanded dipole. Recall from equation 4.16 that the predicted value of the damping coefficient of the actuating case is dependent upon the dipole commands of the magnetorquers. However, these commands are proportional to the angular rate of the satellite, which is not constant. Thus, this value had to be approximated by a two-step process. The first was to estimate the largest value of the angular rate, and then to use that for  $\omega$  in equation 6.1. The value for the product of  $k |\mathbf{B}|$  is then constrained. This value is then multiplied by the actual measured magnetic field  $|\mathbf{B}|$  in equation 4.16, yielding equation 6.2.

$$k |\mathbf{B}| \omega = 0.108 \quad (6.1)$$

$$\zeta_p = \frac{2\zeta\omega_n J + \left(\frac{0.108}{\omega}\right) |\mathbf{B}|}{2\omega_n J} \quad (6.2)$$

In addition, to validate the analyses of these tests, the results were compared to a simulation. The torque provided by the magnetorquers was modeled as described in Chapter 4, with the saturation in place.

The results show that the model of the magnetorquers matches the data even better than

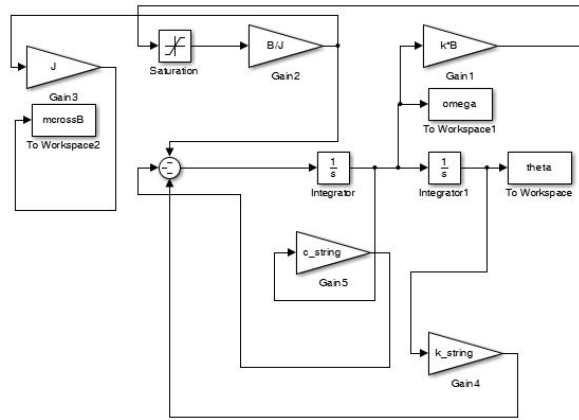


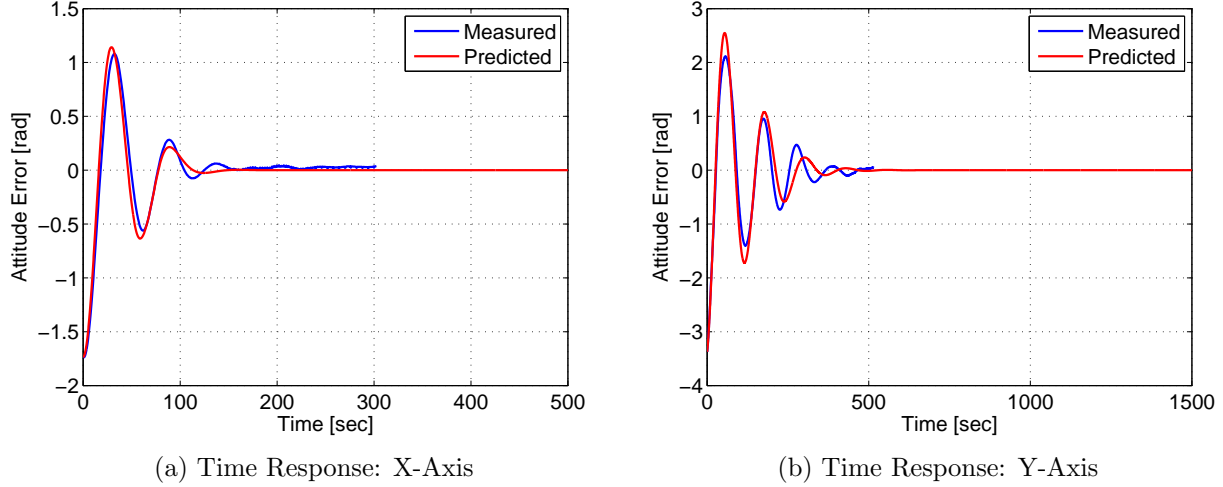
Figure 6-1: Simulation of Hanging Test of Detumble Mode

the exponential curve fit.

One important observation of these results is that a second-order differential equation that assumes a constant  $\zeta$  and  $\omega_n$  does not appear to exactly fit the data. We believe that this is because the exponential decay of the curve of the string response itself is independent on position. In other words, the damping coefficient and natural frequency appear to be a function of angular position - the string appears to behave differently for large angle offsets rather than smaller ones.

To test this theory, we used the parameters that were solved for by fitting the exponential decay function to the non-actuating case, which only models the natural response of the string when loaded with the satellite in a particular orientation, to put back in the model.

Figure 6-2: Prediction of Magnetorquer Effect on Damping Compared with Actual Data

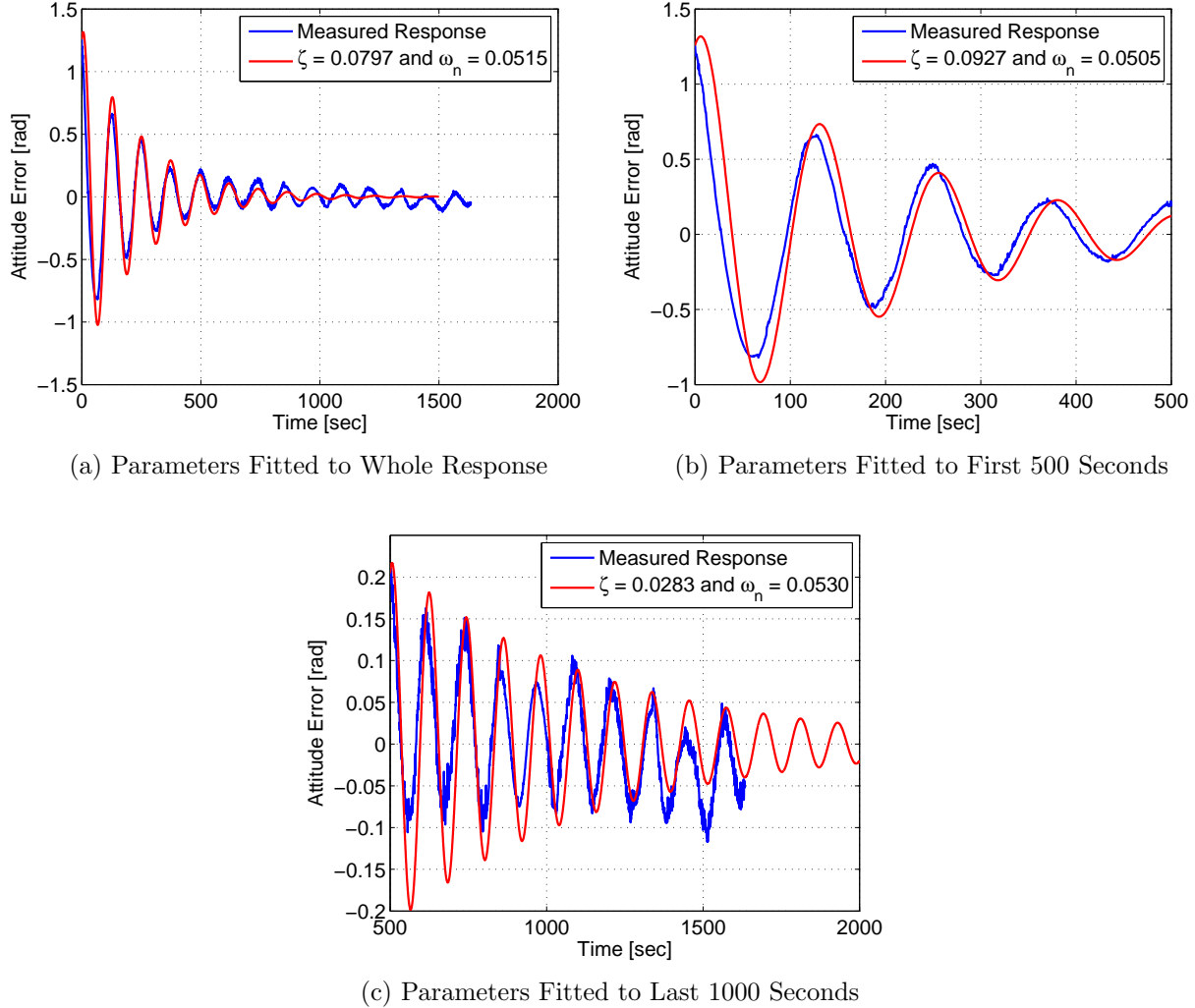


The magnetorquers were turned off, and the response was analyzed.

As can be seen in Figure 6-3, the best exponential decay fit changes as the amplitude changes. Figure 6-3a shows the model with parameters fit to the full time response. Figure 6-3b shows a model with parameters fit to the first few amplitudes. Figure 6-3c shows a model with parameters fit to the smaller amplitudes. The damping coefficient between the three varies from 0.0927 in Figure 6-3b, to an average of 0.0515 in Figure 6-3a, to only 0.0283 in Figure 6-3c. This decrease in damping coefficient with respect to amplitude tells us that the string response is not strictly a second-order system.

Despite this limitation, the model was accurate enough to match the data within  $1\sigma$ . The tests about the x- and y-axes show that the Detumble algorithm in conjunction with the magnetorquers successfully damp out rotation rates as predicted. The cases with the signs on the commands flipped also show the actuation of the magnetorquers. The requirement of the Detumble Mode are to slow the satellite to a tumbling rate of less than 1 degree per second. While this cannot be literally shown in this test, since the restoring force of the string naturally wants to restore the system to a non-rotating state, the results of the tests validate that the B-dot algorithm works as predicted. Simulations with on-orbit conditions

Figure 6-3: Modeling the String Response as a Second Order System



were performed by other members of the MicroMAS team to verify that the 1 degree per second benchmark could be reached. [20]

### 6.1.3 Slew Mode

As discussed in Chapter 5, there are many limitations to the piñata test set-up. The chief one is the restoring torque of the string, which has proven difficult to model. This leads to some discrepancy between the model of the controller within test set-up and real system

performance. However, despite these challenges, in each axis, the controller in conjunction with the reaction wheels was able to perform the slew maneuver. The oscillation after the maneuver is not desirable, but can be attributed to the restoring torque of the string. Thus, the important part of the model for the slew itself is the rise time. In each case, the maneuver matched the model to within 15%, and in some cases, much better than that. This gives confidence that the algorithms and hardware working together are able to achieve the objective of Slew Mode.

#### 6.1.4 Spin-up Mode

What these figures reveal is that the controller is able to hold the satellite at a steady attitude during spin-up, but that attitude is offset a few degrees from its commanded attitude. After the spin-up is complete, the controller successfully guides the satellite back to its commanded attitude with a small steady-state error before the reaction wheels lose their ability to provide more than 0.1 N-m of torque.

The requirement for Spin-up Mode was to hold the satellite to within 1 degree ( $3\sigma$ ) of its commanded attitude. However, this has proven not to be possible with the constraints of time delay and hardware. With no external torques acting on the system, the attitude deviated by about 0.07 radians ( $\sim 4$  degrees), and then slowly recovered during spin-up to 0.03 radians ( $\sim 1.7$  degrees), and finally to a steady-state of about 0.009 radians ( $\sim 0.5$  degrees). This behavior is analogous to what would be expected on-orbit.

While this performance falls outside of the prescribed requirements for Spin-up Mode, these requirements flow from an overall conops. If the best effort was put forth to achieve the requirements, but they are still elusive, sometimes it is best to return to the big picture of the overarching mission of the satellite. The science objective for MicroMAS is to take radiometer measurements of the atmosphere with the payload spinning at a constant rate. The pointing requirement flows from that objective – to be able to hold the satellite steady during

its science data collection. Thus, even with some slight angular offset, as long as the satellite is able to recover after spin-up to within the required bounds, the mission is not compromised. Therefore, the performance presented here is good enough for this particular mission.

### 6.1.5 Stabilization Mode

The requirement for Stabilization Mode was to hold the satellite steady to within 1 degree ( $3\sigma$ ). Thus, if the slight steady-state error (due to test set-up) is disregarded, the controller working with the reaction wheels met this requirement. We believe that this steady-state error is due entirely to the restoring torque of the string, and the controller's lack of knowledge about this torque. Therefore, it only commanded enough torque to restore the satellite to a zero attitude error state if it were in a friction-free environment. The proportional gain term is not large enough to overcome that constant restoring torque. The integral term would help in this case, but it too is saturated at 10 degrees and is scaled to be a factor of 10 lower than the proportional gain. Thus, taking into account the limitations of the test set-up, the controller has been shown to perform as expected.

## 6.2 Robustness of Model

The model used to evaluate these test results, like any model, has its limitations. It does not account for the messy translation of the commanded reaction wheel torque, through the quantization and discretization process to wheel speed, nor the imperfect performance of the wheels. The model attempts to capture the dynamics of the restoring torque provided by the string, but these terms were solved for experimentally and are thus uncertain. A brief sensitivity analysis of the model will be presented in order to explore these uncertain terms

and their effects on the response of the system.

### 6.2.1 Exploring Uncertainties

There are four terms in the model that are uncertain for each axis, which actually results in nine total uncertain terms. These terms are the proportional and derivative gain terms describing the restoring torque of the string, as well as the scalar value of the inertia of the satellite about the axis of rotation and the scalar value of the inertia of the reaction wheel about its axis of rotation. All of the other terms have been selected by the controller, and the initial conditions are known. Since the inertia of the reaction wheel only affects the wheel speed prediction, its uncertainty was not investigated.

### 6.2.2 Inertia of the Satellite

The values for each of these unknowns has been modeled and put into the simulation. The inertia about each axis comes from a CAD model of the satellite [17]. We do not believe that the uncertainty surrounding this term is very high, due to two separate results. The first result is that the CAD model predicted the mass of the satellite to be 2.97 grams, and it was measured to be 2.91 grams - a difference of only 2%. While this does not guarantee the accuracy of the inertia, this was a good first-order comparison to boost confidence.

To be thorough, we ran a brief sensitivity analysis on how dependent the model is on the accuracy of the inertia estimate. With no adjustments, the model tracks the actual performance about all three axis to within 15%. The goal of this analysis is to see if by adjusting some parameters, the model shows closer results. Figure 6-4 shows a slew about the y-axis, along with various models. The only parameter that was changed between the models is the estimate of the inertia.

In Figure ??, the blue shows the actual measured response; the red shows the model

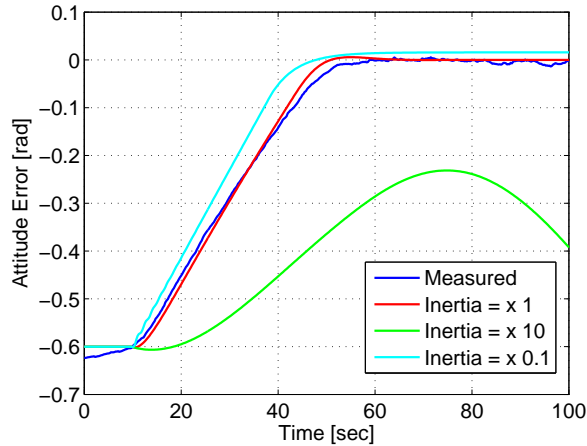


Figure 6-4: Comparison of Data with Models with Varying Inertia Estimates

with no adjustments; the green shows the model with an inertia estimate that is 10 times the CAD model prediction; the cyan shows the model with an inertia estimate that is 0.1 times the CAD model prediction. While this only affects one axis, the response is representative of how a change in inertia would affect each axis, since none of the blocks change between modeling the various axes.

It is important to note that the inertia in the model does not change everywhere. There are inertia terms that are used within the controller to determine the appropriate gain to apply. This inertia is fixed based on the estimate of the CAD model. However, the a change in the actual inertia of the system would be realized in the decomposition from torque to acceleration, and thus its integration (twice) yielding angular position. It would also affect the response of the string.

It is clear from Figure 6-4 that the inertia estimate from the CAD model is pretty close to the actual inertia of the system, based on how different the factor of 10 and 0.1 responses are from the measured response.

### 6.2.3 Proportional and Derivative Gains of the String

The next uncertain terms that were explored are the gains determining the restoring torque of the string. The Simulink model of the system (see Figure ??) not only gives an estimate of the attitude, but also of the angular rate, control torque, and reaction wheel speed. Since each of these are also known values, they can be compared to see how well the model fits the data.

The damping coefficient of the system was solved for in the method described in Section 4.3.3, with the time response fitted to an exponential decay function. This exponential decay function was then used to solve for the parameters of quadratic equation, assuming it can be represented as a second-order under-damped system. This analysis had to be performed for each axis, since the restoring torque is dependent upon the inertia. These tests, the results of which were discussed in Section 5.5.1, yielded the damping coefficient and the natural frequency of the system.

Since the gains are directly related to the natural frequency and damping coefficient (see equations 4.7 and 4.8), adjusting those parameters would subsequently have an effect on the model of the string torque. Some iteration was performed to see if it were possible to guess the correct values of these terms that would mitigate differences between the model and the observed response.

### 6.2.4 Damping Coefficient that Models Response of String

As it turns out, changing the damping coefficient of the system has a limited effect on the response. This is due to the fact that the rate is relatively small for the entire maneuver (never exceeding 0.1 radians per second or about 5 degrees per second). Figure 6-5 shows data from a slew about the x-axis overlaid with models with varying damping coefficients.

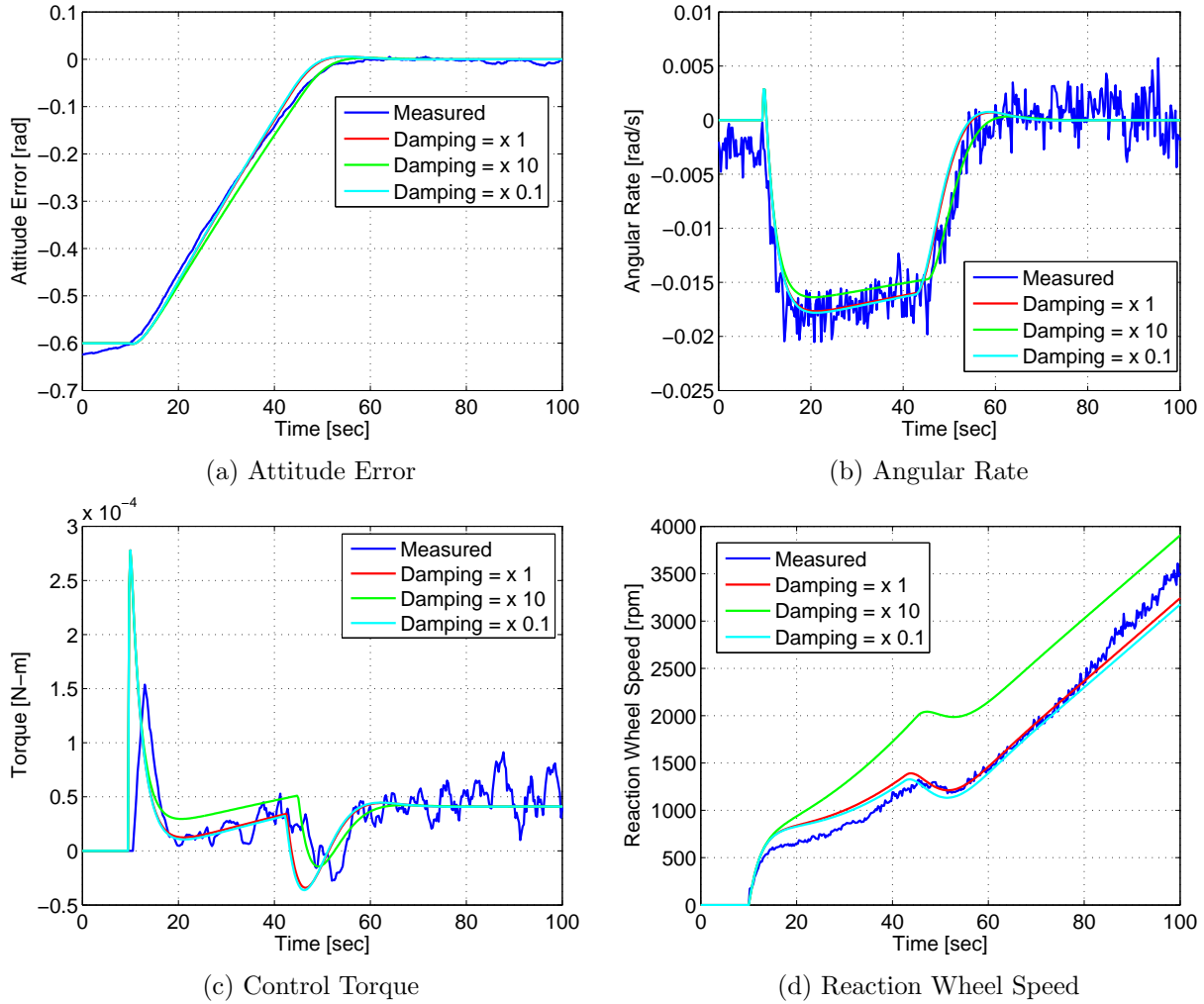


Figure 6-5: Model Response to Changing the Damping Coefficient of the String

Figure 6-5a shows the attitude with respect to time, with varying damping coefficients of the string modeled. Figure 6-5b shows the angular rate. Figure ?? shows the predicted vs measured commanded torque for the same set of damping coefficients. Figure 6-5d shows the reaction wheel speed that results from the commanded torque. It is interesting to note the various effects that a changed damping coefficient has on these responses. The y-axis is shown, since that is the axis whose response matches the model most closely; therefore, any effects of changing the parameters are evident.

The response of the attitude seems to change little by varying the damping coefficient.

The rise time increases for the higher value of the damping coefficient, but does not seem to correspondingly decrease by much for a lower value of  $\zeta$ . The angular rate and control torque are not too noticeably different with the various damping coefficients. The reaction wheel speed shows a marked increase in its initial slope for a higher damping coefficient, but not much difference with a lower damping coefficient.

### 6.2.5 Natural Frequency that Models Response of String

The natural frequency of the system is the final unknown in the model. It is also the value over which we have the least confidence, since it is based on a measurement of the damped natural frequency of the system. The periods between peaks would vary by up to 10-20 seconds, which leaves some ambiguity about the actual frequency. In addition, analytical solution presented here to solve for the natural frequency is dependent upon the damping coefficient of the system in addition. Thus, the two are coupled. If the damping coefficient was incorrect, then the natural frequency would also be wrong.

We did a similar analysis as for the damping coefficient, varying the natural frequency and observing the response. All other parameters were left unchanged. Figure 6-6 has the same order of plots as seen before, to observe all of the repercussions of changing the model.

Similarly to adjusting the damping coefficient, it appears that a decrease in natural frequency does not change the model very much. However, an increase in the natural frequency changes the response quite a bit. In the attitude error, shown in Figure 6-6a a factor of ten increase causes the system to never reach equilibrium. This would be saying that the string is so strong that the system cannot get past about 0.1 radians of rotation. The angular rate, shown in Figure 6-6b drops back down to zero pretty quickly, because the model thinks the string response is so strong that the system cannot rotate. The torque, shown in Figure 6-6c exhibits an increase in control torque required in order to counter the restoring torque felt

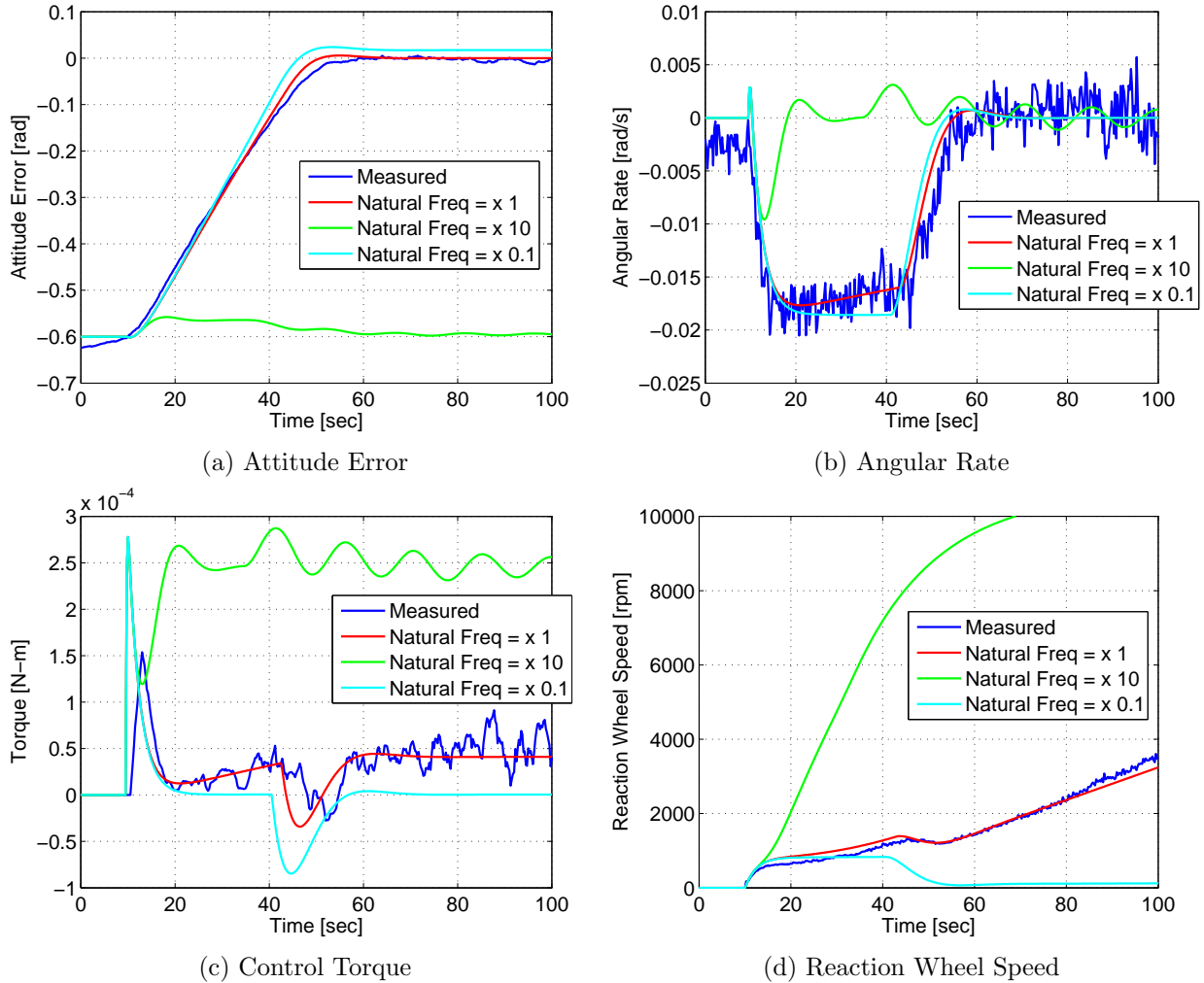


Figure 6-6: Model Response to Changing the Natural Frequency of the String

by the string. The reaction wheel speed, in Figure 6-6d, shows the wheels having to spin up much faster in order to supply that increased torque.

### 6.3 Concluding Thoughts

In conclusion, it appears that the characterization of the string from capturing its damping coefficient and natural frequency in a free-to-oscillate case with no actuators on was success-

ful. The model with no parameters tweaked yields a prediction that is quite close to the actual measured response. Of course, there is still some uncertainty as to why the model for the x-axis seemed to be off by a factor of about 2. However, the y- and z-axes' models performed adequately with no adjustment.

It seems that the model predicts the system's response to within 15%, and allows for detailed analysis of performance. The system met all requirements for each mode, except that of maintaining its attitude during the spin-up. However, as was discussed in Section 5.6.1, the attitude is recovered after spin-up, which is the true mission objective. Therefore, the test results shown in Chapter 5 demonstrate that MicroMAS's attitude determination and control algorithms work harmoniously with its actuators to perform in a predictable manner that meets requirements.

# Chapter 7

## Conclusion and Future Work

In this final chapter, we put into context what the results of this case study of testing the attitude determination and control subsystem of MicroMAS can contribute to the small satellite community. The goal of this work was to present a method for testing the ADCS of a small satellite in a resource-constrained environment. The idea was to start with the satellite's overall concept of operations (conops) and requirements, evaluate the test facilities available, and come up with tests that would be able to validate the ADCS algorithms with real hardware-in-the-loop. Then, these tests are modeled and evaluated based on their expected responses.

The results for the Detumble algorithm were that the measured response matched the predicted response to within 20%, and the error observed was within one standard deviation of the uncertainty of the measurements. The slew maneuver was validated by a model of the controller with the dynamics of the restoring torque of the string also capture. The results of these tests were a maximum 8% error in the x-axis, about 10% error in the y-axis, and about 13% error in the z-axis with respect to the model. In each case, the satellite achieved the desired slew rotation and was able to maintain its attitude to within one degree ( $3\sigma$ ) with no payload rotation. The Spin-up and Stabilization Mode tests showed that while the

satellite tended to deviate by about 5 degrees at the kick-off of the payload’s acceleration, it was able to maintain that attitude and then recover to within 2.2 degrees ( $3\sigma$ ). This exceeds the pointing threshold requirements for the mission (1 degree  $1\sigma$  deviation), and is largely due to the reaction wheels having little authority left to control after spin-up due to the lack of saturation ability in the lab. On orbit, the magnetorquers will continuously desaturate the reaction wheels, which allows them to recover some authority (approximately 1 mN-m of torque, down from their full 5 mN-m) after accounting for the momentum of the payload during spin-up. We believe this amount of torque to be adequate to account for disturbances.

Based on these results, we conclude that the controller for MicroMAS is able to fulfill its mission. The specific contributions that were made by the author were the application of the conops to coming up with a method by which to test the algorithms in-the-loop with real flight hardware, and creating a model by which to evaluate the tests. There were many surprises throughout the testing journey, and some of the lessons learned have been highlighted.

Future work would be to apply this method to another small satellite mission, and see how the test and evaluation process goes. The author would recommend spherical air bearing tests within a Helmholtz cage or other magnetic field emulator for future ADCS tests. The suspension test method was needed for the specific limitations of MicroMAS hardware (the spinning payload which caused center-of-mass offsets), but any small satellite with stationary hardware would be better off testing with more freedom of rotation available.

In addition, more sensor capability in the engineering unit in order to make it more flight-like would help validate the full system. MicroMAS was able to validate the controller and the Extended Kalman Filter, but had to rely on simulation results for initial attitude estimation. Having the ability to test those algorithms would build further confidence in the system.

At the end of the day, the question everyone wants the answer to in the satellite commu-

nity is whether the satellite is ready for launch. This research work attempts a closed-loop method to help an engineer to be able to answer that question.



# Bibliography

- [1] *Small is Beautiful: US Military Explores Use of Microsatellites*. Defense Industry Daily, 2011.
- [2] *CubeSat Design Specification*. San Luis Obispo, CA: California Polytechnic State University. URL: [http://www.srl.utu.fi/AuxDOC/tke/radmon/cubesat\\_standard.pdf](http://www.srl.utu.fi/AuxDOC/tke/radmon/cubesat_standard.pdf).
- [3] F. Landis Markley. *Fast Quaternion Attitude Estimation from Two Vector Measurements*. Greenbelt, MD: NASA Goddard Spaceflight Center.
- [4] Martin John Baker. *Maths - Quaternion Notations - As a quantity similar to axis-angle*. URL: <http://www.euclideanspace.com/mathematics/algebra/realNormedAlgebra/quaternions/geometric/axisAngle/>.
- [5] Daniel D. Kekez, Robert E. Zee, and Freddy M. Pranajaya. *Launches and On-Orbit Performance: An Update on Nanosatellite Missions at the UTIAS Space Flight Laboratory*. Space Flight Laboratory, University of Toronto, 2010.
- [6] James Armstrong et al. “23rd Annual AIAA/USU Conference for Small Satellites”. In: *Pointing Control for Low Altitude Triple CubeSat Space Darts*. American Institute of Aeronautics and Astronautics. 2009.
- [7] Stephen Arnold. “26th Annual AIAA/USU Conference on Small Satellites”. In: *QbX: The CubeSat Experiment*. U.S. Naval Research Laboratory. 2010.

- [8] Darren Rowen and Rick Dolphus. *3-Axis Attitude Determination and Control of the AeroCube-4 CubeSats*. The Aerospace Corporation, 2013.
- [9] Siegfried W. Janson and Richard P. Welle. “SSC13-II-1”. In: *The NASA Optical Communication and Sensor Demonstration Program*. The Aerospace Company. 2013.
- [10] Steve Wassom et al. “10th Annual CubeSat Developers’ Workshop”. In: *Integrated Test Facility for Nanosat Assessment and Verification*. American Institute of Aeronautics and Astronautics. 2013.
- [11] David M. Meissner. “A Three Degrees of Freedom Test Bed for Nanosatellite and CubeSat Attitude Dynamics, Determination, and Control”. MA thesis. Naval Postgraduate School, 2009.
- [12] Corey Crowell. “Development and Analysis of a Small Satellite Attitude Determination and Control System Testbed”. MA thesis. Massachusetts Institute of Technology, 2010.
- [13] Tyler Ustrzycki, Regina Lee, and Hugh Chesser. “AIAA Modeling and Simulation Technologies Conference”. In: *Spherical Air Bearing Attitude Control Simulator for Nanosatellites*. American Institute of Aeronautics and Astronautics. 2011.
- [14] Oscar R. Polo et al. “End-to-end validation process for the INTA-Nanosat-1B Attitude Control System”. In: *Acta Astronautica* 93 (2014), pp. 94–105.
- [15] Christopher Masaru Pong. “High-Precision Pointing and Attitude Estimation and Control Algorithms for Hardware-Constrained Spacecraft”. PhD thesis. Massachusetts Institute of Technology, 2014.
- [16] William Blackwell and Kerri Cahoy. “27th Annual AIAA/USU Conference on Small Satellites”. In: *MicroMAS: A First Step Towards a Nanosatellite Constellation for Global Storm Observation*. American Institute of Aeronautics and Astronautics. 2013.
- [17] Eric Peters. *MicroMAS CAD Models*. MIT Graduate Student.

- [18] K. Cahoy et al. “CubeSat Developers’ Workshop”. In: *Microsized Microwave Atmospheric Satellite (MicroMAS)*. American Institute of Aeronautics and Astronautics. 2013.
- [19] R. Kingsbury et al. “Nuclear and Space Radiation Effects Conference (NSREC)”. In: *TID Tolerance of Popular CubeSat Components*. Institute of Electrical and Electronics Engineers (IEEE). 2013.
- [20] Evan D. Wise. “Design, Analysis, and Testing of a Precision Guidance, Navigation, and Control System for a Dual-Spinning CubeSat”. MA thesis. Massachusetts Institute of Technology, 2013.
- [21] Kerri Cahoy et al. *Microsized Microwave Atmospheric Satellite (MicroMAS): CDR-B*. powerpoint presentation. MIT Space Systems Laboratory, 2012.
- [22] *ADIS 16334: Low Profile Six Degree of Freedom Inertial Sensor*. Norwood, MA: Analog Devices. URL: [http://www.analog.com/static/imported-files/data\\_sheets/ADIS16334.pdf](http://www.analog.com/static/imported-files/data_sheets/ADIS16334.pdf).
- [23] *MicroMag3: 3-Axis Magnetic Sensor Module*. Santa Rosa, CA: PNI Sensor Corporation. URL: <https://www.sparkfun.com/datasheets/Sensors/MicroMag3%20Data%20Sheet.pdf>.
- [24] *Solderable Planar Photodiode*. Montreal, Quebec: Silonex, Incorporated. URL: <http://www.datasheet-pdf.com/datasheet/Silonex/652556/SLSD-71N7.pdf.html>.
- [25] *Thermopile Detector*. Weisbaden, Germany: Excelitas Technologies. URL: [http://www.elv-downloads.de/Assets/Produkte/4/469/46963/Downloads/46963\\_Sensor\\_TPS\\_DS.pdf](http://www.elv-downloads.de/Assets/Produkte/4/469/46963/Downloads/46963_Sensor_TPS_DS.pdf).
- [26] Tam Nguyen. “28th Annual AIAA/USU Conference on Small Satellites”. In: *Attitude Determination using Infrared Earth Horizon Sensors*. American Institute of Aeronautics and Astronautics. 2014.

- [27] Sergei Tanygin and Malcolm D. Shuster. *The Many TRIAD Algorithms*. American Astronomical Society.
- [28] T. S. Kelso. *NORAD Two-Line Element Sets*. URL: <http://www.celestrak.com/NORAD/elements/>.
- [29] David A. Vallado. *Fundamentals of Astrodynamics and Applications*. New York: Springer, 2001.
- [30] E. J. Lefferts, F. L. Markley, and M. D. Shuster. “Kalman Filtering for Spacecraft Attitude Estimation”. In: *AIAA Journal of Guidance* 5.5 (1982), pp. 417–429.
- [31] John L. Crassidis and John L. Junkins. *Optimal Estimation of Dynamic Systems, Second Edition*. London: Chapman and Hall/CRC, 2011.
- [32] Jonathan P. How. “16.322: Stochastic Estimation and Control (Spr10)”. Powerpoint presentation of notes for graduate level class at MIT.
- [33] *MAI-400 Specifications*. Crofton, MD: Maryland Aerospace Incorporated. URL: [http://www.miniadacs.com/miniadacs\\_012.htm](http://www.miniadacs.com/miniadacs_012.htm).
- [34] A. Craig Stickler and K. T. Alfriend. “Elementary Magnetic Attitude Control System”. In: *Journal of Spacecraft* 13.5 (1976).
- [35] B. Wie, H. Weiss, and A. Aropostathis. “Quaternion Feedback Regulator for Spacecraft Eigenaxis Rotations”. In: *AIAA Journal of Guidance* 12.3 (1989), pp. 375–380.
- [36] Norman S. Nise. *Controls Systems Engineering, 6th Edition*. Hoboken, NJ: John Wiley & Sons, 2010.
- [37] Meghan K. Prinkey et al. “AIAA Guidance, Navigation, and Control Conference”. In: *CubeSat Attitude Control Testbed Design: Merritt 4-Coil per Axis Helmholtz Cage and Spherical Air Bearing*. American Institute of Aeronautics and Astronautics. 2013.

- [38] Raichelie J. Aniceto. “AIAA Student Paper Conference”. In: *MicroMAS and MiRaTA Radiation Environment*. American Institute of Aeronautics and Astronautics. 2014.
- [39] *Spherical Air Bearings*. Specialty Components. URL: [http://www.specialtycomponents.com/spherical\\_air\\_bearings.html](http://www.specialtycomponents.com/spherical_air_bearings.html).
- [40] Jeff Weaver. “CubeSat Developers’ Workshop”. In: *ExoCube and a Gravity Gradient ADCS*. American Institute of Aeronautics and Astronautics. 2013.
- [41] Dominic Del Rosso. *Reduced Gravity Program*. National Aeronautics and Space Administration. URL: <https://zerog.jsc.nasa.gov/home.html>.
- [42] I. S. Grant and W. R. Phillips. *Electromagnetics, 2nd Edition*. Hoboken, NJ: John Wiley & Sons, 2008.
- [43] Joseph L. Kirschvink. “Uniform Magnetic Fields and Double-Wrapped Coil Systems: Improved Techniques for the Design of Bioelectromagnetic Experiments”. In: *Bioelectromagnetics* 13 (1992), pp. 401–411.
- [44] *3-Axis Fluxgate Magnetometers*. Mountain View, CA: Applied Physics Systems. URL: [http://www.2genterprises.com/Prod\\_Model1520.pdf](http://www.2genterprises.com/Prod_Model1520.pdf).
- [45] *Boxplots*. Mathworks. URL: <http://www.mathworks.com/help/stats/boxplot.html>.
- [46] *Program Level Poly-picosatellite Orbital Deployer (PPOD) and CubeSat Requirements Document*. John F. Kennedy Space Center, Florida: National Aeronautics and Space Administration, Launch Services Program. URL: [http://www.nasa.gov/pdf/627972main\\_LSP-REQ-317\\_01A.pdf](http://www.nasa.gov/pdf/627972main_LSP-REQ-317_01A.pdf).
- [47] Katsuhiko Ogata. *Modern Control Engineering*. Englewood Cliffs, NJ: Prentice-Hall, Inc., 1970.

- [48] Christopher Pong, Sara Seager, and David Miller. “Guidance, Navigation, and Control (GN&C) Conference”. In: *Three-Degree-of-Freedom Testing of Attitude Determination and Control Algorithms on ExoPlanetSat*. American Astronautical Society (AAS). 2014.
- [49] S. Diop, V. Fromion, and J. W. Grizzle. *A resettable Kalman filter based on numerical differentiation*. University of Michigan, Department of Electrical Engineering and Computer Science, 2000.